

Eldbjørg Stenrud Nilsen

Numerical Modelling of the Stress Field and Failure Behaviour of Grouted Rocks

Master's thesis in Geotechnology

Supervisor: Alexandre Lavrov

June 2021

Eldbjørg Stenrud Nilsen

Numerical Modelling of the Stress Field and Failure Behaviour of Grouted Rocks

Master's thesis in Geotechnology
Supervisor: Alexandre Lavrov
June 2021

Norwegian University of Science and Technology
Faculty of Engineering
Department of Geoscience and Petroleum



Abstract

This study investigated the strengthening effects from grouting of rock specimens containing flaws of varying length and dip angle *via* numerical modelling. For this purpose, two- and three-dimensional numerical simulations of rock specimens containing grouted and non-grouted flaws were carried out in the finite element method (FEM) programs Abaqus/Standard and RS2. The basis for the numerical model design was the methodology behind experimental uniaxial compression tests of grouted rocks performed by Le et al. (2018). The findings suggest that grouting improves the strength of rocks containing open flaws. Moreover, the grout reinforcement effect is most pronounced for specimens containing the longest flaws and for specimens containing flaws that are rotated 75-90° from the loading axis. Both literature and the computed stress plots suggest that stress reduction around the flaw tip is one mechanism behind the grout reinforcement effect. Another aim of the current study was to verify the numerical models against the available lab results from Le et al. (2018). The numerical and experimental results show good agreement based on the following observations: (1) both the numerical and experimental tests produced tensile cracks initiating from the flaw tip and growing parallel to the applied load and (2) the numerical yielded elements contour plots and experimental crack patterns qualitatively show similar failure modes. However, two crack types that were observed in lab tests of grouted specimens — a tensile crack originating from the middle-area of the grouted flaw and a shear crack initiating from the rock-grout interface — do not occur in the 2D numerical models. This thesis therefore suggests that further three-dimensional finite element analyses — where the flaw boundary is modelled with interface elements — are carried out.

Sammendrag

Denne masteroppgaven undersøkte den forsterkende effekten fra injeksjon av bergprøvestykker som inneholder åpne sprekker av varierende lengde og fallvinkel, gjennom numerisk modellering. Til dette formålet ble to- og tredimensjonale numeriske simuleringer av prøvestykker som inneholder injiserte og ikke-injiserte sprekker utført i elementmetodeprogrammene Abaqus/Standard og RS2. Den numeriske modelleringen tok sikte på å etterprøve enaksiale trykkforsøk av injiserte og ikke-injiserte prøvestykker, som ble utført i laboratorium av Le et al. (2018). De numeriske modellene ble derfor oppbygd etter metodikkbeskrivelsen av de nevnte laboratorieforsøkene. Funnene antyder at injeksjon forbedrer styrken av berg som inneholder åpne sprekker. Videre er den forsterkende effekten mest tydelig for prøvestykkene som inneholder de lengste sprekke, og for de prøvestykkene som inneholder sprekker rotert $75 - 90^\circ$ fra kompresjonsaksen. Både litteratur og beregnede spenningsplott foreslår at spenningsreduksjon rundt sprekketuppen er en av mekanismene bak forsterkningseffekten. Et annet mål med oppgaven var å verifisere de numeriske modellene mot de tilgjengelige eksperimentelle resultatene fra Le et al. (2018). De numeriske og eksperimentelle resultatene stemmer godt basert på de følgende observasjonene: (1) Både de numeriske og eksperimentelle testene produserte strekkbrudd som initieres fra sprekketuppen og vokser parallelt med den påsatte lasten, og (2) de numeriske bruddelement-konturplottene og de eksperimentelle sprekke mønstrene viser kvalitativt lignende bruddmoduser. To sprekketyper som ble observert i laboratorieforsøkene, forekommer likevel ikke i de todimensjonale numeriske analysene. Dette gjelder en sprekke type som åpnes i strekkmodus og utvikles fra midtområdet på injiserte preeksisterende sprekker, samt en sprekke type som opptrer som skjærbrudd langs berg-mørtel-grenseflaten til injiserte preeksisterende sprekker. Derfor foreslås det at videre tre-dimensjonale numeriske analyser, der sprekkeflaten modelleres med overflateelementer, utføres i fremtidig forskning.

Preface

This master's thesis finishes a 5-year study program in Geotechnology ("tekniske geofag") at the Norwegian University of Science and Technology (NTNU). The thesis was written during the spring of 2021 under the Department of Geoscience and Petroleum.

In the beginning of the autumn semester of 2020, my supervisor, Prof. Alexandre Lavrov, suggested an interesting specialization project and a good special course syllabus. This master's thesis primarily builds on the numerical simulations that I did in my special course about fracture mechanics. However, the literature searches and experience in numerical modelling and academic writing from my specialization project about tunnels constructed in grouted rock masses were also very useful.

As with many things in life, this thesis work was confusing and slightly overwhelming at first, but turned out as quite exciting and rewarding towards the end. I definitely learned a lot during this semester.

Trondheim, June 2021

Eldbjørg Stenrud Nilsen

Acknowledgement

Professor Alexandre Lavrov,
Your vast expertise was solid inspiration
and valuable when writing this dissertation.
You reviewed the manuscripts that I sent
and I appreciate the time you spent.
For meetings and guidance too
Thank you!

Brian, you let me borrow your office space.
For peace and inspiration, there was no better place.
I am really grateful.
I also want to thank Cata, my flatmate and friend
for advice and hilarious breaks, from beginning to end.

And my best friend John!
You supported me from early on,
with spell checks and priceless jokes,
encouragement, snacks, ice cold cokes.
Cheers mate

E.S. Nilsen

Contents

Figures	xiii
Tables	xv
Nomenclature	xvi
1 Introduction	1
1.1 Fracture mechanics of intact rock	1
1.2 Fracture mechanics of grouted rock	2
1.3 Research task	3
1.4 Report structure	4
2 Crack Types in Grouted and Non-Grouted Specimens	5
2.1 Specimen preparation, material properties and testing procedure from Le et al. (2018) . .	5
2.2 Strengthening effect and crack types from Le et al. (2018)	6
2.2.1 Increased mechanical properties after grouting	6
2.2.2 Crack types observed in grouted and ungrouted flaws	7
2.2.3 Flaw geometry and filling and their effect on crack types	8
3 The Finite Element Method	12
3.1 Basic FEM principles	12
3.2 Solving nonlinear numerical problems	13
3.2.1 The Newton-Raphson method	14
3.2.2 The initial stiffness method and accelerated initial stiffness method	15
3.3 Shape functions and mesh refinement tests	16
3.4 Commercial FEM codes	16
3.4.1 Abaqus	16
3.4.2 RS2	17
4 Methodology	18
4.1 Experimental design (2D)	18
4.1.1 Experimental design — geometry	18
4.1.2 Experimental design — material properties	19
4.1.3 Experimental design — load and boundary conditions	20
4.1.4 Experimental design — mesh	20
4.1.5 Experimental design — other settings	21

4.2	Code validation (2D)	21
4.2.1	Code validation — geometry	21
4.2.2	Code validation — material properties	22
4.2.3	Code validation — load and boundary conditions	22
4.2.4	Code validation — mesh	23
4.2.5	Code validation — other settings	23
4.3	2D/3D validation	24
4.3.1	2D/3D validation — geometry	24
4.3.2	2D/3D validation — material properties	24
4.3.3	2D/3D validation — load and boundary conditions	25
4.3.4	2D/3D validation — mesh	25
5	Results	28
5.1	Experimental design	28
5.1.1	Experimental design — linear-elastic results	28
5.1.2	Experimental design — elastoplastic results	33
5.2	Code validation	38
5.2.1	Code validation — linear-elastic results	38
5.2.2	Code validation — elastoplastic results	38
5.3	2D/3D validation	41
5.3.1	2D/3D validation — elastoplastic stress results	41
5.3.2	2D/3D validation — yielded elements	42
5.3.3	2D/3D validation — linear-elastic stress results	43
5.3.4	2D/3D validation — nonzero σ_z buildups in the outer x-y-plane of 3D models . . .	44
6	Comparison of Numerical Results and Experimental Results	47
6.1	UngROUTED rocks	47
6.1.1	Far-field and spalling crack types not observed in numerical models	47
6.1.2	Flaw tip tensile cracks	48
6.1.3	Shear failure indicated in numerical models	48
6.1.4	Midflaw tensile cracks around ungrouted flaws	49
6.1.5	UngROUTED specimen strength based on flaw length and dip angle	50
6.2	Grouted rocks	51
6.2.1	Far-field and flaw-tip tensile cracks in grouted rocks	51
6.2.2	Midflaw tensile cracks in grouted rocks	52
6.2.3	Shear cracks in grouted rocks	53

6.2.4	Grouted specimen strength based on flaw length and dip angle	53
6.3	Grout reinforcement effect	54
6.3.1	Yielding	54
6.3.2	The stress field before and after grouting	54
6.4	Overall agreement between numerical models and literature	55
7	Discussion of the Numerical Models	57
7.1	Agreement between the models	57
7.1.1	Agreement between RS2 and ABQ results	57
7.1.2	2D and 3D models	58
7.1.3	Unexpected nonzero σ_z buildups along material boundary in 3D models	59
7.2	Challenges with the design	60
7.2.1	Challenges with the geometrical model	60
7.2.2	Challenges with the material properties	61
7.2.3	Experience with Abaqus/Standard and RS2	61
7.2.4	Program recommendations for further work	63
8	Conclusions and Suggestions for Future Research	64
8.1	Conclusions	64
8.2	Suggestions for further research	65
	Bibliography	67
	Appendix	69
	Figures	
1	Schematic of a wing crack	1
2	En passant microcrack linking, from Kranz (1979)	2
3	Grouted specimen and schematic tangential stress-displacement curves, from Liu et al. (2017)	3
4	Specimen geometry and example of a specimen, from Le et al. (2018)	6
5	Strengthening factor from grouting of flaws of varying geometry, from (Le et al., 2018).	7
6	Crack types observed in specimens containing ungrouted flaws, from Le et al. (2018) . . .	8
7	Crack types observed in specimens containing grouted flaws, from Le et al. (2018)	9
8	Specimens after failure, after Le et al. (2018)	10
9	Example of cracks in grouted and ungrouted specimens, from Le et al. (2018)	11
10	Internal and external forces on a meshed structure under uniaxial loading	12

11	Nonlinear load/displacement curve, from Dassault Systèmes (2014)	14
12	The first iteration with the Newton-Raphson method, from Dassault Systèmes (2014) . .	15
13	Flaw details for 2D specimens	19
14	Mesh and loading example	20
15	Comparison of the mesh on models containing ungrouted and grouted flaws	21
16	Comparison of the meshes used in ABQ and RS2	23
17	Geometry 3D models	24
18	Boundary conditions 3D models	25
19	Mesh 3D models	26
20	Experimental design: maximal compressive stress values from linear-elastic models.	29
21	Experimental design: maximal tensile stress values from linear-elastic models.	29
22	Experimental design: σ_1 contour plot example from ungrouted and grouted linear-elastic models with long flaws	30
23	Experimental design: σ_1 contour plot example from ungrouted and grouted linear-elastic models with long flaws (flaw details)	30
24	Experimental design: σ_3 contour plot example from ungrouted and grouted linear-elastic models with long flaws	31
25	Experimental design: σ_3 contour plot example from ungrouted and grouted linear-elastic models with long flaws (flaw details)	31
26	Experimental design: σ_1 contour plot example for ungrouted and grouted linear-elastic models with short flaws	32
27	Experimental design: σ_3 contour plot example for ungrouted and grouted linear-elastic models with short flaws	32
28	Legend for yielded elements contour plots.	35
29	Experimental design: yielded elements around grouted and ungrouted flaws ($2a = 20\text{mm}$, $\alpha = 45^\circ$)	36
30	Experimental design: yielded elements around grouted and ungrouted flaws ($2a = 20\text{mm}$, $\alpha = 45^\circ$), flaw details	36
31	Experimental design: marked crack types examples around ungrouted flaws	37
32	Experimental design: σ_1 contour plot example from ungrouted and grouted elastoplastic models	37
33	Code validation: σ_1 contour plots from elastoplastic models from Abaqus/Standard and RS2	39
34	Code validation: yielded elements from Abaqus/Standard and RS2	40
35	2D/3D validation: σ_3 legend for Figure 36	41
36	2D/3D validation: σ_3 contour plots from elastoplastic 2D and 3D models	42
37	2D/3D validation: AC yield contour plots for 2D and 3D models	42
38	2D/3D validation: σ_3 legend for Figure 39	43
39	2D/3D validation: σ_3 contour plots from linear-elastic 2D and 3D models	44

40	2D/3D validation: locations of points A, B and C	44
41	2D/3D validation: sigma ZZ stress effects 3D models	46
42	Comparison of lab results and numerical results for an ungrouted specimen	49
43	Crack types from numerical models and lab specimens containing a 10 mm long grouted flaw with $\alpha = 0^\circ$	52
44	Schematic of possible grouting results in the time after injection (exaggerated).	53
45	Yielded elements for grouted and ungrouted flaws with varying flaws lengths ($\alpha = 60^\circ$) . .	56
46	Loading diagram of 3D uniaxial compression tests	59

Tables

1	Flaw geometries of specimens subjected to uniaxial compression tests by Le et al. (2018) .	5
2	Material parameters for intact model material (rock-like material/cement mortar) and epoxy from Le et al. (2018).	5
3	Crack types observed in uniaxial compression tests by Le et al. (2018)	7
4	Comparison of RS2 and Abaqus/Standard features.	17
5	Overview of performed numerical simulation sets	18
6	Experimental design: material properties	19
7	Code validation: flaw geometries and total number of elements in meshes	22
8	Code validation: material properties	22
9	2D/3D validation: material properties	25
10	2D/3D validation: overview of simulations	27
11	Experimental design: summary of elastoplastic results	34
12	Code validation: linear-elastic and elastoplastic results	38
13	2D/3D validation: Maximum and minimum stress concentrations	41
14	2D/3D validation: linear-elastic stress results for 2D and 3D models	43
15	2D/3D validation: σ_z values elastoplastic 3D models	45
16	2D/3D validation: stress values linear elastic results	45
17	Comparison of crack types observed in numerical simulations and lab experiments for rocks containing ungrouted flaws	47
18	Comparison of crack types observed in numerical simulations and lab experiments for rocks containing grouted flaws	51

Nomenclature

Abbreviations

2D	Two-dimensional
3D	Three-dimensional
ABQ	Abaqus/Standard
DOF	Degrees of freedom
FEA	Finite element analysis
FEM	Finite element method
FT	Flaw tip
G	Grouted
MC	Mohr-Coulomb
MF	Midflaw
NG	Not grouted (ungrouted)
UCS	Uniaxial compressive strength
w/c	Water-cement ratio

Symbols (finite element analysis)

α	Acceleration factor used in the accelerated initial stiffness method
ΔU_i	Displacement correction at the i -th iteration
ϵ	Strain
σ	Stress
A	Cross-sectional area of elastic bar
b	Bulk force per unit length
c_a	Displacement correction
f	Applied force
k	Spring stiffness
K_0	Initial stiffness
L	Length of elastic bar
n	Order of polynomial shape function
P	Polynomial
R_a	Incremental force residual
tol	Tolerance value used in numerical iteration solvers
u	Nodal displacement
U_i	Total displacement
u_s	Displacement of elastic spring
[F]	Vector of external forces or total force

[I] Vector of internal forces

[K_0] Initial stiffness matrix

[K] Stiffness matrix

Symbols (rock mechanics)

$2a$ Flaw length

α Flaw dip angle

ν Poisson's ratio

ϕ Internal angle of friction

ϕ_j Internal angle of friction of flaw surface

ψ Dilation angle

σ_1 Maximal principal stress

σ_2 Intermediate principal stress

σ_3 Minimal principal stress

σ_c Compressive stress

σ_t Tensile strength or tensile stress

τ Shear strength

c Cohesion

c_j Cohesion of flaw surface

D_s Strengthening factor — a measure of the grout reinforcement effect

E Deformation modulus or Young's modulus

t Flaw thickness

UCS_g Uniaxial compressive strength of grouted specimen

UCS_u Uniaxial compressive strength of ungrouted specimen

1 Introduction

Rock mass grouting can be defined as the injection of a fluid, such as cement or epoxy, into a rock mass under pressure. In tunneling, grouting is performed for the purposes of ground water control or improvement of rock mass stability. Grouting is fundamental in areas with high requirements for water control, for example in urban areas. In rock masses of low quality, grouting can be performed for ground reinforcement. For rock masses with a high amount of discontinuities, ground reinforcement is especially relevant. This thesis examines fracture behaviour of grouted, fractured rock specimens via numerical modelling.

Fractures and fracture networks are features of great interest in rock mass grouting. Fractures provide flow paths for injection fluids (grouts) in rock masses. Cement suspensions are often used as injection fluids, and are expected to behave as non-Newtonian fluids (Mo and Skjetne, 2016, Liu et al., 2017, Bohlooli et al., 2019). The properties of the fracture walls, such as aperture width and roughness, affect the flow and penetration length of non-Newtonian injection fluids (Brown, 1987, Barton et al., 1985, Barton and de Quadros, 1997, Saeidi et al., 2013). The grouting outcome therefore depends on the presence of fractures and their properties, in addition to the grout properties and grouting pressure. Several studies have indicated that fractured rock masses show pronounced strengthening effects after grouting (Liu et al., 2017, Le et al., 2018, Wang et al., 2019). Before discussing grouted rock mechanics, it is however necessary to provide an introduction to fracture mechanics of intact rocks. This is given in the following section.

1.1 Fracture mechanics of intact rock

The theoretical strength of a solid depends on the atomic bond strength, and can be quantified as the applied stress necessary to break the atomic bonds in the material. Moreover, preexisting grain boundaries make up weakness planes in the material. The practical material strength is therefore 10 to 100 times lower than the theoretical strength for bulk materials (Sun and Jin, 2012*b*). In rocks, grain boundaries, pores and microcracks exist; depending on rock type and stress history.

Fracture failure implies that the failure of a material is caused by fracture propagation (Sun and Jin, 2012*a*). At the tips of pre-existing material flaws — such as microcracks, micropores and grain boundaries — stress concentrations of magnitudes higher than the material strength occur (Sun and Jin, 2012*b*). Fracture growth initiates at tips of the material flaws in shear, tensile or tearing modes, and they propagate in the direction of the local maximal principal stress (σ_1) and perpendicular to the direction of the local minimal principal stress (σ_3) (Kranz, 1979, Hoek and Martin, 2014). Figure 1 is a schematic of crack development at the tips of a preexisting flaw with length $2a$ and dip angle α in local stress condition. Specifically, the figure illustrates a wing crack, which is a crack type that initiates at the tips of inclined penny-shaped flaws and grows parallel to σ_1 (Ashby and Sammis, 1990).

It is well established that macro-scale fractures in intact rocks are formed by coalescence of microscopic structures such as microcracks, micropores and grain boundaries (Kranz, 1979, Eberhardt et al., 1999, Hoek and Martin, 2014). For the purpose of quantifying stress-induced damage in rocks, Eberhardt et al. (1999) conducted cyclic uniaxial compression tests on rock specimens. The test procedure included measurements of acoustic emissions, which is the rapid energy release that occurs when molecular bonds are broken. Acoustic emission events were used to quantify mechanical events such as initiation, growth or coalescence of microfractures. The tests showed that the microcrack population gradually built

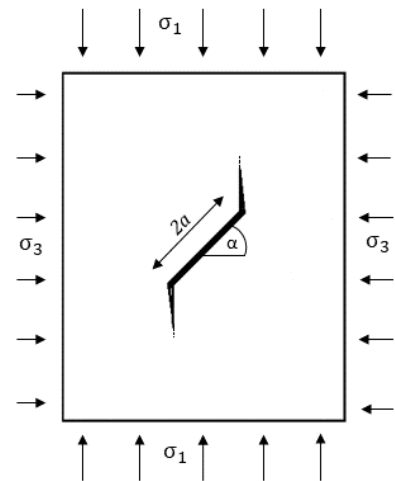


Figure 1: Schematic of a wing crack, that initiates on the tip of a preexisting flaw with length $2a$ and dip angle α . The crack initiates due to high stress concentrations at the flaw tip and grows parallel to σ_1 .

up with repeated loading. During the loading cycles, the Young's modulus and Poisson's ratio gradually decreased and increased respectively. When the microcrack population reached the crack damage threshold at approximately 0.75 of the uniaxial compressive strength, unstable crack growth would result in an inevitable critical failure plane in the specimen (Eberhardt et al., 1999).

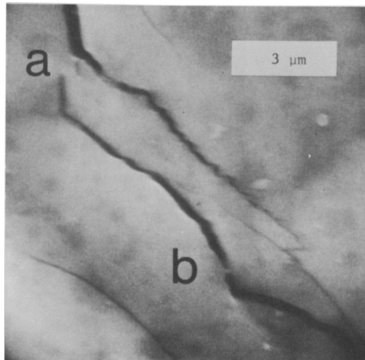


Figure 2: This photomicrograph (see scale bar) shows an *en passant* interaction between microcracks (Kranz, 1979). The microcracks link at location *a*.

Via scanning electron microscope observations, Kranz (1979) studied interactions between microcracks and between microcrack and micropores in granites. The interaction types between existing microcracks, *en echelon* and *en passant*, emerged from the study. *En echelon* interactions were characterized by either extension cracks growing parallel to the direction of the maximum principal stress or shear cracks. High shear stress concentrations between the crack tips is typical for this interaction type. The *en passant* interactions can be described as two cracks approaching each other in parallel planes until either one crack joins the side of the other crack, or the growth paths deviate from each other and follow the direction of the applied stress field (Kranz, 1979). See Figure 2. Kranz (1979) further found that material between cracks can be stress relieved. Moreover, combinations of *en echelon* and *en passant* are usual, and the micro-scale interactions are complicated. Kranz (1979) concluded that the magnitude and direction of the stress experienced by the microcracks deviates from the applied stress field.

In failure analyses, the intermediate principal stress, σ_2 is often assumed to have little influence on the failure process (Hoek and Martin, 2014). Compared to the dimensions of rock specimens, mineral grain sizes are relatively small. Therefore, rock specimen are often considered a homogeneous and isotropic material, and discussed in two dimensions (Hoek and Martin, 2014). In two-dimensional failure analysis, failure criteria are used. Failure criteria are functions for prediction of shear and/or tensile failure of rocks based on the stress conditions and known material parameters. Within rock engineering, the Mohr-Coulomb criterion (MC-criterion) is a commonly used failure criterion. The criterion expresses the shear strength of a material, τ , as a linear function of the applied normal stress, σ_n , with the cohesion, c and angle of internal friction, ϕ of the material. The MC-criterion is expressed as follows (Labuz and Zang, 2012):

$$\tau = \sigma_n \tan \phi + c. \quad (1)$$

In two-dimensional failure analysis, Eq. 1 is used with the Mohr circle, a circle with a diameter $\sigma_1 - \sigma_3$. When the Mohr circle is tangent to Eq. 1, the stress state and material strength is associated with failure (Labuz and Zang, 2012).

As indicated in this section, fracture mechanics is characterized with complicated interactions on microscopic levels. Still, a considerable amount of literature is published in this area, and several principles are well established. However, few studies have investigated on the effect of grouting in failure mechanics. The following part of this thesis moves on to presenting recent studies on fracture mechanics of grouted rocks.

1.2 Fracture mechanics of grouted rock

Recent studies have found that grouting increases the shear strength parameters of fractured rock specimens (Liu et al., 2017, Le et al., 2018, Wang et al., 2019). Grouting has additionally been found to improve the rock mass quality in terms of increased Q-value (Zolfaghari et al., 2015). Liu et al. (2017) performed shear loading tests on grouted and non-grouted fractured sandstone specimens (with persistent fractures). An example specimen in the grouting mold is shown in Figure 3 a). The stress-displacement data showed a peak shear strength increase by 106-170% and a residual shear strength increase by 54-72% after grouting with cement (Liu et al., 2017). In shear loading tests of fractured rock-like specimens, Wang et al. (2019) found that that the shear strength improvement was higher when using cement grouts of lower w/c number (w/c = 0.6). Furthermore, failure characteristics analyses suggested that the failure mode is affected by grouting. The non-grouted specimens demonstrated a typical plastic failure type, while the failure mode of the grouted specimens were typical brittle (Liu et al., 2017, Wang et al., 2019). Liu et al. (2017) proposed a schematic stress-displacement curve, which is shown in Figure 3 b).

A study by Le et al. (2018) examined the failure modes of grouted and non-grouted fractured specimens in further detail. The study included uniaxial compression tests of specimens containing open or grout-infilled non-persistent flaws of varying lengths and dip angles. Le et al. (2018) concluded that the grout reinforcement effect is ascribed to two mechanics: The shear strength parameters (ϕ and c) in the model-fracture interface are increased and stress concentrations at the flaw tips are reduced. An interesting finding that emerged from this study was that the cracks did not always initiate at the tip of the flaw for specimens with a grouted flaw (Le et al., 2018). In some cases, the primary cracks initiated close to the middle of the flaw. Consequently, two new fracture types that occur in specimens with grouted flaws were suggested. This thesis is based on the study by Le et al. (2018). A detailed review of the proposed fracture types (and other findings) is therefore presented in Chapter 2.

The Intact (non-fractured) rock specimens demonstrated higher strength properties than the grouted (fractured) specimens in the research by Liu et al. (2017), Wang et al. (2019) and Le et al. (2018). Intact rock or high quality rock masses are in other words unlikely to benefit from grouting — at least from a strength reinforcement perspective. Also, these types of rock masses provide limited flow paths or area to transport or hold the grout. Consequently, intact rocks and high quality rock masses were not the primary focus of this study.

As presented in this section, most research on the strengthening aspects of grouting has been carried out in laboratory studies. To the author’s knowledge, no large-scale in-situ tests of grout reinforcement of rock masses are available. Numerical modelling can be a suitable tool to examine a large-scale problem such as fracture mechanics of a grouted rock mass. Before modelling the mechanical behaviour of grouted rock masses, it is however necessary to build and validate numerical models against the available lab results of grouted rock specimens. This outlines the motivation for this thesis. The following section presents the research aims and report structure.

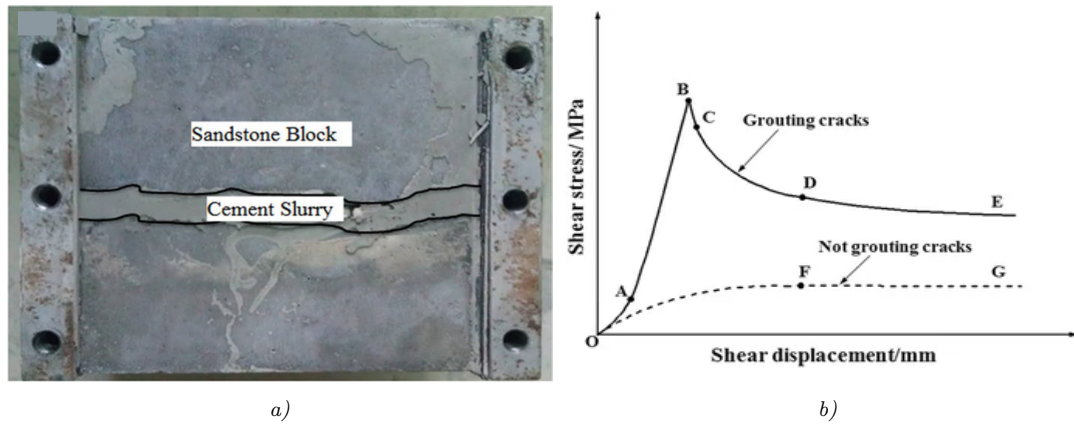


Figure 3: a) Specimen after grouting (in grouting mold) from Liu et al. (2017). b) Schematic stress-displacement curves for grouted and non-grouted fractured specimens (Liu et al., 2017).

1.3 Research task

The goal of this study was to examine the failure modes in specimens containing grouted and non-grouted, open flaws (fractures) under uniaxial compression. The research was based on the work by Le et al. (2018), and aimed to verify these experimental results using numerical modelling.

The finite element method (FEM) codes Abaqus/Standard and RS2 were used for the numerical simulations of uniaxial compression tests of the grouted and non-grouted rock specimens. The FEM programs returned contour plots of yielded elements (according to the MC-criterion) and stress conditions, which were used to address the research goal. The task was assessed through several objectives, which specifically set out to achieve the following points:

- examine the stress distribution in the specimen, both close to the flaw and far field;
- explore how flaw dip angles and flaw lengths affect the failure modes and stress distribution in the

model; and

- compare the observed yielding patterns from the numerical modelling with the experimental results described by Le et al. (2018).

1.4 Report structure

The next parts of this thesis are organised as follows:

Chapter 2 provides detailed information about crack types that have been observed in uniaxial compression tests by Le et al. (2018), and other results that emerged from these tests.

Chapter 3 lays out the basic principles behind the finite element method and why the method was chosen.

Chapter 4 moves on to documenting the methodology behind the performed numerical simulations of uniaxial compression tests.

Chapter 5 presents the results of the numerical simulations.

Chapter 6 compares the experimental results from Chapter 2 with the numerical results from Chapter 5 and discusses the differences.

Chapter 7 describes the agreement between the simulations from this research. This includes comparing results from different programs and models using different assumptions. Errors, challenges and assumptions are discussed.

Chapter 8 rounds off this thesis with conclusions and suggestions for further research.

2 Crack Types in Grouted and Non-Grouted Specimens

In 2018, Le et al. published a study on the mechanical properties and cracking behaviour under uniaxial compression of rock-like specimens containing a single, grouted flaw (as mentioned in the introduction). Specimens containing ungrouted flaws were also tested. This chapter presents the methodology and results from the work by Le et al. (2018) in more depth.

2.1 Specimen preparation, material properties and testing procedure from Le et al. (2018)

The specimens used for the project were made from cement mortar (fine sand, Portland 42.5 cement and water mixed with weight ratio 2:1:0.5). Cement mortar was used to replicate rock specimens, and does not come with *e.g.* weathering or developed fracture planes (which occur in natural rock masses) that could influence the test results. The cement mortar was cast in square prismatic steel molds containing a single 1 mm thick steel sheet of varying lengths (10-30 mm) and orientations (1-90° from the horizontal line). The specimens had the following dimensions: Height of 100 mm, depth of 50 mm and width of 50 mm. After the first 24 hours of curing, the steel sheets were pulled out to make the open flaws. The total curing time for the specimens was 28 days in constant humidity and temperature. For half of the specimens, the open flaw was injected with epoxy resin (Bisphenol A) and left to cure for an additional 3 days. Figure 4 shows a specimen containing an ungrouted flaw and a sketch of the geometry. In addition to an intact specimens (without flaw), Le et al. (2018) tested 42 combinations of specimens containing a grout-infilled or unfilled flaw of varying dip angle (α) and length ($2a$). The combinations are listed in Table 1.

Table 1: Tested flaw geometries from Le et al. (2018).

Specimen type	$2a$ (mm)	t (mm)	α (°)
Intact specimen	0	0	N/A
Specimens with grouted flaw	10	1	0, 15, 30, 45, 60, 75, 90
	20	1	0, 15, 30, 45, 60, 75, 90
	30	1	0, 15, 30, 45, 60, 75, 90
Specimens with ungrouted flaw	10	1	0, 15, 30, 45, 60, 75, 90
	20	1	0, 15, 30, 45, 60, 75, 90
	30	1	0, 15, 30, 45, 60, 75, 90

In supplement to studying the cracking behaviour from the uniaxial compression tests, Le et al. (2018) obtained the uniaxial compressive strength (UCS), Poisson's ratio (ν), deformation modulus (E), cohesion, internal friction angle and tensile strength (σ_t) of the intact model material (cement mortar) and epoxy. These are listed in Table 2. Le et al. (2018) also tested the shear strength properties for surfaces of the ungrouted flaw (because the flaw walls can come into contact during loading) and the epoxy filled flaw. The ungrouted flaw surface had a cohesion, c_j of 0 Mpa and friction angle ϕ_j of 35.6°. For the grout infilled flaw surface, c_j and ϕ_j were 2 Mpa and 42.5° respectively.

The specimens were fitted with horizontal and vertical strain gauges, and loaded uniaxially on the shorter specimen edges until failure (Le et al., 2018). To minimize fabrication and recording errors, the test of each flaw geometry was repeated three times (on identical specimens).

Table 2: Material parameters for intact model material (rock-like material/cement mortar) and epoxy from Le et al. (2018).

	UCS (MPa)	E (GPa)	ν	ϕ (°)	c (MPa)	σ_t (MPa)
Intact specimen	42.0	19.6	0.18	41.6	10.0	4.1
Epoxy resin	62.8	1.2	0.45	21.9	30.2	22.6

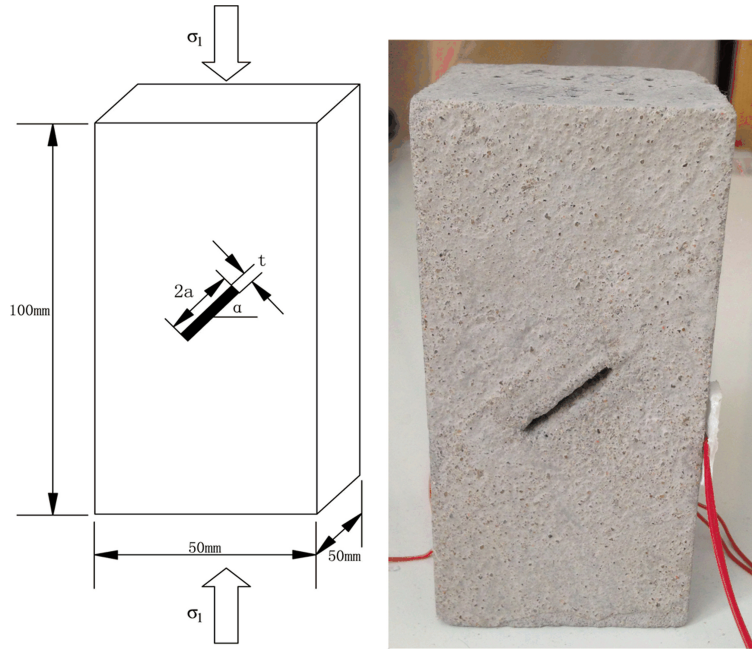


Figure 4: A sketch of the specimen geometry (left), and a specimen with an ungrouted flaw before subjected to uniaxial compression tests (right) (Le et al., 2018).

2.2 Strengthening effect and crack types from Le et al. (2018)

As described earlier, Le et al. (2018) loaded the specimens, which contained flaws with varying length and geometry, uniaxially until failure. In the uniaxial compression tests, Le et al. found that the failure mode and mechanical properties of the specimens were affected by both grouting, length and dip angle of the preexisting flaw. These results are presented in detail in the following sections.

2.2.1 Increased mechanical properties after grouting

The specimens with grouted flaws demonstrated higher UCS and deformation modulus than their non-grouted counterparts (Le et al., 2018). UCS for the specimens containing grouted and ungrouted flaws are given in Figure A1 in Appendix A. Moreover, the strengthening effect can be measured in terms of a strengthening factor D_s :

$$D_s = \frac{UCS_g - UCS_u}{UCS_u}, \quad (2)$$

where UCS_g and UCS_u are the UCS of the specimens containing a grouted and ungrouted flaw, respectively (of equal flaw geometry). Figure 5 plots D_s as a function of flaw dip angle for the three different flaw lengths (10 mm, 20 mm and 30 mm). As seen in the plot, the grouting reinforcement effect was most pronounced for the specimens containing the longer flaws. For the 10 mm flaws, the UCS-values were closer to the UCS of the intact specimen (42 MPa). Furthermore, the dip angle had the clearest effect on grout reinforcement for the 30 mm fracture. Regardless of flaw length, the strengthening factor was lowest for $\alpha = 90^\circ$. The next section moves on to presenting the crack types and failure modes that occurred in the specimens. Crack combinations explain why the flaw length and dip angle affect the strength improvement.

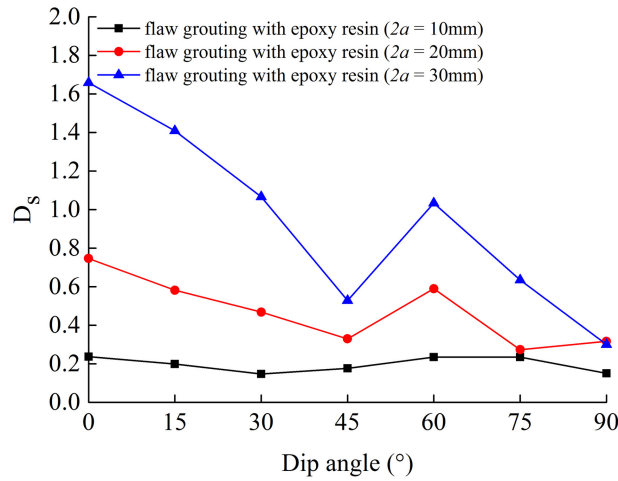


Figure 5: The strengthening factor D_s for grouting of flaws of varying length and dip angles (Le et al., 2018).

2.2.2 Crack types observed in grouted and ungrouted flaws

Coherent to expectations, Le et al. (2018) observed that the failure mode depended on the dip angle and length of the preexisting flaw, and whether the flaw was grouted or not. Further, the observed failure modes of the specimens were combinations of different crack types. Note that the term "flaw" refers to the preexisting flaw in the specimen. Moreover, the term "cracks" points to the fracture development in the specimen. In total, nine different crack types were observed in the study (Le et al., 2018). Table 3 presents the crack types, their initiation point and propagation pattern:

Table 3: Crack types observed by Le et al. (2018). The crack initiation point and crack development are described in the table. See Figures 6 and 7.

Crack name - type	Initiation point	Crack development
I-tensile	Flaw tip or close to flaw tip	First perpendicular to flaw, finally parallel to loading direction
II-tensile	Flaw tip or close to flaw tip	Parallel to loading direction
III-anti-tensile	Flaw tip	Finally parallel to loading direction
IV-shear	Tip of ungrouted flaw	Parallel to flaw plane
V-far-field tensile	Far from flaw	Almost parallel to loading direction
VI-surface spalling	Flaw tip and specimen edge	Small scale spalling (combined with tensile cracks)
VII-corner spalling	Specimen corner or edge	Large scale spalling (usually initiates after tensile cracks)
VIII-mid-flaw tensile	At grouted flaw, at midflaw	Parallel to loading direction, finally cuts through grouted flaw
IX-interface shear	Rock-grout interface	Parallel to flaw plane

Figures 6 and 7 present sketches of the crack types that occurred in specimens containing ungrouted flaws and specimens containing grouted flaws respectively. As seen in Table 3, crack type IV is a shear crack that developed from the tip of the ungrouted flaw along the flaw direction. This crack type only occurred in specimens with ungrouted flaws, and is thus only included in Figure 6. Furthermore, Le et al. (2018) discovered two new crack types — type VIII and IX. These are shown in Figure 7. Type VIII is a tensile crack that initiated at the grout infilled flaws, often at a distance away from the flaw tips. The tensile crack further propagated along the loading direction and cut through the grouted flaw. Type IX is a shear crack that occurred at the interface between the rock-like material and the grout, and propagated in the direction of the flaw. Type VIII and IX only occurred in specimens containing grouted flaws (Le et al., 2018).

2.2.3 Flaw geometry and filling and their effect on crack types

This section presents and compares the cracking behavior that occurred in the grouted and ungrouted specimens during the study by Le et al. (2018).

UngROUTED flaws

The crack types I-VII occurred in the unfilled flaw specimens (see Figure 6). No clear relation between far-field cracks and spalling (types V, VI and VII) and crack geometry was found for the unfilled flaws (Le et al., 2018). For most of the specimens containing an ungrouted flaw, tensile crack types II initiated first, followed by secondary cracks of types I-tensile, III-anti-tensile and/or IV-shear. In some cases, the anti-tensile crack was however the first appearing primary crack (Le et al., 2018). Moreover, a pronounced correlation between flaw length and cracking behaviour was found for the ungrouted specimens. For the specimens with the longest flaws ($2a=30$ mm), the distance to the lateral side is shorter, making it more likely for the primary tensile crack (II or III) to reach the lateral side of the specimens before initiation of secondary cracks (Le et al., 2018). For the 30 mm cracks with $45^\circ \leq \alpha \leq 75^\circ$, secondary cracks (IV-shear) appeared before the specimen failed. Table A1 in Appendix A gives an overview of the crack types that were observed for each combination of flaw length and dip angle by Le et al. (2018).

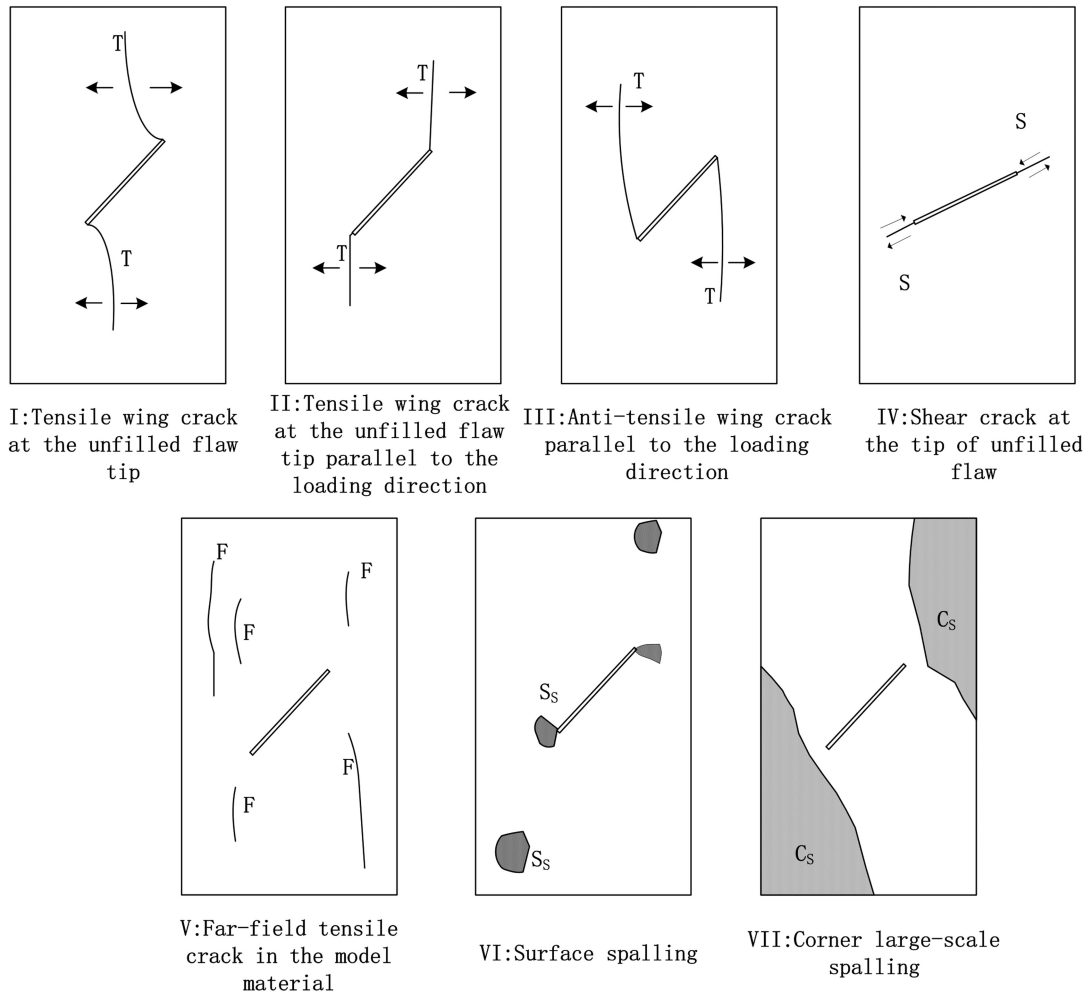


Figure 6: The crack types that were observed under uniaxial compression of specimens containing ungrouted flaws (Le et al., 2018). The shown crack types are tensile crack (T), shear crack (S), far-field crack (F), Surface spalling (S_s) and corner spalling (C_s).

Grouted flaws

In the specimens containing grouted flaws (as presented in Figure 7), the crack types I-II and V-IX occurred (Le et al., 2018). The length and dip angle of the grouted flaw was found to have no effect on the presence of spalling and far-field tensile cracks (types V-VII). For the specimens containing grouted flaws of length 10 mm, the failure mode was similar to the failure mode of the intact specimen. The dominating crack types in these specimens were far-field tensile cracks and spalling. Moreover, the crack developed in the lateral side of the specimen in some cases. Except for one specimen ($\alpha = 60^\circ$), tensile cracks did not initiate from the flaw tips of the grouted 10 mm flaws. Figure 8 presents the cracking behaviour of the intact specimen (no preexisting flaw) and two specimens with grouted 10 mm flaws (Le et al., 2018). Le et al. (2018) concluded that the grout effectively reduced the effect of the flaw for short flaw lengths.

Tensile cracks of type I, II and III did not occur in every grouted specimen, as opposed to the specimens containing ungrouted flaws. In fact, anti-tensile cracks (type III) never occurred in the grouted specimens. For some specimens ($\alpha = 60$ and 75°), tensile cracks of type I and II still dominated the critical failure plane, combined with shear cracks of type IX (grout-rock interface). In the other cases, coalescence of far field tensile cracks (type V), mid-flaw tensile cracks (type VIII) and spalling (type VI and VII) established the critical failure plane (Le et al., 2018). Table A2 in Appendix A presents an overview of the observed crack types in specimens containing grouted flaws.

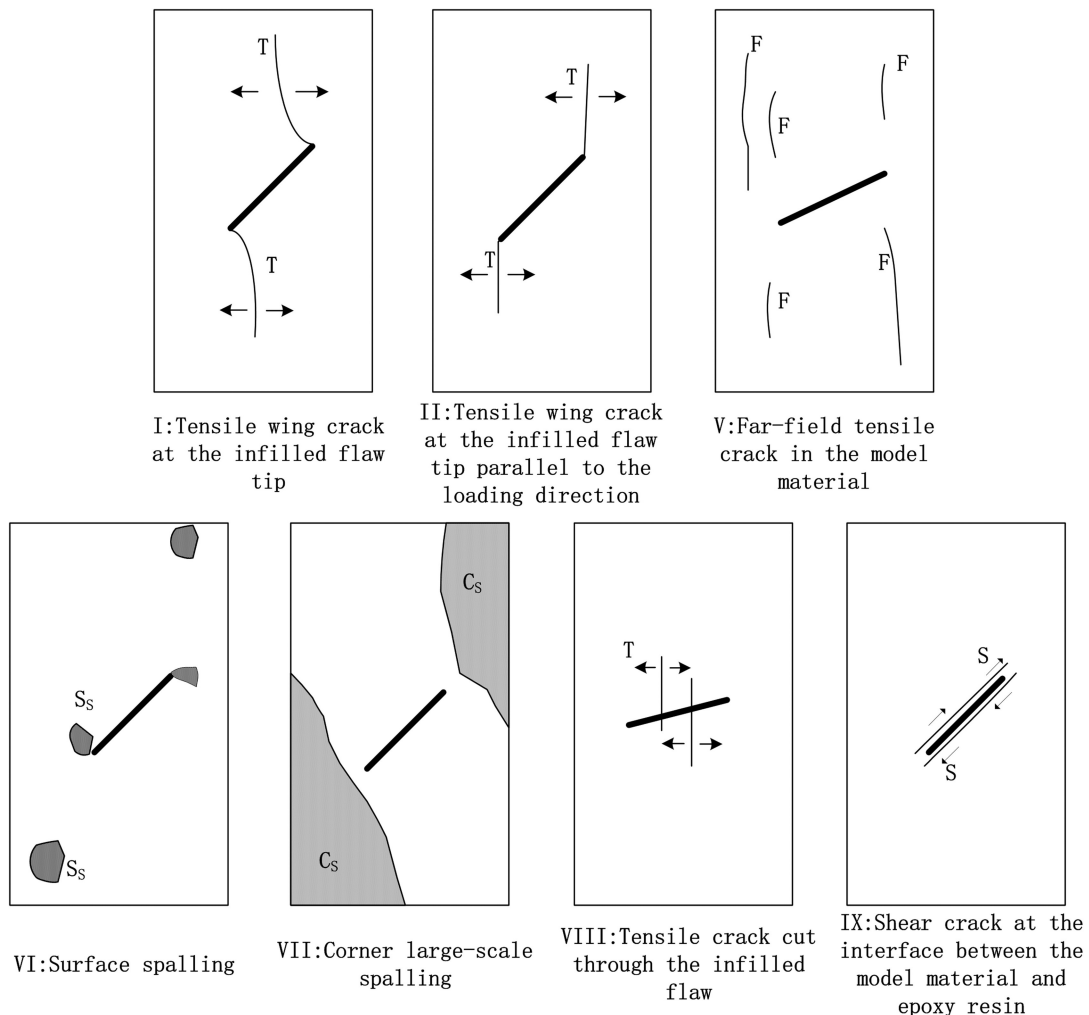


Figure 7: The crack types that were observed under uniaxial compression of specimens containing grouted flaws (Le et al., 2018). The shown crack types are tensile crack (T), shear crack (S), far-field crack (F), Surface spalling (S_s) and corner spalling (C_s). (Because type III was not observed in grouted specimens, the type III sketch was edited out of the original image from Le et al. (2018))

Comparison of cracking behaviour around grouted and ungrouted flaws

As described in the previous section, grouting both changes the cracking behaviour of specimens containing geometrically equal flaws and improves the mechanical properties of the specimen (Le et al., 2018). In the specimens with unfilled flaws, tensile cracks initiated at or close to the flaw tips in every case. However, in the grouted specimens, tensile cracks often initiated at the mid-section of the flaw. Le et al. (2018) thus concluded that grouting can reduce the stress concentration at flaw tips. Figure 9 compares the cracking behaviour of grouted and ungrouted specimens containing a 20 mm long flaw with a dip angle of 30° . The grouted specimen exhibits failure caused by type VIII-tensile cracks and spalling. The critical damage of the ungrouted specimens is caused by type II-tensile cracks. Moreover, the grouted specimen failed at an applied uniaxial load of *ca.* 40 MPa, while the ungrouted specimen failed at *ca.* 27 MPa (Le et al., 2018).

Grouting was found to change the crack-initiation position and coalescence pattern (Le et al., 2018). The strengthening effect from grouting was most pronounced for the specimens containing the longest flaws (30 mm) and lowest angles ($\alpha \leq 30^\circ$). As Le et al. (2018, p. 1) concludes: "Grouting improves the strength of grouted specimens through the following two mechanisms: (1) by increasing the shear-strength parameter values of the interface between the grout and model material and (2) by reducing the stress concentration at the flaw tips."

The uniaxial compressions tests by Le et al. (2018) lay the groundwork for the numerical analyses performed in this thesis. The chapters that follow move on to the theory and methodology behind the performed finite element analyses.

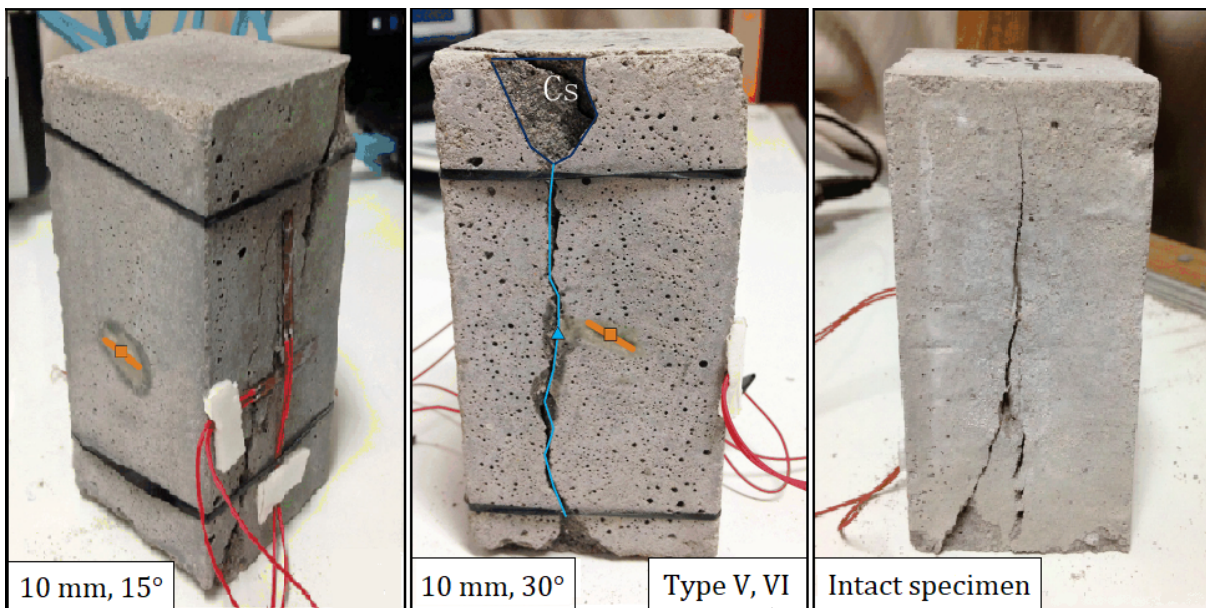


Figure 8: Failure modes for specimens with short grouted flaws (left and middle) and intact specimen (right) (edited after Le et al. (2018)). The cracking behaviour for the specimens containing grouted 10 mm flaws were similar to the cracking of the intact specimen. C_s is corner spalling, blue line marks tensile crack, orange line highlights grouted flaw.

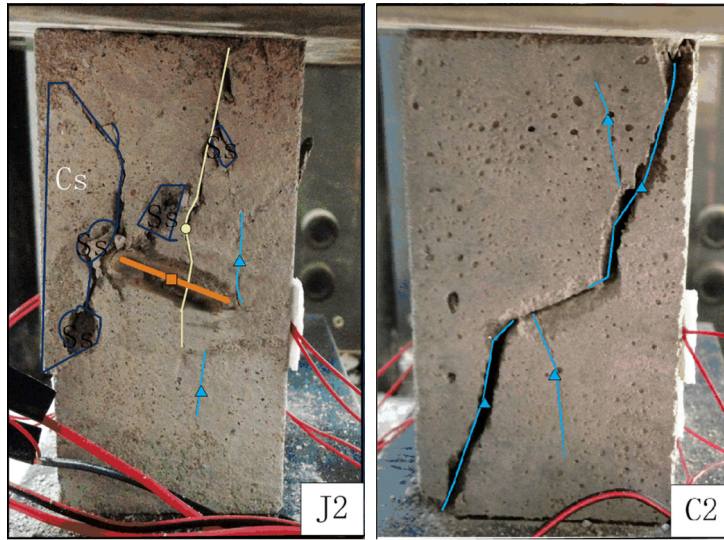


Figure 9: Specimens containing grouted flaws (left) and ungrouted flaws (right) of dip angle 30° and length 20 mm (Le et al., 2018). Yellow line marks the type VIII tensile crack.

3 The Finite Element Method

The finite element method is a versatile tool that can be applied to problems in a variety of fields — from structural problems, such as loading of a rock, to *e.g.* fluid dynamics or acoustics. In a structural analysis, FEM takes a structure, splits it into smaller elements of simple shapes and calculates the nodal displacements, which are the primary unknown variables (Kurowski, 2004). FEM is a popular and versatile method for structural problems. The method allows easy adjustment of for example model geometry, material parameters and loading conditions, and FEM was therefore chosen for this project.

This chapter gives a brief introduction to the basic theory behind a structural finite element analysis (structural FEA). Finally, the two FEM codes Abaqus and RS2 are presented.

3.1 Basic FEM principles

In FEA, the solution domain is defined with a mesh. The mesh divides the structure geometry into elements, which are joined together by shared nodes (Kurowski, 2004). The mesh can be considered an assembly of linear elastic springs connected at the nodes (Ottosen and Petersson, 1992). For one individual spring, the relation between an applied force, f , and the displacement, u_s , is governed by the spring stiffness, k :

$$f = ku_s. \quad (3)$$

At each node, and in the meshed system, there is static equilibrium between the applied nodal forces and internally generated nodal forces. For an assembly of nodes, equilibrium between the external forces $[F]$ and internal forces $[I]$ can be expressed as follows (Dassault Systèmes, 2014):

$$[F] - [I] = [0]. \quad (4)$$

A schematic drawing of the applied external load and the internal nodal forces for a meshed structure is given in Figure 10. In the drawn case, at the internal nodes, the sum $\sum_{i=1}^6 I_i$ alone equals 0.

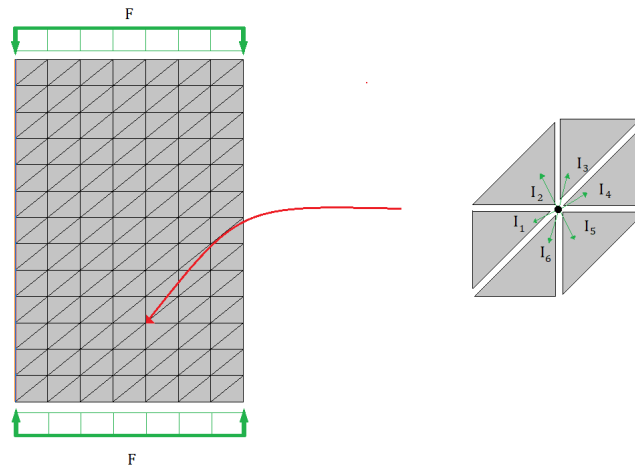


Figure 10: Schematic drawing of the external forces applied on a meshed structure (F) and the internal forces at the nodes (I).

Equation systems expressing force equilibrium, stiffness properties, and nodal displacement are established for the entire mesh (Ottosen and Petersson, 1992). The total system of equations — and the fundamental FEM equation — can be expressed as

$$[F] = [K] \cdot [u], \quad (5)$$

where $[F]$ is the known vector of total force, $[K]$ is the known total stiffness matrix and $[u]$ is the unknown vector of nodal displacements (Kurowski, 2004). For a linear-elastic system, the numerical solution is obtained from calculation of one system of equations (Dassault Systèmes, 2014).

The stiffness matrix $[K]$ depends on the model geometry, material properties and boundary conditions. In a linear-elastic problem, E and ν define the material behaviour completely (Kurowski, 2004). Moreover, boundary conditions are known displacements/loads or constrains against translation or rotation of the rigid body. If $[K]$ is singular ($\det[K] = 0$), no unique solution of the system of equations exists. This can be seen as rigid body motion (Dassault Systèmes, 2014). To achieve a unique numerical solution, boundary conditions must therefore be defined.

When the nodal displacements are computed, stress and strain values for each element can be found. In a linear-elastic system, the material response can be described by Hooke's law (Ottosen and Petersson, 1992). In a one-dimensional stress state, Hooke's law gives:

$$\sigma = E\epsilon, \quad (6)$$

where the strain, ϵ , can be expressed

$$\epsilon = \frac{du}{dx}. \quad (7)$$

In two- or three-dimensional stress states, Eq. 6 and Eq. 7 are expressed with tensors. For a one-dimensional problem, for example the loading of an elastic bar with a length L and cross-sectional area A , force equilibrium is given by the second-order ordinary differential equation:

$$\frac{d}{dx} \left(AE \frac{du}{dx} \right) + b = 0; \quad 0 \leq x \leq L, \quad (8)$$

where b is the bulk force per unit length (Ottosen and Petersson, 1992). Once boundary conditions are given, Eq. 8 can conveniently be solved numerically. This emphasizes the importance of properly defined boundary values in FEA.

3.2 Solving nonlinear numerical problems

The previous section presented principles for linear-elastic numerical problems. For many structural problems, including rock specimen analyses, a linear-elastic material behaviour assumption is not adequate. In structural FEA, there are different sources of nonlinearity, including:

- Nonlinear materials — the material follows a nonlinear load/displacement curve (Kurowski, 2004).
- Nonlinear geometry — the geometry changes the structure stiffness during the analysis (Kurowski, 2004).
- Nonlinear boundaries — the boundary conditions change during the analysis (Dassault Systèmes, 2014).

This section briefly presents material nonlinearity. Elasto-plastic materials are an example of materials that exhibit a nonlinear load-displacement response (see Figure 11). Elasto-plastic models are defined with a yield stress, where the material behaves as an linear-elastic material until the yield stress is reached and the material starts to deform permanently (Kurowski, 2004). In FEM software, the yield stress can be defined with a failure criterion with various input parameters, such as the MC-criterion. The chosen failure criterion marks each element to be either yielding or elastic, and the stress over the yielded elements is redistributed to elastic elements (Griffiths and Lane, 1999).

The following subsections explain how variations of Newton's method calculate the solution to nonlinear numerical problems.

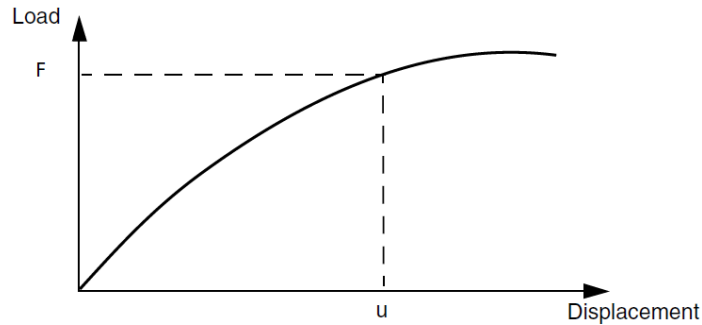


Figure 11: Nonlinear load/displacement curve from Dassault Systèmes (2014) (variable names have been modified).

3.2.1 The Newton-Raphson method

The Newton-Raphson method is a variation of Newton’s method (Dang et al., 2014). The following paragraphs aim to explain how the Newton-Raphson method calculates the numerical solution to a non-linear structural problem. Examples of the convergence criteria from the Abaqus/Standard code documentation (Dassault Systèmes, 2014) are included. In different FEM codes however, the details and principles for calculating and accepting numerical solutions may vary from the given examples.

With the Newton-Raphson method, the numerical solution of a nonlinear structure model is computed by dividing the applied load into *increments* — smaller portions of the loading step (Dassault Systèmes, 2014). Within each increment, *iterations* are run to find the displacement that gives an acceptable equilibrium between the applied and internal loads.

The first Newton-Raphson iteration takes the smaller load increment, ΔF and the initial stiffness, K_0 and returns a displacement correction, c_a . Following, an updated displacement u_a is calculated:

$$u_a = u_0 + c_a, \quad (9)$$

where u_0 is the initial displacement. At u_a , the updated internal force I_a and an updated stiffness K_a are calculated (see Figure 12). Convergence criteria are then used to control the solution u_a .

In Abaqus/Standard, there are two criteria for accepting the incremental response (Dassault Systèmes, 2014): (1) the approximate equilibrium is accepted when the c_a is sufficiently small compared to the total incremental displacement (Δu_a):

$$c_a < \Delta u_a \cdot 1\%, \quad (10)$$

and (2) the incremental force residual, R_a is smaller than a tolerance value (tol),

$$R_a = F - I_a < tol. \quad (11)$$

In Abaqus/Standard, $tol = 0.5\%$ of the time-averaged force in the structure by default (Dassault Systèmes, 2014).

If the equilibrium is not accepted, the Newton-Raphson method attempts new iterations, using the updated stiffness K_a and R_a . This gives a new displacement correction value and subsequently a new displacement. This solution is again checked against the convergence criteria (Equations 10-11). This process is repeated until an increment converges or the calculations are stopped because a maximum amount of iterations is reached. Consequently, the stiffness matrix $[K]$ is continuously updated during the iterations in the Newton-Raphson method. Finally, the numerical solution for the loading step is the sum of the responses from each increment — if equilibrium is accepted within the specified tolerance (Dassault Systèmes, 2014).

For stable systems, Newton-Raphson is a method able to converge with low computational cost (small number of iterations). In cases with excessive plasticity/yielding, the Newton-Raphson method is less

robust compared to other variations of Newton’s method (Dang et al., 2014). Other variations of Newton’s method are briefly presented in the following subsection.

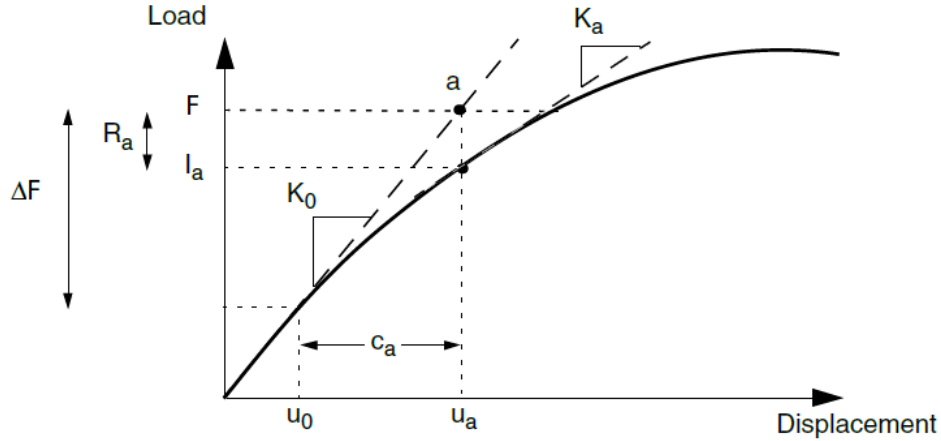


Figure 12: The first iteration with the Newton-Raphson method, from Dassault Systèmes (2014) (variable names have been modified).

3.2.2 The initial stiffness method and accelerated initial stiffness method

The initial stiffness method is another variation of Newton’s method. Unlike the Newton-Raphson method, the initial stiffness method uses the initial stiffness matrix, K_0 , and keeps it constant throughout the iterations (Dang et al., 2014). The next paragraphs outline the iteration process in the initial stiffness method.

The initial stiffness method calculates updates values of nodal displacements and internal forces through iterations. At the i -th iteration, the displacement correction ΔU_i can be calculated by (Dang et al., 2014):

$$\Delta U_i = K_0^{-1} R_{i-1}. \quad (12)$$

R_{i-1} is the force residual at the current iteration and K_0 is the stiffness of the initial displacement state. The force residual is again given by the difference between the external and internal forces. When ΔU_i is known, the total displacement U_i at the current iteration can be found by (Dang et al., 2014):

$$U_i = U_{i-1} + \Delta U_i, \quad (13)$$

where U_{i-1} is the known displacement for the previous iteration. New iterations are attempted until the force residual is sufficiently small. During the iterations U_i approaches the true solution within the specified error tolerance.

Compared to the Newton-Raphson method, the initial stiffness method may require a high number of iterations. However, the initial stiffness method can be a robust method for dealing with severe plasticity problems (Dang et al., 2014).

The accelerated initial stiffness method is a modification of the initial stiffness method. This method uses an acceleration parameter (α) that scales ΔU_i in the iterations (Dang et al., 2014). Dang et al. (2014) developed a variation of the accelerated initial stiffness method. Moreover, the performance of the accelerated initial stiffness method (using $\alpha \in [0.1 - 10]$) was evaluated by comparing the number of iterations and computation time that the accelerated initial stiffness method and other algorithms (including the non-accelerated initial stiffness method) spent when solving 4 different three-dimensional FEA tasks. The solved tasks were *e.g.* simulation of a cylindrical hole excavated in an elastoplastic Mohr-Coulomb-medium under a constant initial stress field, and determination of the bearing capacity of an axially loaded pile in cohesionless soil. In their study, Dang et al. (2014) found that the accelerated initial stiffness method reduced the required number of iterations and computation time by up to 80% and 77% respectively (compared to the non-accelerated initial stiffness method).

3.3 Shape functions and mesh refinement tests

In FEA, each element is described with a shape function — a function that takes the nodal displacements and returns the displacement field within the element (Kurowski, 2004). The shape functions are typically polynomials (P) of a defined order (n):

$$P(x) = \alpha_0 + \sum_{i=1}^n \alpha_i x^i,$$

where $\alpha_0, \alpha_1, \dots, \alpha_n$ are constants. The most rudimentary elements follow a linear shape function (first-order elements). For first-order elements, the strain and stress values are constant within the element. In FEM-software however, averaging-algorithms are often used to display a continuous stress field within elements, even when first-order elements are used. Moreover, second-order elements follow a quadratic shape function, and give a linear stress distribution within the elements. Further, higher order shape functions can be used (Kurowski, 2004).

According to Kurowski (2004), the shape functions must meet certain requirements, including:

- shape functions are continuous over the entire element; and
- shape functions do not overlap other shape functions at edges shared with several elements.

In two dimensions, each node has two degrees of freedom (DOF) — translation in the first and second direction. Moreover, a first order triangular element can have up to 3 nodes and 6 DOFs. In second order elements, nodes are allowed at the element midsides as long as at the element corners. A second order triangular element can therefore have up to 6 nodes and 12 DOFs (Kurowski, 2004). In other element types, the nodes can be enriched with extra DOFs. Examples are translation in the third direction and rotations around the three axes (Dassault Systèmes, 2014).

The mesh resolution can be described by both the order of the element shape functions or the total amount of elements. In FEA, the resolution of the mesh can be increased to study the convergence of *e.g.* maximum stress magnitudes. Mesh refinement can be done with a h-refinement test or a p-refinement test. In h-refinement, the total number of elements in the mesh is gradually increased (and shape function order remains constant) (Kurowski, 2004). Conversely, a p-refinement test increases the order of the element shape function (and keeps the number of elements constant) (Kurowski, 2004).

3.4 Commercial FEM codes

In this thesis, the FEM programs RS2 and Abaqus were used, which are developed by Rocscience Inc. and Dassault Systèmes Simulia Corp, respectively. This section presents and compares the two programs. Some important features are summarized in Table 4.

3.4.1 Abaqus

The Abaqus package consists of three analysis products:

- Abaqus/Standard — an implicit general purpose numerical tool;
- Abaqus/Explicit — an explicit numerical tool for dynamic problems; and
- Abaqus/CFD — a tool developed for fluid dynamic problems.

Abaqus/Standard (Dassault Systèmes, 2017) has been used in this study. The program is developed for a wide range of numerical problems, and therefore offers well-developed and versatile modules for designing and executing the necessary FEM steps. These include geometric design, material parameters, boundary conditions, loading, meshing, computation and result visualisation.

Both 2D and 3D structures can be modelled in Abaqus/Standard. The selection of element types are vast. Examples are cohesive elements, continuum elements or beam elements. In 2D analysis, the elements can assume *e.g.* plane strain or plane stress conditions. Element shape functions can be linear or quadratic.

Material parameters can be applied to different model sections via a variety of implemented failure criteria, including the MC-criterion. In Abaqus/Standard, the post-yield curve coordinates must be specified by the user (Dassault Systèmes, 2014). Any consistent unit system can be used in Abaqus, as no unit is specified in the parameter input and result output.

Abaqus/Standard uses the Newton-Raphson method to implicitly find the numerical solution of the studied problem. In an implicit algorithm, the increments are solved simultaneously. Additionally, the program offers possibilities for automatic stabilization (stopping criteria) for unstable problems: specification of a dissipated energy fraction or specification of a damping factor (Dassault Systèmes, 2014).

3.4.2 RS2

RS2 (Rocscience Inc., 2021b) is developed for structural rock and soil problems, such as tunnel or slope analyses. The different FEM modules therefore come with settings that are commonly used in rock and soil problems, and the program can therefore be considered less versatile. For example, the CAD-module offers few tools to draw complicated geometries. On the other hand, the user can choose from a variety of different tunnel contours and easily adjust and add them to the model.

RS2 offers 2D plane strain analysis, or computation of axisymmetric 3D (a 2D structure geometry is rotated around an axis, (Rocscience Inc., 2021a)). Both continuum elements and cohesive elements (labelled "joint elements") can be assigned to the structure. Linear and quadratic shape functions are available in RS2 (Rocscience Inc., 2021b).

Some of the failure criteria and material descriptions that are implemented in RS2 are often used within rock engineering. Examples are The Hoek-Brown criterion, Generalized Hoek-Brown criterion and the MC-criterion. In RS2, the entered parameters must follow either the metric or imperial system (Rocscience Inc., 2021b).

The initial stiffness method, or the accelerated initial stiffness method can be chosen to calculate the numerical solution (Rocscience Inc., 2021c). Several stopping criteria are implemented in RS2. Stopping criteria force the program to accept the equilibrium. These criteria let the user define a tolerance of energy, force and/or displacement that will end the iterations faster (Rocscience Inc., 2021b).

Table 4: Comparison of RS2 and Abaqus/Standard features.

Feature	RS2	Abaqus/Standard
Application	Structural rock/soil analysis	General-purpose
Iteration method	Initial stiffness, accelerated initial stiffness	Newton-Raphson
Model dimensions	2D	2D, 3D
Shape functions	Linear, quadratic	Linear, quadratic
Element families	Cohesive (joint), 2D plane strain, axisymmetric	Cohesive, 3D stress, 2D plane stress, 2D plane strain
Unit system	Predefined systems (metric or imperial)	Any consistent unit system
CAD-module	Basic	Versatile

4 Methodology

The simulations that were performed in this thesis set out to simulate uniaxial compression tests of specimens containing unfilled and grouted open flaws. The 2017-version of Abaqus/Standard (Dassault Systèmes, 2017) and version 11 of RS2 (Rocscience Inc., 2021b) were used. The uniaxial compression tests were done through several simulation sets (tasks) to assess different research objectives. These are outlined in the following Table 5. This chapter presents how the different models and tasks were performed.

Table 5: An overview of the different simulation sets that were performed in Abaqus/Standard (ABQ) and/or RS2.

Numerical task	Task description	RS2	ABQ
Experimental design (2D)	The 42 geometry combinations that are listed in Table 1 were tested for the purpose of examining the stress state and yielding behaviour of specimens with different 2D flaw geometries.	✓	×
Code validation (2D)	19 flaw geometries (including models with no flaw) were tested in two programs in 2D to compare the programs.	✓	✓
2D/3D validation	1 flaw geometry was tested in 2D and 3D for validation purposes.	×	✓

4.1 Experimental design (2D)

This part of the project included repeated uniaxial compression tests on flaws with varying geometries, grouted and non-grouted. The simulations were done in two dimensions to reduce computational cost. Several models were made both in Abaqus/Standard (ABQ) and RS2. RS2 was eventually considered the most suitable code, for three reasons: (1) advanced stopping criteria are implemented in the code, (2) it uses the accelerated initial stiffness method, which is expected to be robust in severe yielding cases and (3) it returns specific information about the yield type (shear and/or tension).

However, the first 18 2D models were designed in ABQ. These first simulations indicated that stress singularities and severe plasticity could be a challenge in this thesis work. During these simulations, ABQ demonstrated convergence problems when computing the nonlinear models — the models did not converge with the desired elastoplastic material properties. Consequently, the models had to be rebuilt in RS2, even though a considerable amount of time (approximately 30 days) had been spent on designing two-dimensional ABQ models. Further, this section — and all sections related to the 2D experimental design task — exclusively presents information from the RS2 models. The next sections outline the details in the RS2 models: from geometry, material properties, boundary conditions to the mesh.

4.1.1 Experimental design — geometry

The numerical models aimed to copy the geometry of the specimens that are shown in Table 1 and Figure 4. Two-dimensional models of 50 mm wide and 100 mm tall specimens with grouted or ungrouted flaws of varying α and $2a$, and a thickness, $t = 1$ mm, were designed. Figure 13 shows that α is the angle between the horizontal x-axis and the long sides of the flaws. Moreover, the midpoint of the flaw (mid-length and mid-thickness) is located at the origin of the model coordinate system. The midpoint of the flaw is also the midpoint of the specimen. Thus, the outer boundaries of the specimen are a rectangle with opposite corner coordinates $(-0.025, -0.050)$ and $(0.025, 0.050)$ in metres — which is the available length unit in RS2. To reduce stress singularities, the corners of the flaw were rounded with quart-circles with a radius of 0.3 mm (4 line segments). In every case, $t = 1$ mm.

All combinations of $\alpha = [0, 15, 30, 45, 60, 75, 90]^\circ$, $2a = [10, 20, 30]$ mm, grouted and ungrouted were tested. The model shown in Figure 13 is grouted. An Excel algorithm based on basic trigonometric principles was made to return flaw vertices coordinates from the input of α and $2a$. These coordinates were imported to material boundary creator in RS2. For each flaw geometry, both an ungrouted model (where the section within flaw boundary was excavated) and a grouted model (where the section within

flaw boundary was assigned epoxy material) were made. The remaining part of the model was assigned rock-like material (rock) properties.

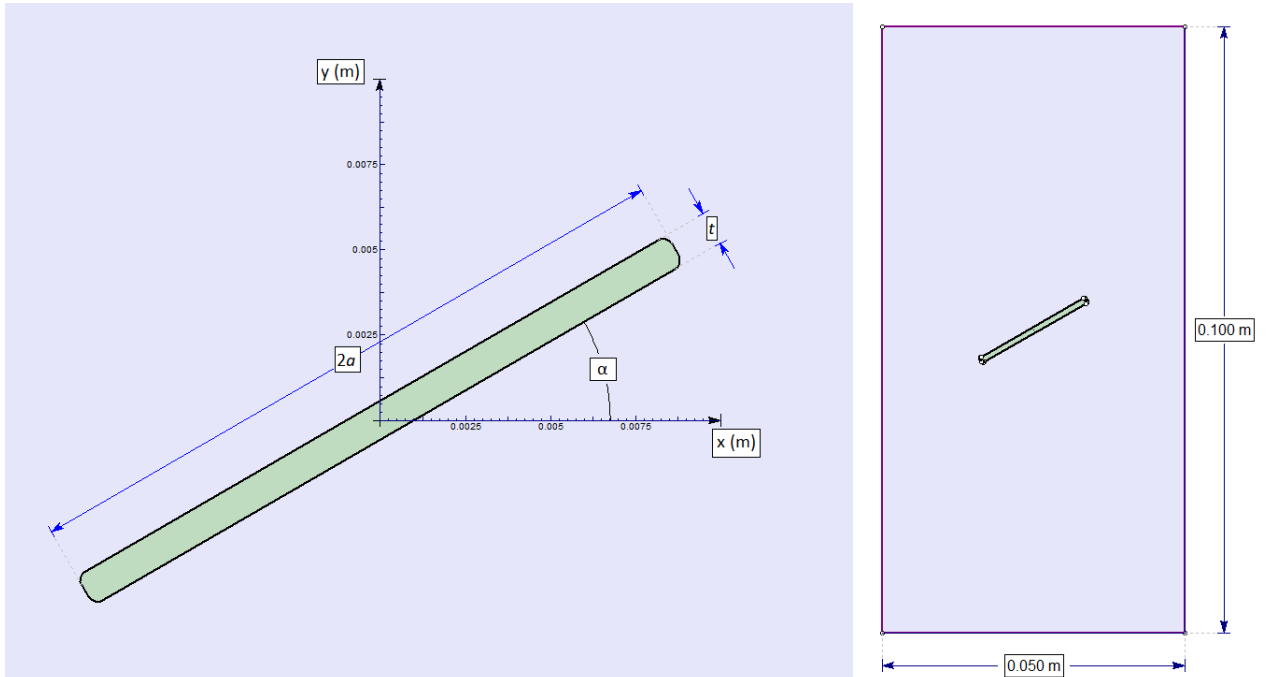


Figure 13: Flaw details for the two-dimensional models. The left figure shows the detailed flaw geometry, the right figure show the whole specimen.

4.1.2 Experimental design — material properties

In the current simulation set, the material properties were kept equal for all the models. However, each model was tested with both elastoplastic and linear-elastic material properties — *i.e.* two simulations were done for each model. In the elastoplastic models, severe yielding redistributed the stress concentrations around the flaw. Therefore, it was chosen to also investigate the stress field around the flaw using linear-elastic material properties. The MC-criterion was used, and the material properties are taken from Table 2. Table 6 summarizes the Poisson’s ratio, Young’s modulus and peak and residual (res.) Mohr-Coulomb parameters for the elastoplastic and linear-elastic material models (ψ is the dilation angle). The residual strength values of the elastoplastic materials were set to 0 MPa and 0° to model a brittle post-peak behaviour.

One simulation (the model containing a grouted flaw with $2a = 30$ mm and $\alpha = 30^\circ$) was repeated with the material ”Epoxy B (Plastic)” assigned to the flaw. This was done to investigate whether a high Poisson’s ratio could induce additional yielding around the flaw.

Table 6: Material properties experimental design.

Material	Colour	E-modulus (MPa)	ν	Peak σ_t (MPa)	Peak ϕ ($^\circ$)	Peak c (MPa)	Res. σ_t (MPa)	Res. ϕ ($^\circ$)	Res. c (MPa)	ψ ($^\circ$)
Rock (Elastic)		19600	0.18	-	-	-	-	-	-	-
Epoxy (Elastic)		1200	0.45	-	-	-	-	-	-	-
Rock (Plastic)		19600	0.18	4.1	41.6	10	0	0	0	0
Epoxy (Plastic)		1200	0.45	22.6	21.9	30.2	0	0	0	0
Epoxy B (Plastic)		1200	0.20	22.6	21.9	30.2	0	0	0	0

4.1.3 Experimental design — load and boundary conditions

In this simulation set, loading was applied in the boundary conditions. The gravitational stress contribution (specimen weight) is low (<1 Pa), and is thus neglected in the models. Figure 14 shows mesh and boundary conditions for a model example (grouted model with $\alpha = 30^\circ$ and $2a = 20$ mm). A displacement of 0.10 mm in negative y-direction was added on the top plate, for all the models (blue lines in Figure 14). The computed total reaction force in the top nodes were about 1.0 MN, which equals an average compressive load of 20 MPa. Furthermore, the bottom plate was restrained in y-direction (red circles in Figure 14). To prevent rigid body motion, the lower right corner of the specimen was fixed in both x- and y-direction (red triangle in figure 14). The side edges of the specimen were not restrained in any direction. A free body diagram for the loading condition is given in Figure 10.

One ungrouted model ($2a = 20$ mm, $\alpha = 0^\circ$) was also tested with a lower applied load (-0.05 mm which equals 8 MPa) to examine where the first yielding initiated. Moreover, one grouted model ($2a = 10$ mm, $\alpha = 0^\circ$) was tested with a higher applied load (-0.14 mm which equals 28 MPa) to investigate which secondary yielding patterns that developed.

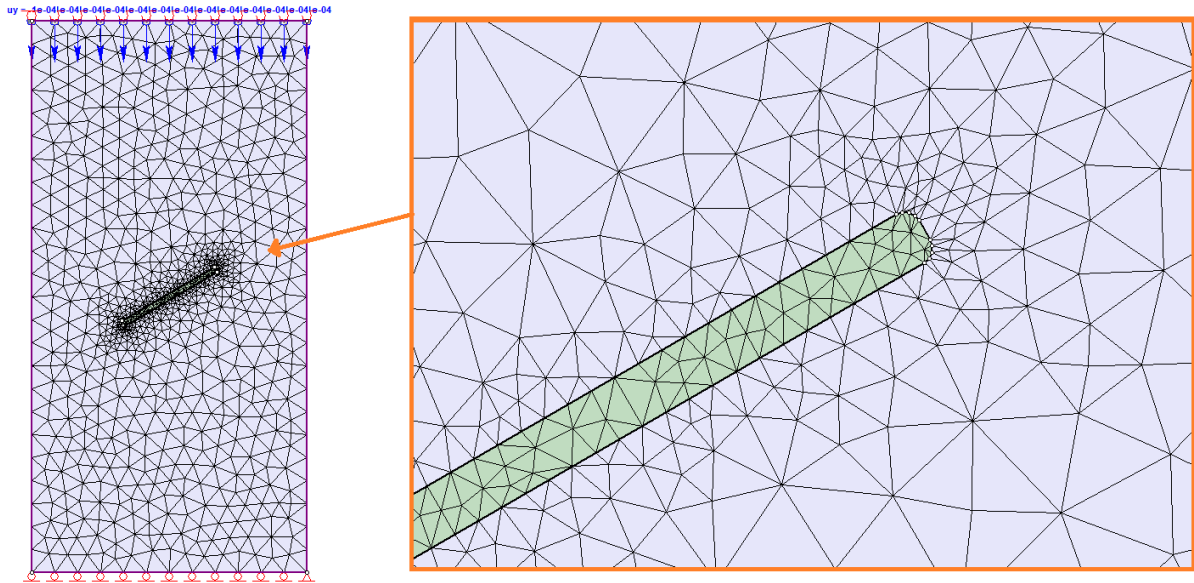


Figure 14: The mesh and boundary conditions for a model example is shown. The model contains a grouted flaw with $\alpha = 30^\circ$ and $2a = 20$ mm. The top plate was assigned a constant displacement of -0.10 mm (blue arrows), and is free to translate along the x-direction (hence both red circles and displacement symbols are shown). Red circles indicate that nodes can translate in x-direction. Red triangle indicates that node is restrained in x- and y-direction.

4.1.4 Experimental design — mesh

For all the models in this set, plane strain 3-noded triangles (first order elements) were assigned to the entire structure. An example of a meshed model is given in Figure 14. It was aimed to keep approximately the same mesh density in all models. The same discretization intervals were therefore used on the top and bottom edges (12 segment discretizations/elements), and on the right and left side edges (24 segment discretizations), for all models. For the long sides of the flaws, 20, 40 and 60 segment discretizations were used on the flaws of lengths 10 mm, 20 mm and 30 mm respectively (*i.e.* 20 discretizations per 10 mm flaw length). 4 discretizations were placed on the quart circles to include the curved geometry. The remaining part of the short flaw side was described with 1 element. Further, the mesh was constructed with the RS2 automesh. The meshes used in the ungrouted and grouted models with equal flaw geometries were identical around the flaw (except from within the flaw, where the ungrouted open flaw has no elements). This can be seen in Figure 15. The total number of elements assigned to the flaw and rock section for each model is included in Tables B3 (ungrouted models) and B4 (grouted models) in Appendix B.

4.1.5 Experimental design — other settings

The default analysis settings in RS2 were used. This means that the accelerated initial stiffness method was used to solve the iterations. The used stop criteria are comprehensive — meaning that the solution is accepted when there is an approximate equilibrium in both energy, force and displacement, with a tolerance of 0.001. The simulations were run in one loading stage.

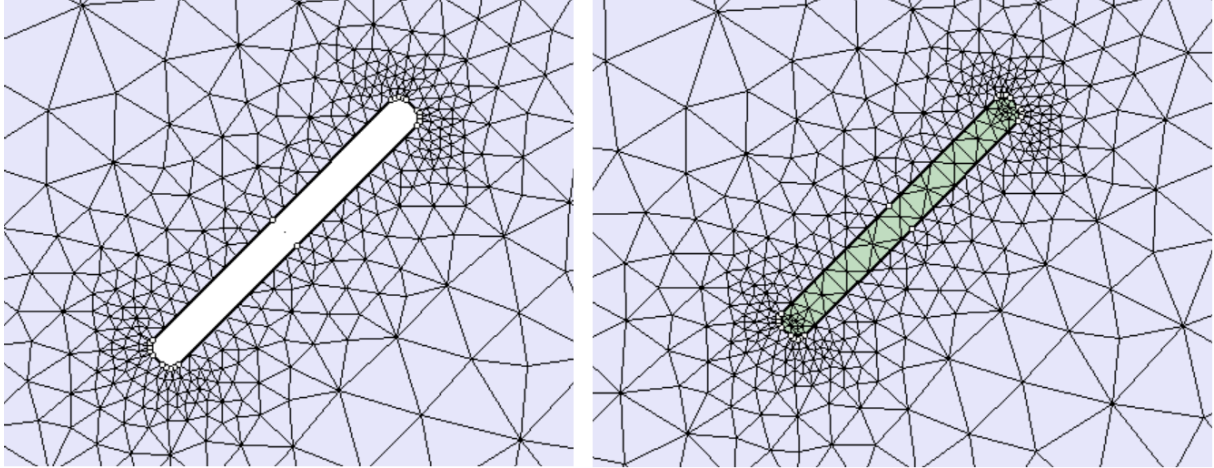


Figure 15: The mesh for models containing an ungrouted (left) and a grouted flaw (right) is reused ($2a = 10$ mm, $\alpha = 45^\circ$).

4.2 Code validation (2D)

Before attempting to recreate the 2D models from in RS2 as 3D models in ABQ, it was decided to compare two-dimensional results from ABQ and RS2. This makes it easier to describe the differences from the programs, and could also serve as a validation of the RS2 results. This lays out the motivation behind the code validation task. This section moves on to describing how these models were made.

As mentioned above, the purpose of the code validation simulations was to compare results from the codes ABQ and RS2. Uniaxial compression tests were therefore simulated in both programs under similar conditions. In this task, models that were suitable for both programs had to be designed. Therefore, some modifications were made to the 2D models that were described in the experimental design sections. This section describes the model details for the code validation simulations in ABQ and RS2, and briefly argues why changes were made.

4.2.1 Code validation — geometry

RS2 only allows 2D-modelling. Therefore, the models that were compared in ABQ and RS2 were two-dimensional. Further, the geometric models used in this task were the same as described in Section 4.1.1 and Figure 13. The unit systems are however different in ABQ and RS2, and the used length and stress units in ABQ were mm and MPa respectively (compared to m and MPa in RS2). 9 different combinations of flaw length and dip angles were simulated, and both grouted and ungrouted models were tested. Additionally, an intact model (with no flaw) was examined in each program. This makes up 19 models in each program. These are described in Table 7.

Table 7: The flaw geometries ($2a$ and α) for the tested models in the code validation task, and the total number of elements in the mesh. Intact models (without flaws) were also tested.

Geometry		Total elements (ABQ)	Total elements (RS2)
Intact specimen	N/A	576	1000
UngROUTED flaw	0°	2120	1574
2a=10 mm	30°	2312	1501
	60°	2222	1498
UngROUTED flaw	0°	2334	1806
2a=20 mm	30°	2620	1686
	60°	2696	1686
UngROUTED flaw	0°	2690	1874
2a=30 mm	30°	3240	1955
	60°	3152	1950
GROUTED flaw	0°	2208	1704
2a=10 mm	30°	2128	1638
	60°	2372	1628
GROUTED flaw	0°	2486	1994
2a=20 mm	30°	2782	1888
	60°	2848	1888
GROUTED flaw	0°	2908	2152
2a=30 mm	30°	3206	2244
	60°	3360	2236

4.2.2 Code validation — material properties

In this task, it was aimed to keep the material properties equal for each model in ABQ and RS2. The MC-criterion is implemented in both programs, and was chosen for this task. Several attempts of creating stable brittle material models in ABQ were done. During these attempts, the effects of different residual values of the MC-parameters, were tested. However, the ABQ-models — which were solved with the Newton-Raphson iteration method — demonstrated challenging convergence problems. Thus, it was chosen to use elasto-perfect-plastic material behaviour in this task, which was found to be the most numerically stable material model. Additionally, linear-elastic material models were tested. The parameters for the elastoplastic and linear-elastic material models that were simulated in ABQ and RS2 are given in Table 8. For the rock material, $\psi = 25^\circ$ was chosen to increase the stability of the models. Additionally, the peak and residual σ_t were increased to 6 MPa due to convergence difficulties in ABQ.

Table 8: Material properties code validation.

Material	E-modulus (MPa)	ν	Peak σ_t (MPa)	Peak ϕ (°)	Peak c (MPa)	Res. σ_t (MPa)	Res. ϕ (°)	Res c (MPa)	ψ (°)
Rock (Elastic)	19600	0.18	-	-	-	-	-	-	-
Epoxy (Elastic)	1200	0.45	-	-	-	-	-	-	-
Rock (Plastic)	19600	0.18	6.0	41.6	10	6.0	41.6	10	25
Epoxy (Plastic)	1200	0.45	22.6	21.9	30.2	22.6	21.9	30.2	10

4.2.3 Code validation — load and boundary conditions

The boundary conditions are similar to the boundary conditions that were described in Section 4.1.3 and shown to the left in Figure 14. This means that the bottom plane is secured with rollers (fixed in y-direction) and one fixed point (fixed in both x- and y-directions). The side edges are free (not restrained in any direction), and the load is added as 0.14 mm displacement on the top plate (in negative y-direction). The total nodal reaction force output values were -1373 N in ABQ and -1.393 MN in RS2. This gives an average applied compression stress of 27 MPa in ABQ and 28 MPa in RS2.

Compared to the displacement load in the experimental design part of the study (0.10 mm), the load

was increased in this task. This was done to give more developed yielding in the elasto-perfect-plastic models.

4.2.4 Code validation — mesh

Triangular plane strain first order elements were used for this task. The mesh from the experimental design task was reused for the RS2 models. Creating identical meshes in RS2 and ABQ was however a too time-consuming objective. Even if the same amount of elements/discretizations were assigned to the boundaries, the mesh resolution/number of elements in the different areas did not match in models from the two programs. 20 segment discretizations per 10 mm flaw length — which was a good density for the RS2 models — resulted in a too fine mesh in ABQ, and some unwanted mesh irregularities close to the flaw occurred. 16 discretizations per 10 mm flaw length was instead used in the ABQ-models. This was conversely too coarse for the RS2-models and resulted in some unwanted effects close to the external model boundaries. Therefore — instead of attempting to design equal meshes in RS2 and ABQ — it was aimed to create a mesh that worked well in each program. The amount of elements on the long side of the flaw therefore differ in the RS2 and ABQ models (as described above). Yet, the same amount of elements were ascribed to the external boundaries in both programs (12 elements on short sides and 24 elements on long sides). 4 discretizations were further used on the curved fillets (quart circles) close to the flaw tip, and the short side of the flaw was given in one discretization in both programs.

Figure 16 compares the meshes around the flaw in ABQ and RS2 for models containing a grouted 30 mm long flaw with $\alpha = 60^\circ$. As can be seen in the figure, the mesh in the ABQ model has higher density, despite a lower number of elements being planted at the flaw boundary. Table 7 included the total amount of elements for each RS2 and ABQ model. Note that in ABQ, the mesh on the rock section of the grouted models did not always match the mesh in the rock section of the ungrouted counterpart, even if the same amount of "mesh seeds" (discretizations) were planted on the different line segments.

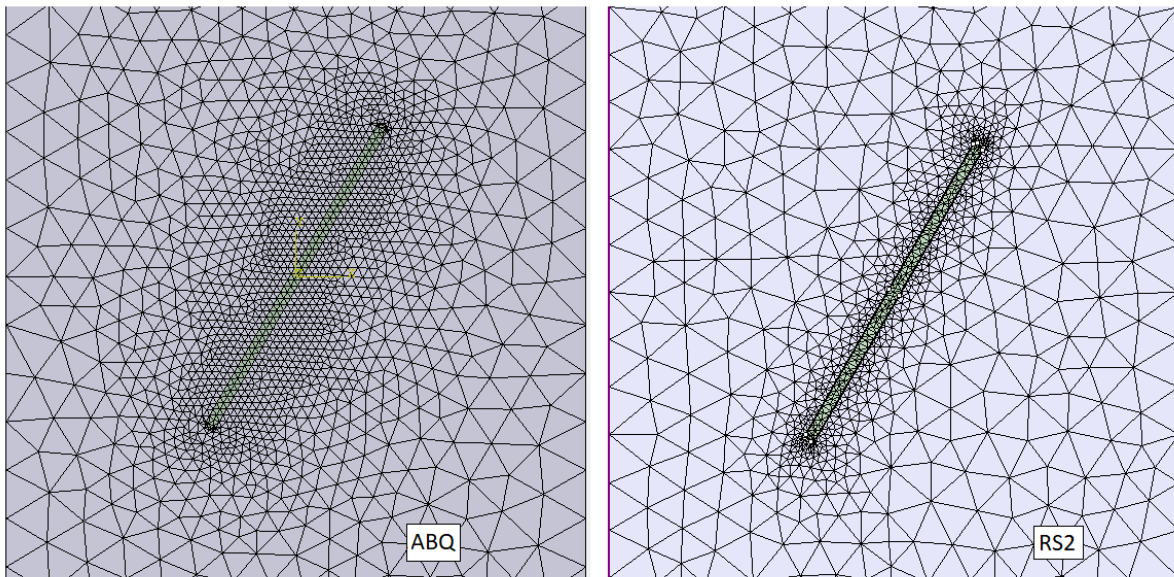


Figure 16: Comparison of the meshes used in ABQ (left) and RS2 (right) for a model containing a grouted 30 mm long flaw with $\alpha = 60^\circ$.

4.2.5 Code validation — other settings

The simulations were run in one stage in both programs. RS2 used the accelerated stiffness method, and ABQ used the Newton-Raphson method. A comprehensive stop criteria with a tolerance of 0.001 was used in RS2. In ABQ, an automatic stabilization based on a dissipated energy fraction of 0.0002 was applied. These values are the default tolerance values in the programs.

4.3 2D/3D validation

The motivation behind this task was to examine the agreement between uniaxial compression test results from two- and three-dimensional models. A part of this task was to explain the disagreements between the results. Therefore, several variations of models containing one grouted flaw geometry were made — instead of comparing several grouted and non-grouted flaw geometries. These tests were carried out in ABQ, and the following sections describe how these models were made.

4.3.1 2D/3D validation — geometry

In the first two-dimensional analyses in ABQ, the model containing a 1 mm thick grouted flaw with $2a = 20$ mm and $\alpha = 30^\circ$ geometry converged with a high displacement load magnitude compared to other models. This geometry was thus assumed to be one of the most numerically stable models, and was therefore chosen for this task.

Two- and three-dimensional models containing a grouted flaw with $2a = 20$ mm and $\alpha = 30^\circ$ were compared. The 50 mm wide and 100 mm tall two-dimensional geometries were created as described in Section 4.1.1.

The 3D geometrical model was created by extruding a 50 mm \times 100 mm rectangle in a depth of 50 mm. One of the 50 mm \times 100 mm planes was then partitioned with the flaw geometry $2a = 20$ mm, $\alpha = 30^\circ$ and $t = 1$ mm with fillets at the flaw tips (to exactly match the 2D models). By using the "Extrude/Sweep Edges" function in ABQ, the flaw geometry was extruded to cut through the 50 mm deep specimen (swept along the direction orthogonal to the flaw plane axes). The geometric model was finished by assigning epoxy material to the flaw partition and rock material to the remaining specimen volume. The 3D model geometry is presented in Figure 17.

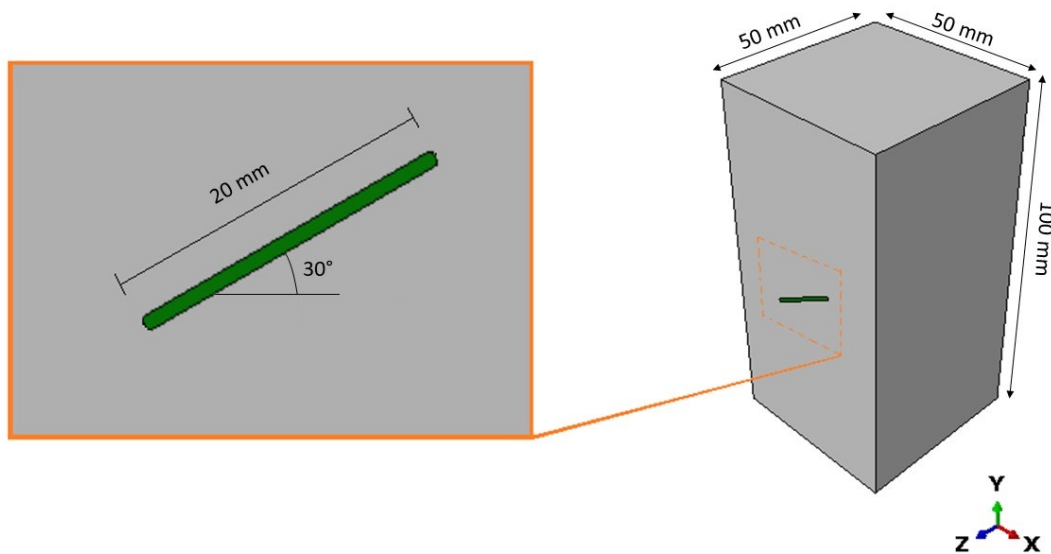


Figure 17: The geometry of the three-dimensional model containing a grouted flaw.

4.3.2 2D/3D validation — material properties

The material properties used in this task match the properties that were used in the code validation task. In this task, σ_t was increased to 6 MPa to enhance the model stability. Both linear-elastic and elasto-perfect-plastic material models were tested. Additionally, a few variations of the epoxy with improved

ν and E-modulus values (epoxy 2 and epoxy 3) were tested. See Table 9. The purpose of the material variations was to investigate some unexpected nonzero σ_z values along the flaw boundary in the outer x-y-plane, where σ_z was expected to be zero (see Section 5.3.4).

Table 9: Material properties 2D/3D validation.

Material	E-modulus (MPa)	ν	Peak σ_t (MPa)	Peak ϕ ($^\circ$)	Peak c (MPa)	Res. σ_t (MPa)	Res. ϕ ($^\circ$)	Res c (MPa)	ψ ($^\circ$)
Rock (Elastic)	19600	0.18	-	-	-	-	-	-	-
Epoxy (Elastic)	1200	0.45	-	-	-	-	-	-	-
Rock (Plastic)	19600	0.18	6.0	41.6	10	6.0	41.6	10	25
Epoxy1 (Plastic)	1200	0.45	22.6	21.9	30.2	22.6	21.9	30.2	10
Epoxy2 (Plastic)	1200	0.18	22.6	21.9	30.2	22.6	21.9	30.2	10
Epoxy3 (Plastic)	10000	0.18	22.6	21.9	30.2	22.6	21.9	30.2	10

4.3.3 2D/3D validation — load and boundary conditions

A top plate displacement of -0.10 mm was assigned to both the 2D- and 3D models. The 2D models are restrained with rollers and one fixed point on the bottom line and displacement on the top plate (as seen in Figure 14).

Figure 18 shows the defined boundary conditions of the 3D model. -0.10 mm displacement in y-direction is assigned to all top plate nodes. Further, all nodes in the bottom plane were restrained in y-direction. To prevent rigid-body-movement (rotation about the y-axis), additional constraints were assigned to parts of the bottom plate (Figure 18 b)). In the bottom plate, the nodes on the middle line parallel to z-direction were fixed in x-direction. Moreover, the nodes on the middle line parallel to x-direction were fixed in z-direction.

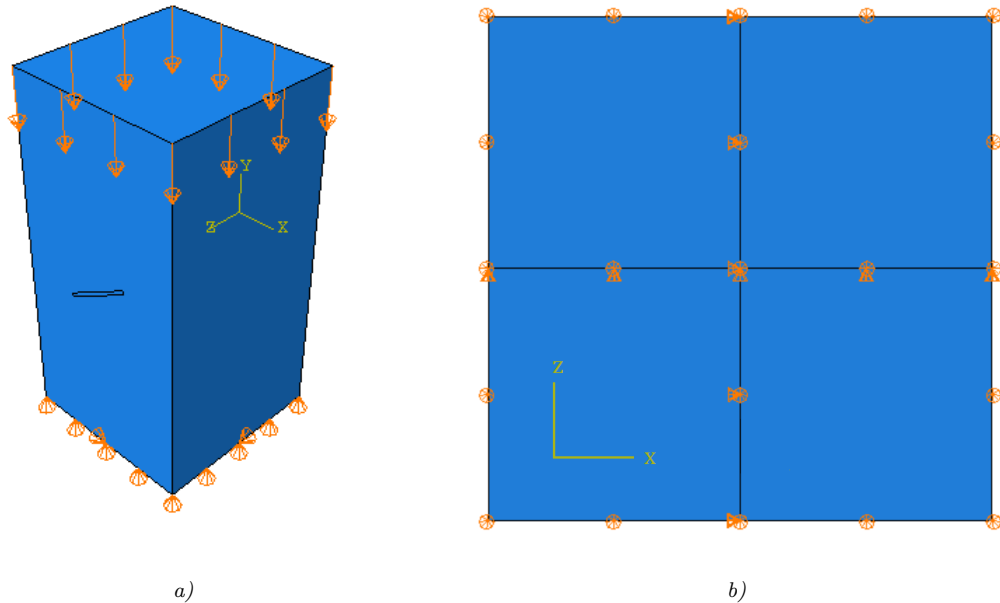


Figure 18: The boundary conditions of the 3D models. a) shows the entire model. b) shows the details in the bottom plate.

4.3.4 2D/3D validation — mesh

Designing the 3D model mesh appeared to be a more complicated task than the 2D mesh design. The first 3D model results included some non-zero σ_z buildups at the flaw boundary in the outer x-y-plane,

where zero σ_z was expected (see Section 5.3.4). There were additionally some disagreements between the stress contour plots from the 2D models and the 3D models. For the purpose of examining these errors further, it was decided to test several meshes. Different mesh densities and geometric orders were compared. These are presented in the following sections.

3D meshes

An h-refinement test was carried out to compare stress concentrations at points along the flaw (in the middle and outer plane). This test compared 5 meshes with increasing mesh density. These 5 meshes consisted of linear (6-noded) triangular prism elements from the 3D stress family in ABQ. Mesh 1 contained the lowest number of elements and mesh 5 contained the highest number of elements. Mesh 1 and 5 are shown in Figure 19. These simulations were run with elastoplastic material properties.

In the 3D analysis, it was also chosen to increase the geometric order of the elements. Second order (quadratic) element types calculate continuous stress values over the elements. Mesh 5 was therefore reused with quadratic (15-noded) triangular prism elements. These simulations did not converge with elastoplastic material properties, and were consequently run with linear-elastic material properties.

2D mesh

2D simulations were run with meshes that matched the meshes of the 3D models. This means that the mesh on the x-y-planes in the 3D model (which contain the flaw) is similar to the 2D model mesh. Examples of 2D and 3D meshes with similar resolution can be seen in Figure 36 in Chapter 5 (deformed mesh 2 and mesh 2 (2D) are compared). In the 2D-models, 3-noded (first order) triangle elements were used. The 2D models were tested with both plane stress and plane strain element types. This comparison was done with linear-elastic material properties, as the MC-criterion cannot be run with plane stress element family in ABQ. Two two-dimensional meshes were tested. The next section gives an overview of the different models that were used in this task.

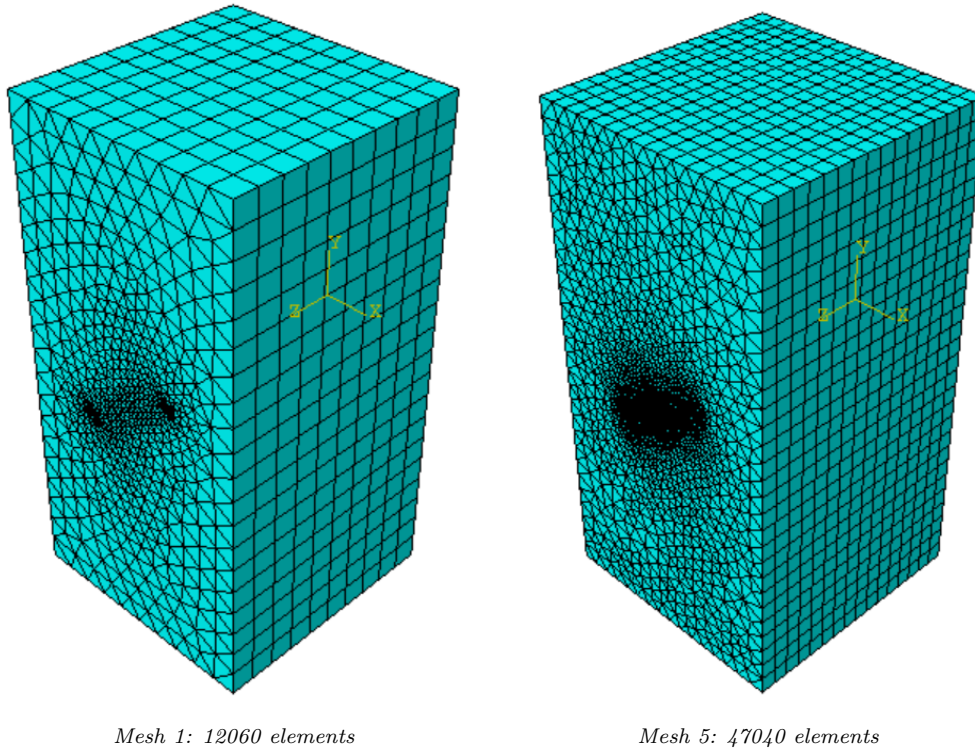


Figure 19: The coarsest mesh (mesh 1, left) and the finest mesh (mesh 5, right) that were used in the h-refinement test.

Overview of mesh and material combinations

An overview of the properties of the meshes — and which material and stress assumptions that were tested for each mesh — is given in Table 10. The table includes geometric order, total number of elements and total number of nodes.

Table 10: An overview of the details of the 2D and 3D meshes. Details of the tested material properties and stress assumptions are also given.

Mesh	Order	Elements	Nodes	Material behaviour	Element family
Mesh 1 (3D)	Linear	12060	6974	Plastic (epoxy 1,2 and 3)	3D Stress
Mesh 2 (3D)	Linear	14180	8140	Plastic (epoxy 1), elastic	"
Mesh 3 (3D)	Linear	17832	10088	Plastic (epoxy 1)	"
Mesh 4 (3D)	Linear	31836	17700	Plastic (epoxy 1)	"
Mesh 5 (3D)	Linear	47040	25755	Plastic (epoxy 1), elastic	"
Mesh 5q (3D)	Quadratic	47040	125713	Elastic	"
Mesh 1 (2D)	Linear	1206	634	Plastic (epoxy 1)	Plane strain
Mesh 2 (2D)	Linear	1390	726	Plastic (epoxy 1), elastic	Plane strain, plane stress

5 Results

This chapter presents results from the different simulation tasks. First, the experimental design results are presented. The second part outlines the code validation results, and the third part reports the 2D/3D validation results. Results are given as stress contour plots, maximal stress values, yielded element contour plots and/or yielded element percentages. General tendencies are explained and a few explanations are given. Results from the different simulation tasks are further discussed and compared in Chapter 6 and Chapter 7.

5.1 Experimental design

Models containing the 42 different flaw geometry combinations were tested with both linear-elastic and elastoplastic material properties. This section first presents the linear-elastic results, then it moves on to presenting the elastoplastic results. In Chapter 6, the results are compared to the experimental results from Le et al. (2018).

5.1.1 Experimental design — linear-elastic results

In linear-elastic simulations, the stress contour plots of the specimens were studied. The maximum σ_1 and minimum σ_3 values — and their locations — are summarized in Tables B1 and B2 in Appendix B. In all cases, the maximum value of σ_1 ,

$$\sigma_{1,max} > 0,$$

and the minimum value of σ_3 ,

$$\sigma_{3,min} < 0.$$

Thus, the maximal compressive stress, $\sigma_{c,max}$ was defined as:

$$\sigma_{c,max} = \sigma_{1,max}; \tag{14}$$

and the maximal tensile stress, $\sigma_{t,max}$ was defined as:

$$\sigma_{t,max} = |\sigma_{3,min}|. \tag{15}$$

The $\sigma_{c,max}$ and $\sigma_{t,max}$ for specimens containing ungrouted and grouted flaws were further plotted in the Figures 20 and 21. As seen in Figure 20, the $\sigma_{c,max}$ values were significantly lower in most of the grouted models compared to the ungrouted ones. For the 30 mm long flaw with dip angle 15° , the maximal concentrations were reduced by 172 MPa. Conversely, for the flaws with dip angle 90° , the stress concentrations were reduced by 1 – 3 MPa. The $\sigma_{c,max}$ values were found at the flaw tip for both ungrouted and grouted models (see Tables B1 and B2).

According to Figure 21, the maximum σ_t stress concentrations are not reduced after grouting in every case. For the 10 mm long flaws with $\alpha \geq 30^\circ$, the stress concentrations are 1-12 MPa higher in the grouted models. In other cases, *e.g.* flaws with $\alpha = 0^\circ$ the $\sigma_{t,max}$ is *ca.* 12 MPa lower in the grouted models. In the ungrouted models with $\alpha \leq 30^\circ$, high stress concentrations were found over a larger area, from the flaw tip to the midflaw. In their grouted counterparts, the high stress concentrations were only located at the flaw tip (or close to the flaw tip). The tensile stress values were therefore reduced in several locations around the flaw, even though the maximal concentrations were not reduced. Therefore, the maximum stress concentration values alone do not adequately describe the stress situations. A few typical contour plot examples from the linear-elastic models are thus presented in the following paragraphs and figures.

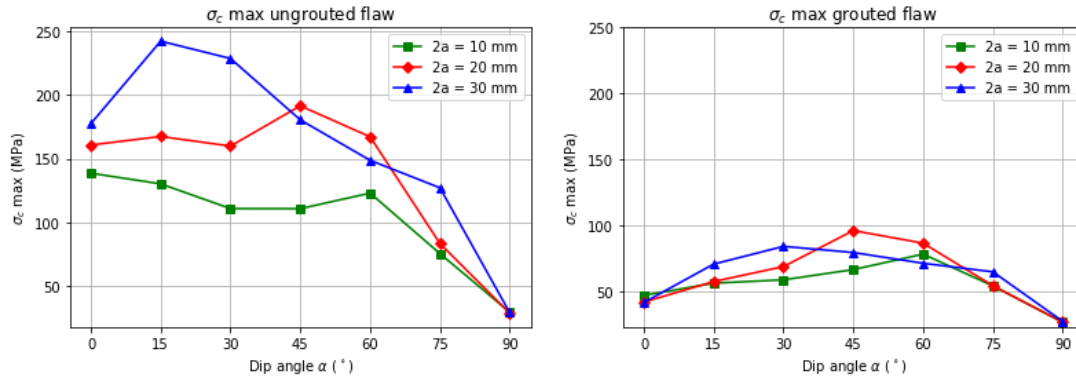


Figure 20: The maximum compressive stress values for the specimens containing ungrouted flaws (left) and grouted flaws (right).

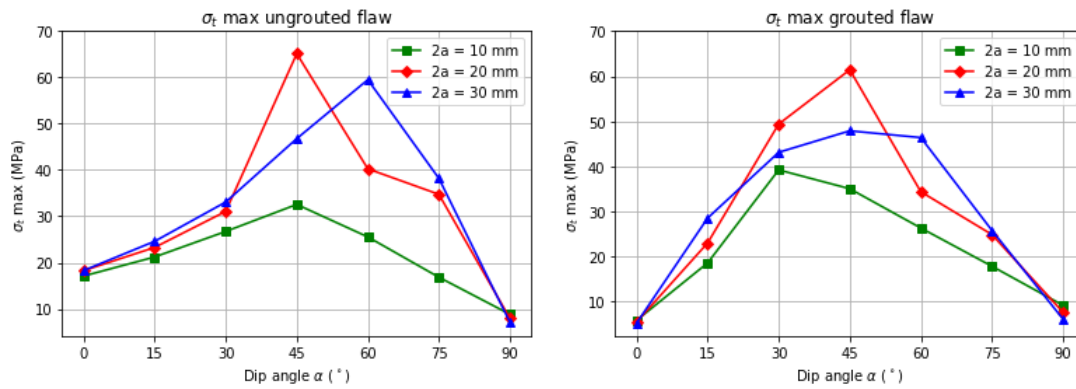


Figure 21: The maximum tensile stress values for the specimens containing ungrouted flaws (left) and grouted flaws (right).

Models containing 30 mm long flaws with $\alpha = 30^\circ$

Longer flaws with lower dip angles showed the most pronounced stress reduction due to grouting, according to Figure 20. This can also be seen from the contours plots. The results from the different models showed similar contour plot patterns. The models containing grouted and ungrouted 30 mm long flaws with $\alpha = 30^\circ$ are typical examples. Thus contour plots from these simulations are presented. Figures 22 and 23 show that σ_1 stress concentrations are reduced in the grouted models. The detailed stress field around the flaw tip is provided in Figure 23. The ungrouted flaw shows high σ_1 concentrations at the flaw tip (up to ≈ 230 MPa) and low σ_1 concentrations midflaw (≈ 0 MPa). In the grouted case, the flaw tip σ_1 concentrations are ≈ 84 MPa, while the values at the midflaw — and within the flaw — are around 16 MPa.

The σ_3 contour plots for the ungrouted and grouted specimens containing a 30 mm flaw with $\alpha = 30^\circ$ are given in Figures 24 and 25. The contour plots include only tensile stress contours ($\sigma_3 < 0$). In these models, the maximal tensile stress values were ≈ 10 MPa higher in the grouted models. However, as can be seen in the figures, the high tensile stress concentrations in the grouted model are located at the flaw tip at a smaller area compared to the ungrouted model. Figure 25 shows the detailed tensile stress field around the flaw. In the ungrouted model, the tensile stresses are generally higher around the entire flaw. Moreover, around the midflaw, and within the flaw, the grouted model results show compressive stress.

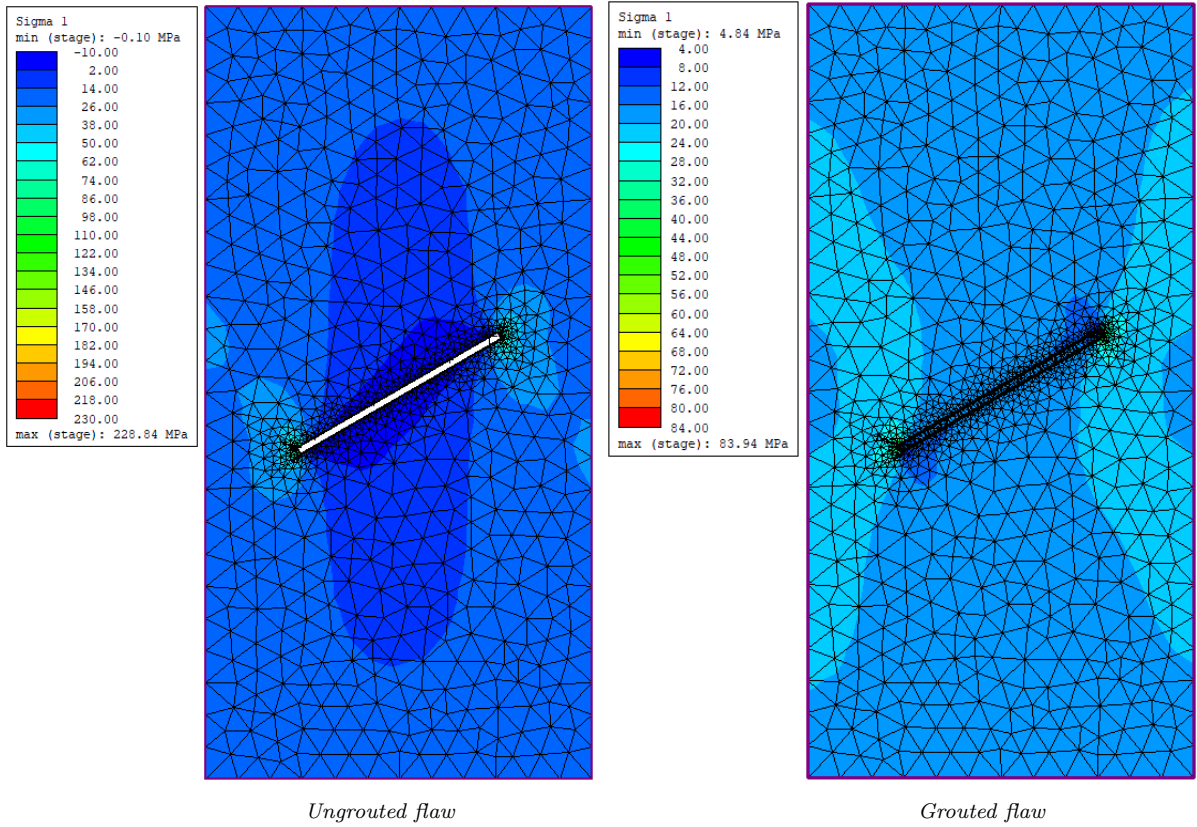


Figure 22: σ_1 contour plots for linear-elastic models containing ungrouped and grouted flaws, $2a = 30$ mm, $\alpha = 30^\circ$. The applied load was 20 MPa on the top plate.

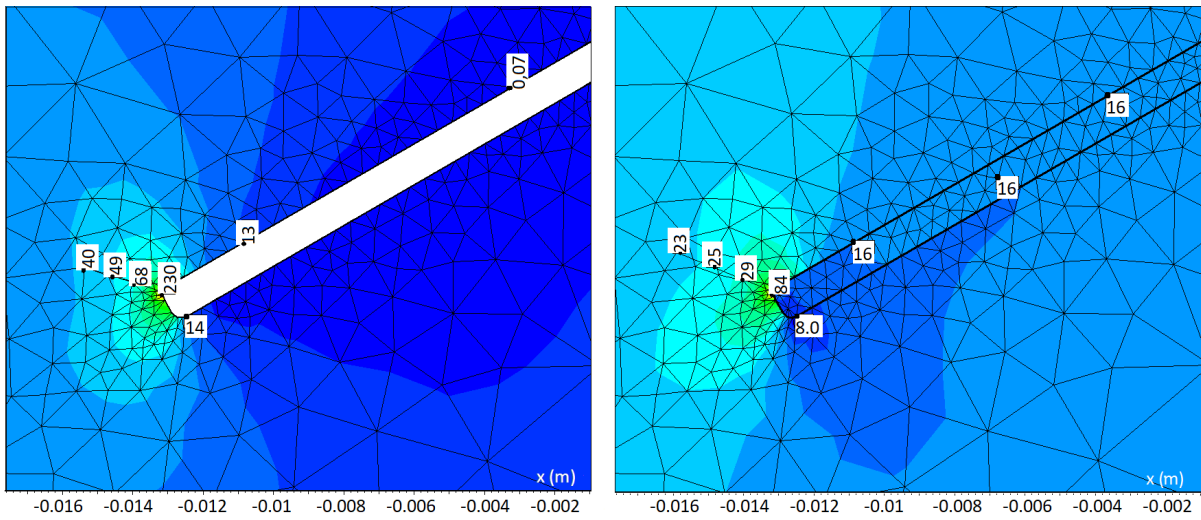


Figure 23: The detailed σ_1 contour plots around the flaw, for specimens containing ungrouped and grouted flaws, $2a = 30$ mm, $\alpha = 30^\circ$. Stress values are given in MPa, lower bar shows length scale. The applied load was 20 MPa on the top plate.

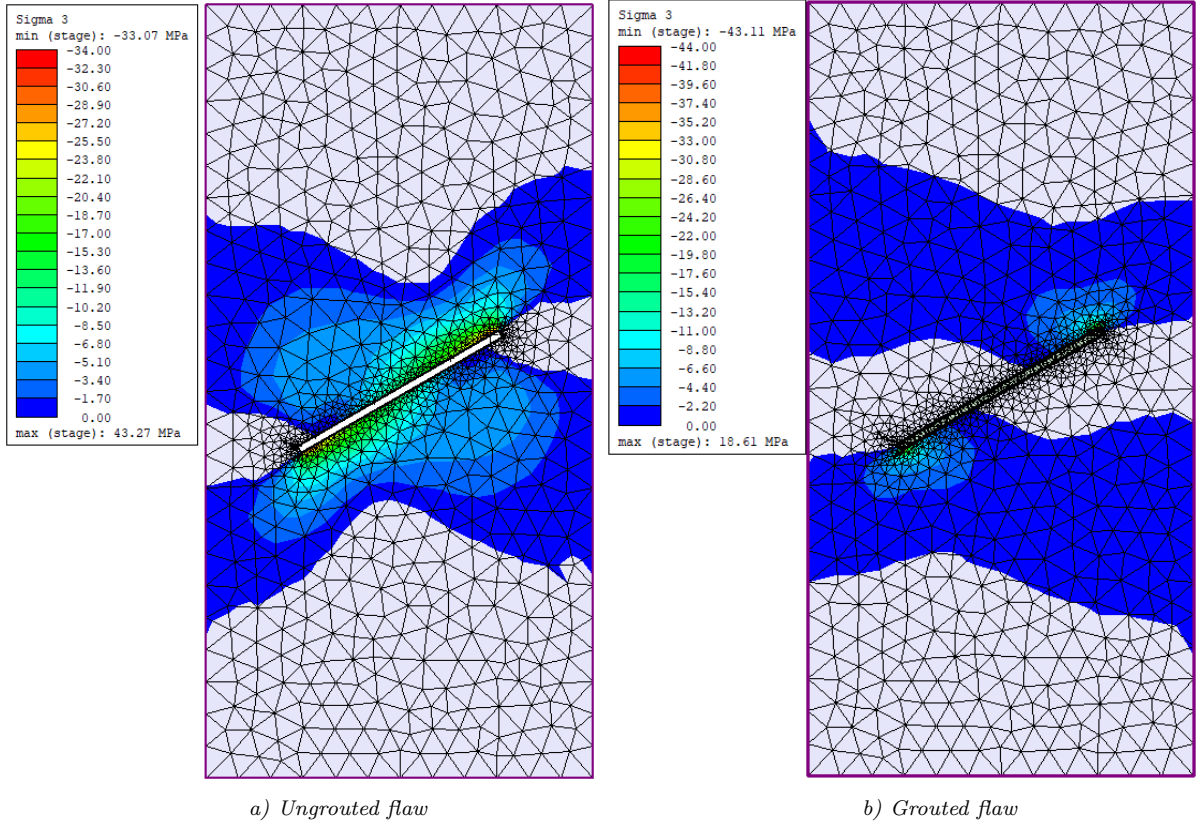


Figure 24: σ_3 contour plots for specimens containing ungrouted and grouted flaws, $2a = 30$ mm, $\alpha = 30^\circ$. The plots show tensile stress ($\sigma_3 < 0$), gray parts are in compressive stress. The applied load was 20 MPa on the top plate.

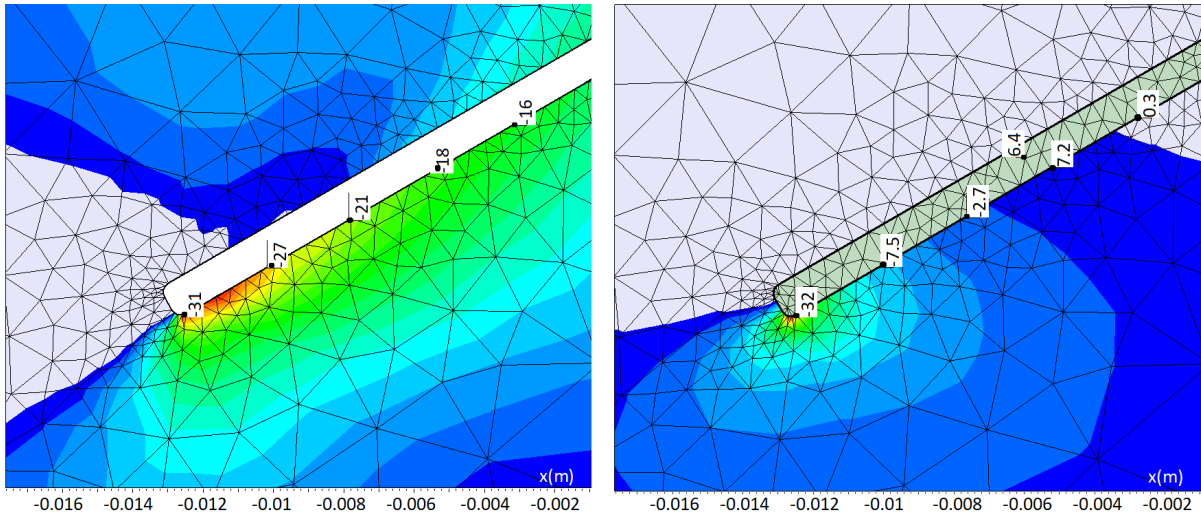


Figure 25: The detailed σ_3 contour plots around the flaw, for specimens containing ungrouted and grouted flaws, $2a = 30$ mm, $\alpha = 30^\circ$. The plots show tensile stress ($\sigma_3 < 0$), gray parts are in compressive stress. Stress values are given in MPa, lower bar shows length scale. The applied load was 20 MPa on the top plate.

Models containing 10 mm long flaws with $\alpha = 75^\circ$

According to the σ_c and σ_t maximal values presented in Figures 20 and 21, grouting does not affect the maximal stress concentrations for short flaws of high dip angles ($\alpha \geq 75^\circ$). Typical examples for short flaws with high dip angles are the models containing 10 mm long flaws with $\alpha = 75^\circ$. Contour plots from these models are therefore presented further. The σ_1 and σ_3 contour plots for the ungrouted and grouted models show similar patterns and stress values. As seen in Figure 26, the σ_1 concentrations at the flaw tips are about 20 MPa higher in the ungrouted model compared to the grouted model. At the midflaw, σ_1 is approximately 20 MPa in both cases. σ_1 is about 5 MPa within the grouted flaw. In Figure 27, the σ_3 contour plots for the models containing 10 mm long flaws with $\alpha = 75^\circ$ are shown. At nodes located a small distances away from the flaws, the σ_3 values differ with 0.0-0.7 MPa. Note that the maximum tensile stress/minimum σ_3 in these models were -17 MPa and -18 MPa for the ungrouted and grouted model respectively. These maximal values were concentrated at the flaw tip in both cases.

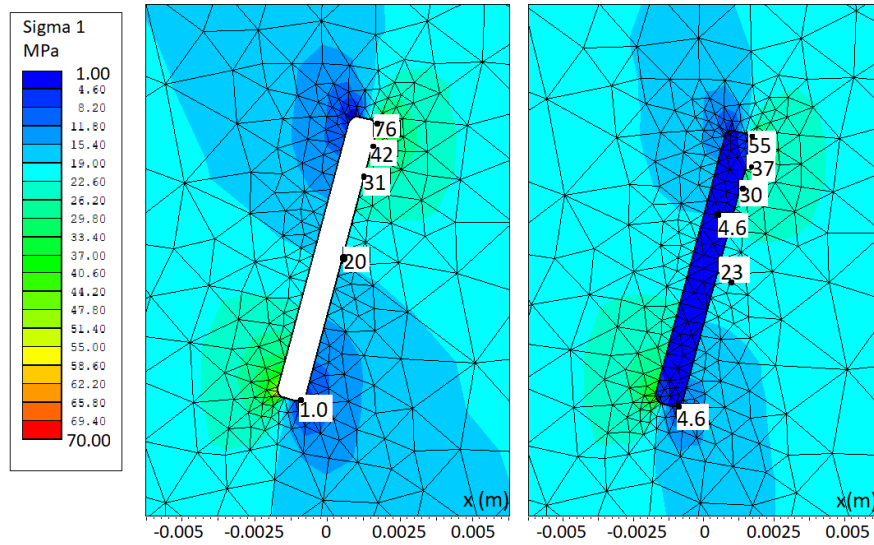


Figure 26: Contour plots showing the σ_1 contours around the flaw, for specimens containing ungrouted (left) and grouted flaws (right). $2a = 10$ mm, $\alpha = 75^\circ$. Stress values are given in MPa. The applied load was 20 MPa on the top plate.

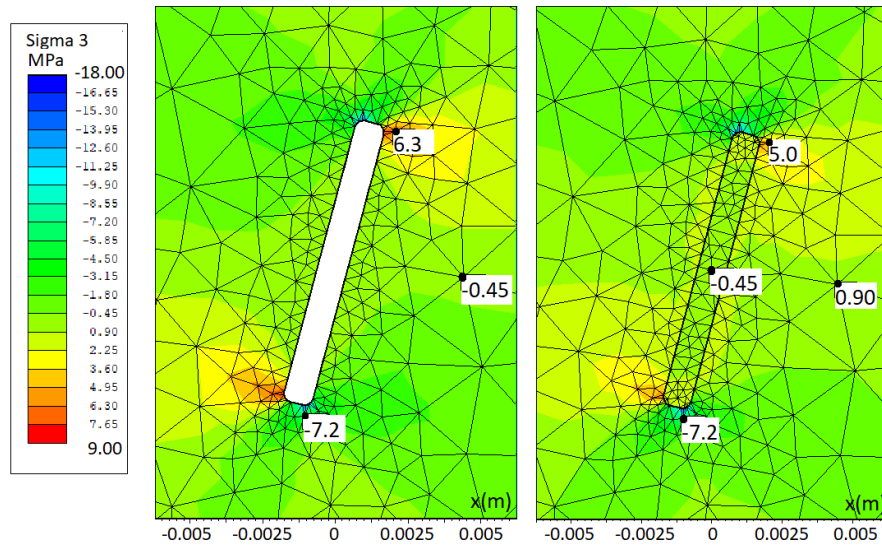


Figure 27: Contour plots showing the σ_3 contours around the flaw, for specimens containing ungrouted (left) and grouted flaws (right). $2a = 10$ mm, $\alpha = 75^\circ$. Stress values are given in MPa. The applied load was 20 MPa on the top plate.

5.1.2 Experimental design — elastoplastic results

The elastoplastic series of the experimental design task set out to investigate yielded elements around the flaw, and far field. The results from each elastoplastic simulation are given in Tables B3 and B4 in Appendix B. The tables include the total amount of yielded elements that were observed in each simulation and comment on the crack types (yielded elements pattern). This section summarizes the information in these tables and presents a few typical examples. Note that the results are discussed more thoroughly and compared to findings from literature in Chapter 6.

No yielded elements were observed within the grout material section/grouted flaw for the grouted models (the material has relatively high peak c). Moreover, the ungrouted flaw contain no elements. The following sections therefore focus on the yielding process in the rock material section.

Yielded elements

The ungrouted models registered from 0 to 995 more yielded elements than their grouted counterparts. Table 11 outlines the percentage of the elements in the rock material section that yielded in the ungrouted and grouted model simulations. In almost every case, the grouted specimens exhibited less yielding. The exception is the flaw geometry with $2a = 20$ mm and $\alpha = 90^\circ$, where both the ungrouted and grouted models showed 13 yielded elements.

For the longer flaws, the difference in yielding is more significant. When $\alpha = 0^\circ$, the yielded elements percentage is more than 50 percentage points lower for the grouted model than for the ungrouted model. For high angles ($\alpha = 90^\circ$) however, the difference between the ungrouted and grouted specimen is less than 1 percentage point. For all flaw lengths, the amount of yielded elements decreases when α increases. Conversely, for the grouted models, flaws with $\alpha = 30^\circ$ and $\alpha = 45^\circ$ demonstrate the highest percentage of yielded elements. This may occur because the grout has a higher Poisson's ratio than the rock ($\nu = 0.45$ compared to $\nu = 0.18$). Therefore, more stress can be induced in the flaw area for certain dip angles. To investigate this, an extra simulation was performed — where the Poisson number of the epoxy was reduced to 0.20 ($2a = 30$ mm, $\alpha = 30^\circ$). This resulted in a decrease in the yielded element percentage from 17% to 7% (see Table B5 in Appendix B).

Yielding patterns — crack types

Table 11 comments briefly on the observed crack type (yielding pattern). If they matched, the cracks were classified after the crack types that were described in Chapter 2. This means that — if the yield type (shear or tension) and propagation path matched the crack types presented in Table 3 — they were given crack names I-IX. Otherwise, a short comment about yield type and location was made. The following paragraphs and figures present the typical flaw types that were observed in the elastoplastic 2D models. Appendix C contains a detailed table presenting the yielded elements contour plots for each of the 42 elastoplastic models (see the legend in Figure 28). A few of the cases will be presented in more detail.

Figure 29 compares the yielding contour plots for models with ungrouted (NG) and grouted (G) flaws of length 20 mm and dip angle 45° . The legend is shown in Figure 28. The observed crack types in the ungrouted model were I, II and IV (about 25% of the elements yielded). Additionally, an early antitensile crack (III) can be seen in this ungrouted model. In the grouted model, type II and some elements yielded in shear at the flaw tip were found (about 10% of the elements yielded). A more detailed contour plot of these models is given in Figure 30. Crack types are marked. The following paragraphs present the tension cracks and shear cracks more systematically.

Tension failure

In the ungrouted and grouted models, elements yielded in tension were always observed at the flaw tip. Tension yielding that initiated at the flaw tip and propagated parallel to the loading direction (crack type II) were observed in every case, with three exceptions. In the three cases where II did not occur, the tensile yielding was not developed enough to decide the propagation direction. During the simulations, it was observed that the tensile crack types I-III could occur in both grouted and non-grouted models. Type II was however the most common crack type. Moreover, in the grouted models, type II was often

the only tension crack that occurred. This is because the grouted models developed less yielded elements than the ungrouted models under the same loading conditions. This can indicate that type II usually is the first crack to initiate. Figure 30 shows cases where type II occurred (the grouted specimen is a good example). Type I is also shown in this figure. An example of type III is shown in Figure 31 b).

Crack type VIII — a tensile crack that developed from the middle-section of grouted flaws, was not observed in the grouted models that were loaded with 20 MPa. However, crack VIII occurred as a secondary crack in the grouted model that was loaded with 28 MPa ($2a = 10$ mm, $\alpha = 0^\circ$). Moreover, a midflaw tensile crack appeared in the models with ungrouted 30 mm long flaws with dip angles 0° and 15° . In these models, 50-55% of the elements yielded. An example of the midflaw tensile crack is shown in Figure 31 a). The simulation of the model containing a horizontal 20 mm long ungrouted flaw with reduced load magnitudes (8 MPa) indicated that the midflaw crack was the first crack to initiate.

Shear failure

Shear yielding developed from the flaw tip in every ungrouted model with one exception (10 mm long flaw with dip angle 75°). In 12 of 21 of the grouted cases, shear yielding also initiated at the flaw tip. The propagation path of the shear "crack" did not always match the propagation path of crack type IV, which is parallel to the flaw plane. Further, the shear failure pattern that occurred in the grouted models were similar to the shear failure pattern in the ungrouted models, but less developed. This can be seen in Figure 30. In this case ($2a = 20$ mm, $\alpha = 45^\circ$) the propagation of the shear yielding was almost parallel to the flaw plane. In other cases — for example the ungrouted model containing a 30 mm long flaw with $\alpha = 0^\circ$ — the shear yielding pattern deviated about 45 - 60° from the horizontal line. This can be seen in Figure 31 a). This means that in the cases with pronounced shear yielding, the shear yielding followed a plane about 45 - 75° from the horizontal line. Some of these elements were yielded in both shear and tension. The shear yielding plane was parallel to the preexisting flaw plane in the cases where α was 45 , 60 and 75° and $2a$ was 20 and 30 mm (ungrouted flaws).

Basic continuum elements were used along the grout-rock interface in these simulations, *i.e.* infinite shear strength was assumed along the flaw.

Table 11: The percentage of yielded elements in models containing ungrouted and grouted flaws are compared for various flaw geometries. Comments are also made about the yielding pattern (crack type).

Flaw geometry		Ungouted flaws		Grouted flaws	
$2a$	$\alpha(^{\circ})$	Yielded rock %	Crack type	Yielded rock %	Crack type
10 mm	0	42.9	II, IV, midflaw tensile	2.60	II
	15	19.8	II, IV	4.22	II
	30	21.4	II, IV	6.20	II, shear at tip
	45	26.8	II, III, IV	13.3	I, II, shear at tip
	60	7.61	I, II, IV	5.67	II, shear at tip
	75	6.47	II, shear at tip	1.62	II
	90	1.59	II, shear at tip	1.21	II
20 mm	0	55.8	II, IV, midflaw tensile	1.77	II
	15	47.0	I, II, III, IV	4.98	II
	30	27.9	I, II, IV	8.96	II, shear at tip
	45	24.9	I, II, III, IV	10.6	II, shear at tip
	60	15.8	I, II, IV	6.64	II, shear at tip
	75	7.54	II, shear at tip	2.88	II, shear at tip
	90	0.72	tensile at tip	0.72	II
30 mm	0	54.5	II, IV, midflaw tensile	1.44	II close to tip
	15	50.6	II, III, IV, midflaw tensile	8.22	II, shear at tip
	30	40.8	I, II, III, IV	17.2	I, II, III, shear
	45	24.9	I, II, IV	11.5	I,II, shear at tip
	60	32.6	I, II, III, IV, midflaw tensile	8.36	II, shear at tip
	75	13.0	II, shear at tip	4.86	II, shear at tip
	90	0.80	tensile at tip	0.59	tensile at tip

Elastoplastic stress distribution

The stress distribution in the elastoplastic models was relatively complicated compared to the linear-elastic stress distribution. In a severely yielded case — an ungrouted flaw with $2a = 30$ mm and $\alpha = 30^\circ$ — the maximum σ_1 and minimum σ_3 concentrations were about 19 MPa and -1 MPa respectively. Moreover, the stress trajectories were rotated about the yielded areas. This can be seen in Figure 32, which shows the σ_1 contour plots for the model including stress trajectories. For the grouted counterpart (*i.e.* the grouted flaw with $2a = 30$ mm and $\alpha = 30^\circ$), the maximum σ_1 and minimum σ_3 concentrations were 40 MPa and -17 MPa respectively. The σ_1 contour plot for the grouted model is also included in Figure 32.

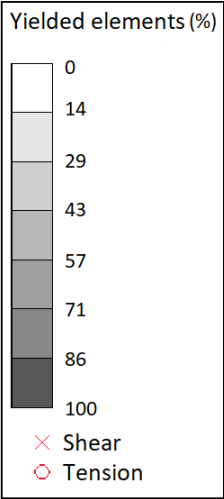


Figure 28: Legend for yielded elements contour plots.

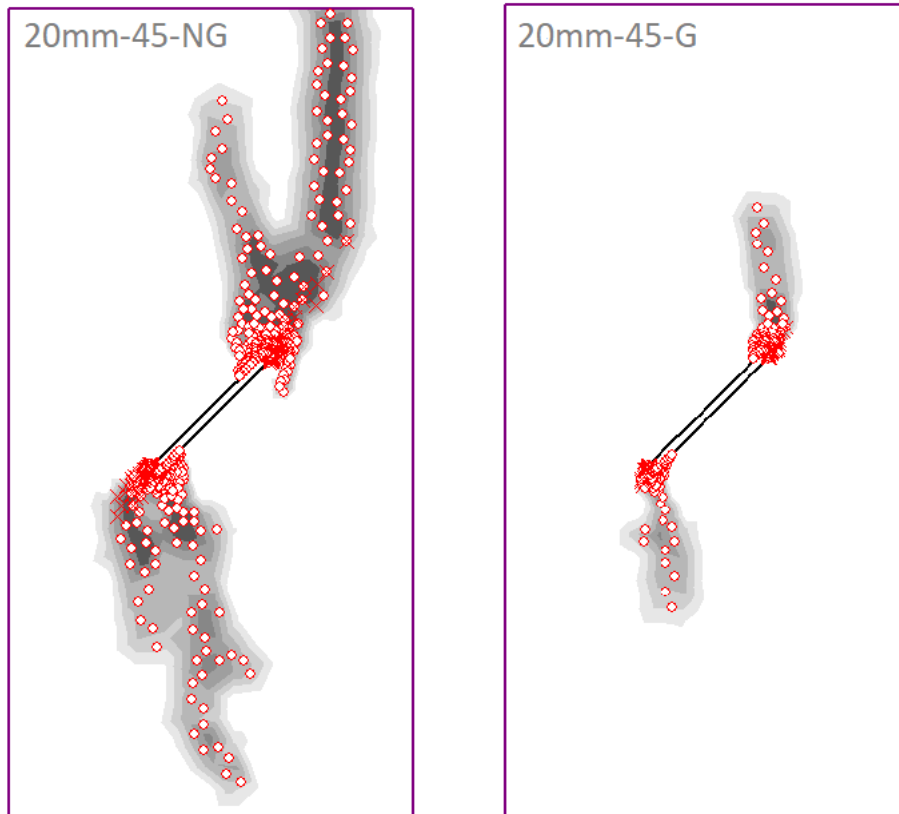


Figure 29: Contour plots of yielded elements around models containing ungrouted (left) and grouted (right) flaws with length 20 mm and dip angle 45° . Purple lines mark the external boundaries of the rock specimen. The applied load was 20 MPa on the top plate. Legend is given in Figure 28.

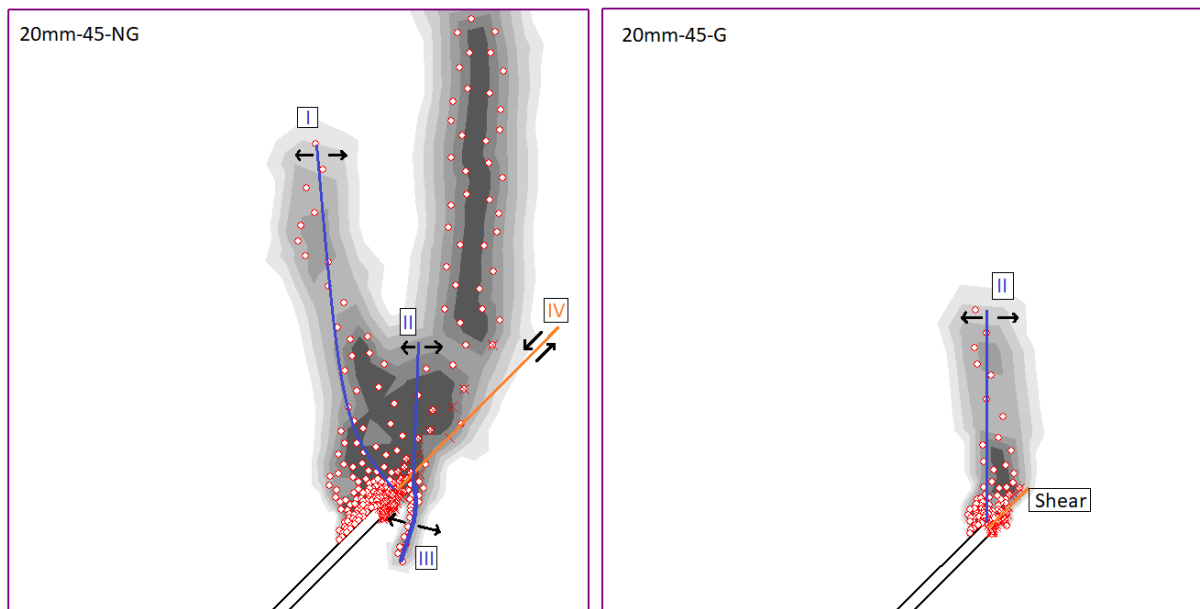


Figure 30: Detailed contour plots of yielded elements in models containing ungrouted (left) and grouted (right) flaws with length 20 mm and dip angle 45° . Ideal tensile crack types (blue lines) and shear crack types (orange lines) are drawn for comparison. The models continue past the stippled lines. Purple lines show the external boundaries. The applied load was 20 MPa on the top plate. Legend is given in Figure 28.

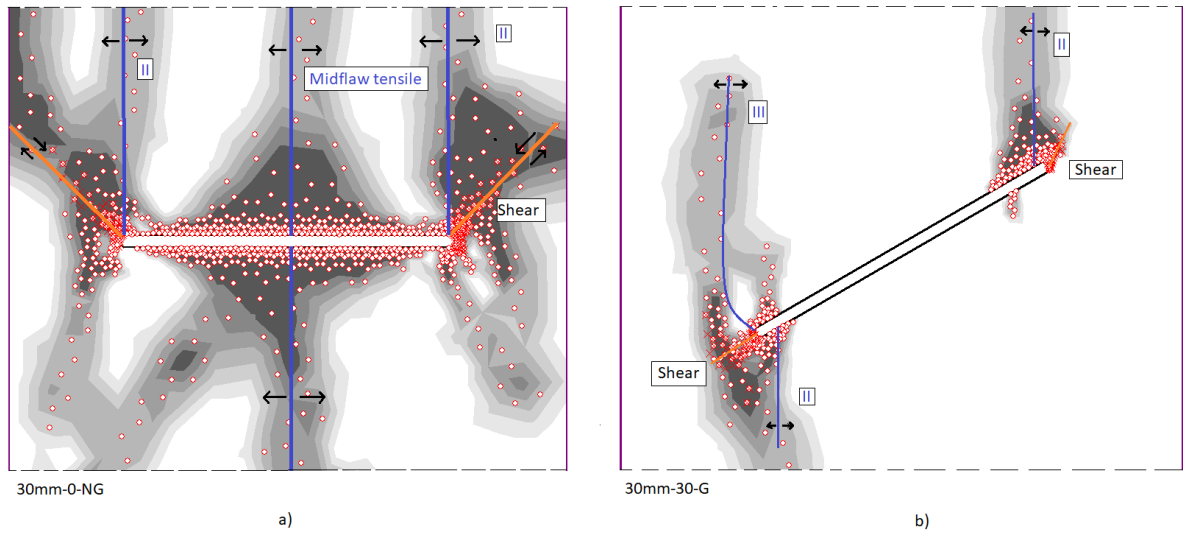


Figure 31: Left contour plot (a) shows a model containing an ungrouted flaw with $2a = 30$ mm and $\alpha = 0^\circ$. Right figure (b) shows a model containing a grouted flaw with $2a = 30$ mm and $\alpha = 30^\circ$. Ideal tensile crack types (blue lines) and shear crack types (orange lines) are drawn for comparison. The models continue past the stippled lines. Purple lines show the external boundaries. The applied load was 20 MPa on the top plate. Legend is given in figure 28.

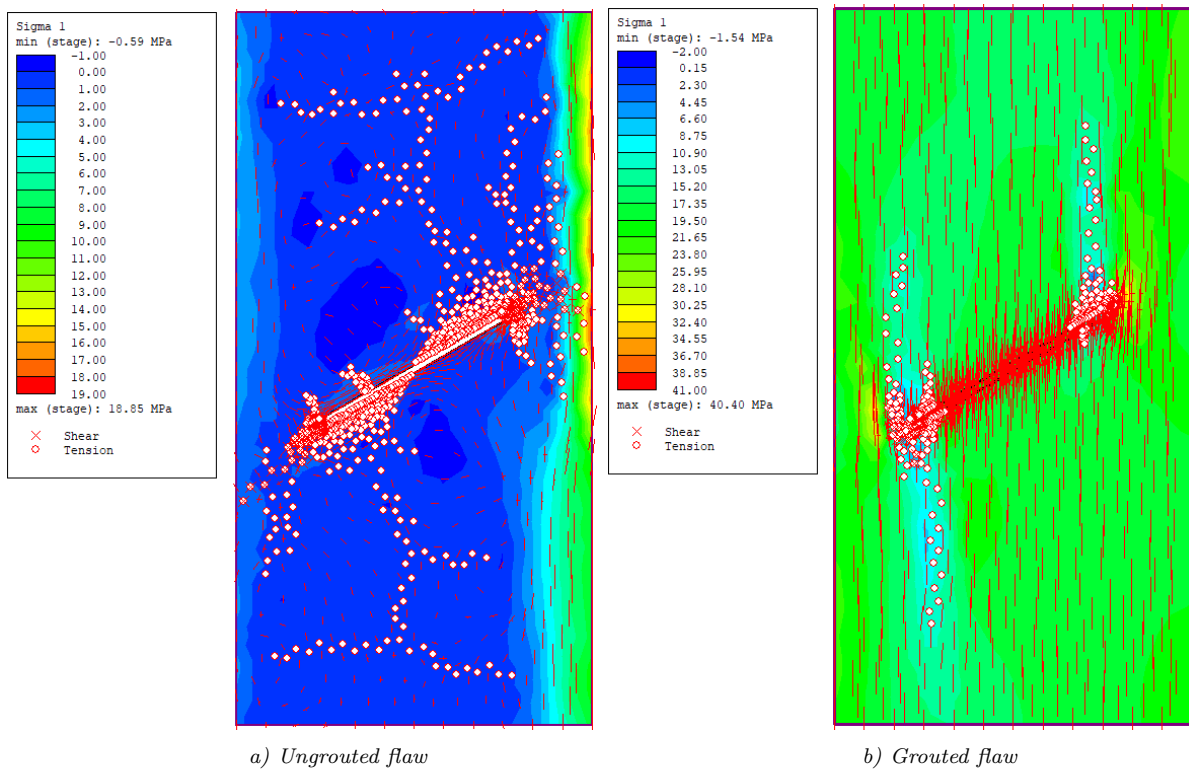


Figure 32: σ_1 for specimens containing ungrouted and grouted flaws with $2a = 30$ mm, $\alpha = 30^\circ$ including yielded elements and stress trajectories (red crosses/lines). In the ungrouted model, the applied stress is rotated about the yielded areas. In the grouted model, the applied stress is less rotated (σ_1 is vertical and parallel to the applied loading direction). The applied load was 20 MPa on the top plate.

5.2 Code validation

This section outlines the results from uniaxial compression tests of 19 models that were simulated in ABQ and RS2. In the simulations, both linear-elastic and elastoplastic material behaviour were assumed. The results from each series are presented and commented in the following subsections.

ABQ and RS2 use opposite stress sign conventions. In ABQ, tensile stress is defined with positive values, while tensile stress is defined as negative in RS2. This means that the σ_1 -plots in ABQ are actually σ_3 -plots — according to the convention used in RS2 (and in rock mechanics). This report consistently uses the rock mechanics convention, and the results from ABQ were therefore changed to match this system.

5.2.1 Code validation — linear-elastic results

Table 12 gives the $\sigma_{1,max}$ and $\sigma_{3,min}$ values that were registered in the ABQ and RS2 results. The intact models showed the best agreement. In both programs, the stress field of the intact models was uniform. Specifically, $\sigma_1 = 28.4$ MPa and $\sigma_3 = 0.00$ MPa over every element in the intact ABQ and RS2 models. For the models containing grouted and ungrouted flaws, the maximal σ_1 concentrations in ABQ deviated 0-30% from the concentrations in RS2. Further, the returned minimum σ_3 concentrations were 1-52% higher or lower in ABQ than in RS2.

The stress contour plots from the linear-elastic series showed similar patterns in both ABQ and RS2. In fact, the deviation between the programs was highest in local points around the flaw tip. An example of stress contour plots from the code validation task is given from the elastoplastic series in the next subsection.

Table 12: The $\sigma_{1,max}$ and $\sigma_{3,min}$ values from the linear-elastic simulations in ABQ and RS2 are given. The percentage error from the RS2 values is calculated for the stress values. For the specimens containing grouted flaws, the location of the elements that yielded in the elastoplastic series is indicated.

Geometry		ABQ-values			RS2-values			Error from RS2-values	
Flaw details	$\alpha(^{\circ})$	$\sigma_{1,max}$ (MPa)	$\sigma_{3,min}$ (MPa)	Yielding	$\sigma_{1,max}$ (MPa)	$\sigma_{3,min}$ (MPa)	Yielding	$\sigma_{1,max}$ error	$\sigma_{3,min}$ error
Intact specimen	N/A	28.4	0.00	No	28.4	0.00	No	0%	0%
Grouted flaw 2a=10 mm	0	63.7	-7.75	Midflaw (MF)	67.1	-8.23	MF	5%	6%
	30	99.7	-52.9	Flaw tip (FT)	82.0	-54.9	FT	22%	4%
	60	106	-46.1	FT	109	-36.9	FT	3%	25%
Grouted flaw 2a=20 mm	0	65.6	-7.01	close to FT	58.4	-7.64	close to FT	12%	8%
	30	109	-70.9	FT	96.1	-69.1	FT	13%	3%
	60	125	-64.6	FT	121	-48.1	FT	3%	34%
Grouted flaw 2a=30 mm	0	65.4	-7.01	close to FT	57.9	-7.28	close to FT	13%	4%
	30	118	-81.0	FT	118	-60.4	FT	0%	34%
	60	125	-70.6	FT	99.6	-64.9	FT	26%	9%
Ungouted flaw 2a=10 mm	0	174	-25.0	N/A	194	-23.9	N/A	10%	5%
	30	201	-42.2	N/A	155	-37.4	N/A	30%	13%
	60	132	-48.9	N/A	172	-35.8	N/A	23%	37%
Ungouted flaw 2a=20 mm	0	233	-26.1	N/A	225	-25.6	N/A	4%	2%
	30	274	-49.2	N/A	224	-43.5	N/A	22%	13%
	60	240	-86.0	N/A	234	-56.4	N/A	3%	52%
Ungouted flaw 2a=30 mm	0	273	-25.8	N/A	249	-25.6	N/A	10%	1%
	30	341	-56.1	N/A	330	-46.3	N/A	3%	21%
	60	264	-114	N/A	210	-84.0	N/A	26%	36%

5.2.2 Code validation — elastoplastic results

Elastoplastic simulations were only done for the grouted flaws. This is because the models containing ungrouted flaws did not converge in ABQ with the current material properties. The ungrouted models converged when the assigned tensile strength of the rock section increased from 6 MPa to 11 MPa. However, the purpose of this task was to compare the two programs, and the intact and grouted models

converged and provided a good basis for this comparison. Instead of studying models with an unrealistically high tensile strength, it was decided to focus on the models that converged. This subsection further presents the results from the intact and grouted elastoplastic models in ABQ and RS2.

The σ_1 contour plots from the elastoplastic ABQ and RS2 models containing a grouted flaw with $2a = 30$ mm and $\alpha = 60^\circ$ are given in Figure 33. The maximal σ_1 concentration at the flaw tip is about 20 MPa (22%) higher in ABQ, but the remaining values show a difference of 1-2 MPa between the programs (ca. 1% of $\sigma_{1,max}$). Overall, the agreement between the programs is good.

Table 12 indicates the yielding patterns that occurred in the grouted models in ABQ and RS2. No yielded elements were registered in the intact specimens. There is a good agreement between the yield development in ABQ and RS2. Typical examples of the yielding patterns are shown in Figure 34. This figure includes the yield contour plots of the models containing grouted 10 mm long flaws with dip angles 0, 30 and 60° . Subfigures a) and d) are examples of the midflaw yielding (from ABQ and RS2 respectively). Moreover, the flaw tip yielding pattern is seen in subfigures b) and c) from ABQ, and e) and f) from RS2. In both programs, the flaw tip yielding propagates about 60° from the horizontal line, and the extent of the yielded zone is about half a flaw length (5 mm) from the flaw tip.

As shown in the given examples, the agreement between ABQ and RS2 is good. The higher deviation is found at small and local points, and the yielding behaviour and stress contours are similar in every case where the simulations converged. The mesh is finer in the ABQ models, which is an explanation for the differences in stress concentration values.

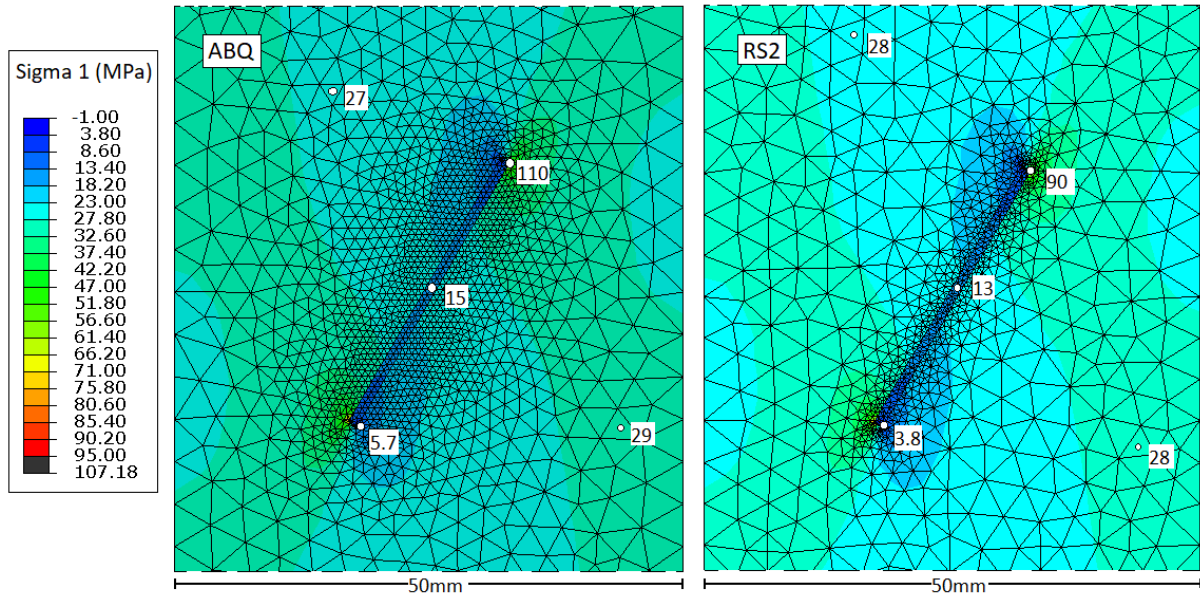


Figure 33: σ_1 contour plots for models containing a grouted flaw with $2a = 30$ mm and $\alpha = 60^\circ$. The left plot is from ABQ. The right plot is from RS2. The contour interval for both plots is $[-1.00, 95.00]$ MPa, as indicated in the legend. ABQ returned $\sigma_1 > 95.00$ MPa at some local flaw tip points.

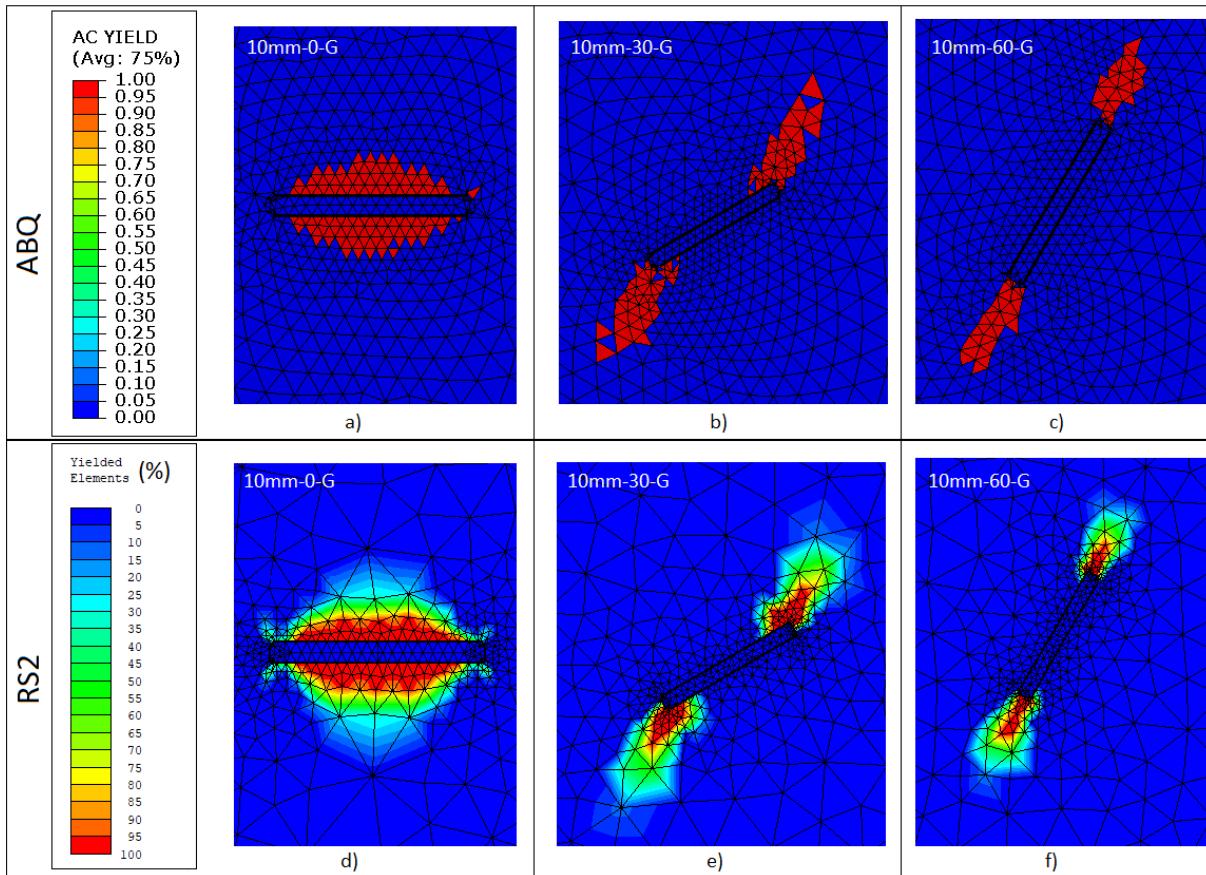


Figure 34: The yielded elements for models containing 10mm long grouted flaws with $\alpha = [0, 30, 60]^\circ$. The top row shows the ABQ results, and the bottom row gives the RS2 results.

5.3 2D/3D validation

2D and 3D uniaxial compression test simulations of models containing a 20 mm long grouted flaw with dip angle 30° were performed. This task tested both elastoplastic and linear-elastic material behaviours, and several mesh densities and element types. This section presents the results from these simulations.

5.3.1 2D/3D validation — elastoplastic stress results

The following paragraphs present stress values from the elastoplastic simulations. Stress values from several meshes are compared, and contour plot examples are given. The $\sigma_{1,max}$ and $\sigma_{3,min}$ values from each simulation are presented in Table 13. The convergence error was calculated as follows:

$$\text{convergence error} = \left| \frac{\text{result}(n) - \text{result}(n-1)}{\text{result}(n)} \right|. \quad (16)$$

As seen in Table 13, the $\sigma_{3,min}$ values are stable as the mesh density increases. $\sigma_{3,min}$ is located close to the flaw tip. Conversely, the $\sigma_{1,max}$ values appear to approach *ca.* 60 MPa at mesh 4, but increases to 70.8 MPa (12% increase) in the model with the finest mesh (mesh 5). This is because the mesh at the $\sigma_{1,max}$ location (at the curved/filleted part of the flaw tip) were actually slightly coarser at the curved part of the flaw tip in mesh 5 (and mesh 1) compared to mesh 2, 3 and 4. This adjustment was however necessary to make the mesh 5 simulation converge. On the other hand, the local mesh resolution around the $\sigma_{3,min}$ position, was finer in mesh 5 than mesh 1, 2, 3 and 4.

Table 13: Maximum and minimum stress concentrations for the elastoplastic 2D and 3D models from the mesh refinement test. The convergence error (conv. error) is included.

	# of elements	$\sigma_{1,max}$ (MPa)	σ_1 conv. error	$\sigma_{3,min}$ (MPa)	σ_3 conv. error
Mesh 1 (3D)	12060	81.4	unknown	-6.01	unknown
Mesh 2 (3D)	14180	63.1	29 %	-6.01	0.00 %
Mesh 3 (3D)	17832	63.3	0.32 %	-6.03	0.33 %
Mesh 4 (3D)	31836	62.1	1.9 %	-6.02	0.17 %
Mesh 5 (3D)	47040	70.8	12 %	-6.00	0.33 %
Mesh 1 (2D)	1206	77.7	unknown	-10.6	unknown
Mesh 2 (2D)	1390	67.1	16%	-9.97	6.3%

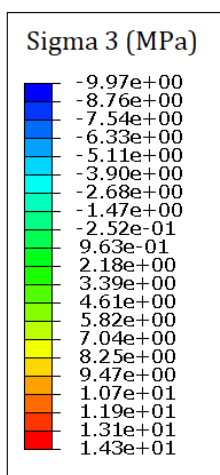


Figure 35: σ_3 legend for Figure 36.

The 2D and 3D models did not show exact agreement in maximal stress concentrations (as presented in Table 13). Models with approximately similar mesh resolutions (mesh 1 and 2) were compared in both 2D and 3D. The $\sigma_{1,max}$ concentration was 4 MPa (6%) higher and the $|\sigma_{3,min}|$ concentration was 4 MPa (76%) higher in the 2D model compared to the 3D model (for mesh 2).

Apart from the maximum stress magnitudes at the flaw tips, the contour plots showed overall good agreement in terms of stress values. However, some pronounced differences were observed around the midflaw area. Figure 36 compares the σ_3 -values for the plane strain 2D model and the 3D model (mesh 2). The figure includes the x-y-plane that cuts through the middle of the 3D model. The areas within the white marked lines are in tensile stress. As seen in the figure, tensile stress appears over a larger area — and closer to the midflaw — in the 3D model than in the 2D model. Close to the midflaw, the stress values over the rock material is about 2 MPa (in compression) in the 2D model. In the 3D model, the values were about -0.5 MPa close to the midflaw (rock). The agreement between the models is relatively poor around the midflaw, as the 2D model returns compressive stress and the 3D model returns tensile stress. However, the tensile stress magnitudes around the midflaw are low (close to 0 MPa) in the 3D model. The 2D and 3D models show similar stress values within the grouted flaw (7-8 MPa in both models). Additionally, both models agree on the position of the maximal tensile stress, which is close to the flaw tip.

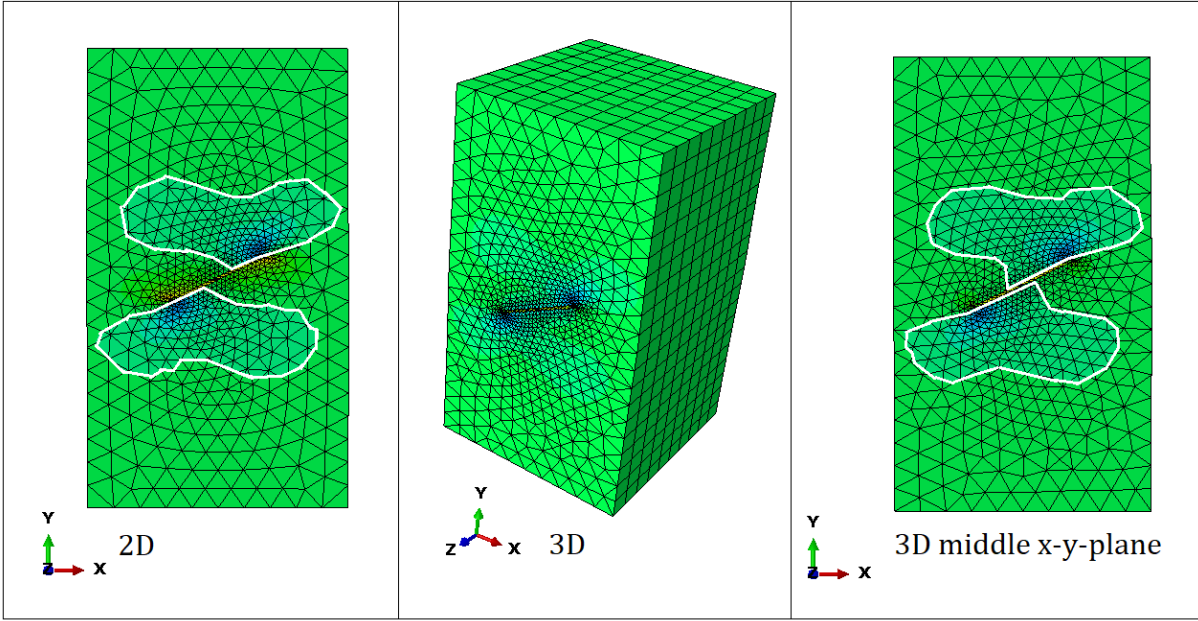


Figure 36: The σ_3 contour plots for elastoplastic 2D (plane strain) and 3D models with mesh 2. The white lines mark the boundary between tensile and compression stress. The figures show deformed meshes and contours, scaled by a factor of 100. The legend is given in Figure 35.

5.3.2 2D/3D validation — yielded elements

The results from the two- and three-dimensional elastoplastic models gave similar yielding patterns: yielding originating from the grouted flaw tip in the direction $60^\circ - 90^\circ$ from the horizontal line. Figure 37 shows the actively yielding element contour plots from the 2D and 3D models with mesh 2. The 2D model returns an AC yield contour plot with constant yield values over each element — either 0 or 1. In the 3D model, the AC yield contour plot is continuous.

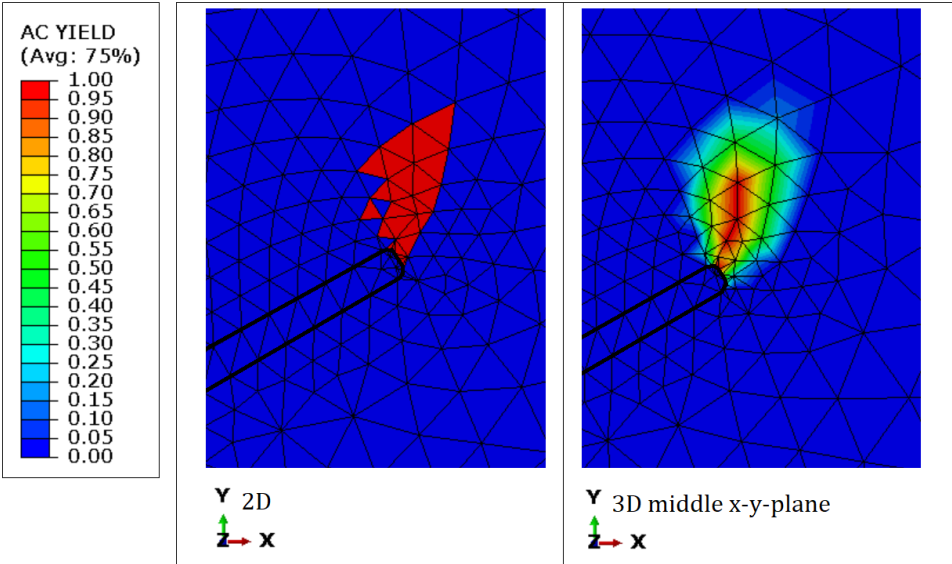


Figure 37: The AC yield contour plots around the tip of the 20 mm long grouted flaw with $\alpha = 30^\circ$. 2D and 3D models using mesh 2 are included. The figures show undeformed meshes and contours.

5.3.3 2D/3D validation — linear-elastic stress results

Simulations were carried out to compare linear-elastic material models from different element families. The 20 mm long grouted flaw with dip angle 30° was tested with plane strain and plane stress elements in 2D, and with the "3D stress" element type in 3D. Table 14 presents the maximum σ_1 and minimum σ_3 concentrations for these models, which used mesh 2. In every simulated case, the highest stress concentrations were located at the same local points close to the flaw tip. In terms of maximum compression and tensile stress values, the 3D model and the plane strain 2D models show the best agreement (there is a 8 MPa difference in $\sigma_{1,max}$ and 4 MPa difference in $\sigma_{3,min}$).

Figure 39 shows the σ_3 contour plot for the 2D and 3D simulations using mesh 2. The figures mark the tensile stress (negative stress values), which reads from the legend in Figure 38. As seen in the contour plots, the maximum tensile stress values are concentrated in small points close to the flaw tip. Apart from these concentrated areas, there is roughly good agreement between the stress values between the models. An obvious exception is the area around the midflaw, where the 3D model shows tensile stress and the plane strain model shows compression stress (similar for the elastoplastic models). Around the midflaw, the plane stress model contour plot is intermediate between the plane strain and 3D model. Additionally, the 3D model has some effects close to the vertical ($||\hat{y}$) specimen edges. These values are however close to 0 MPa.

Maximal stress concentrations for 3D models discretized with a finer mesh of first and second order elements (mesh 5 and 5q respectively) are also given in Table 16. The 3D model with mesh 5q returned a 63% higher σ_1 stress concentration than the 3D model with mesh 2. This is discussed further in Chapter 7.

Table 14: The maximum σ_1 and minimum σ_3 values from linear-elastic 3D and 2D models using mesh 2 with different element types.

	Element type	# of Elements	$\sigma_{1,max}$ (MPa)	$\sigma_{3,min}$ (MPa)
Mesh 2 (3D)	3D stress	14180	62.8	-40.3
Mesh 2 (2D)	2D plane strain	1390	70.7	-36.34
Mesh 2 (2D)	2D plane stress	1390	80.3	-24.1
Mesh 5 (3D)	3D stress	47040 (linear)	73.8	-29.9
Mesh 5q (3D)	3D stress	47040 (quadratic)	101	-60.0

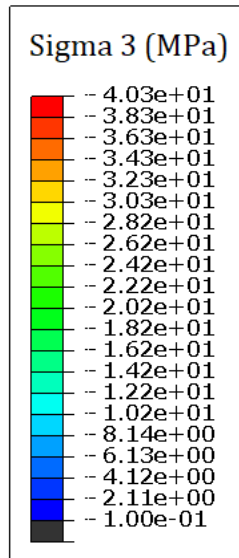


Figure 38: σ_3 legend for Figure 39.

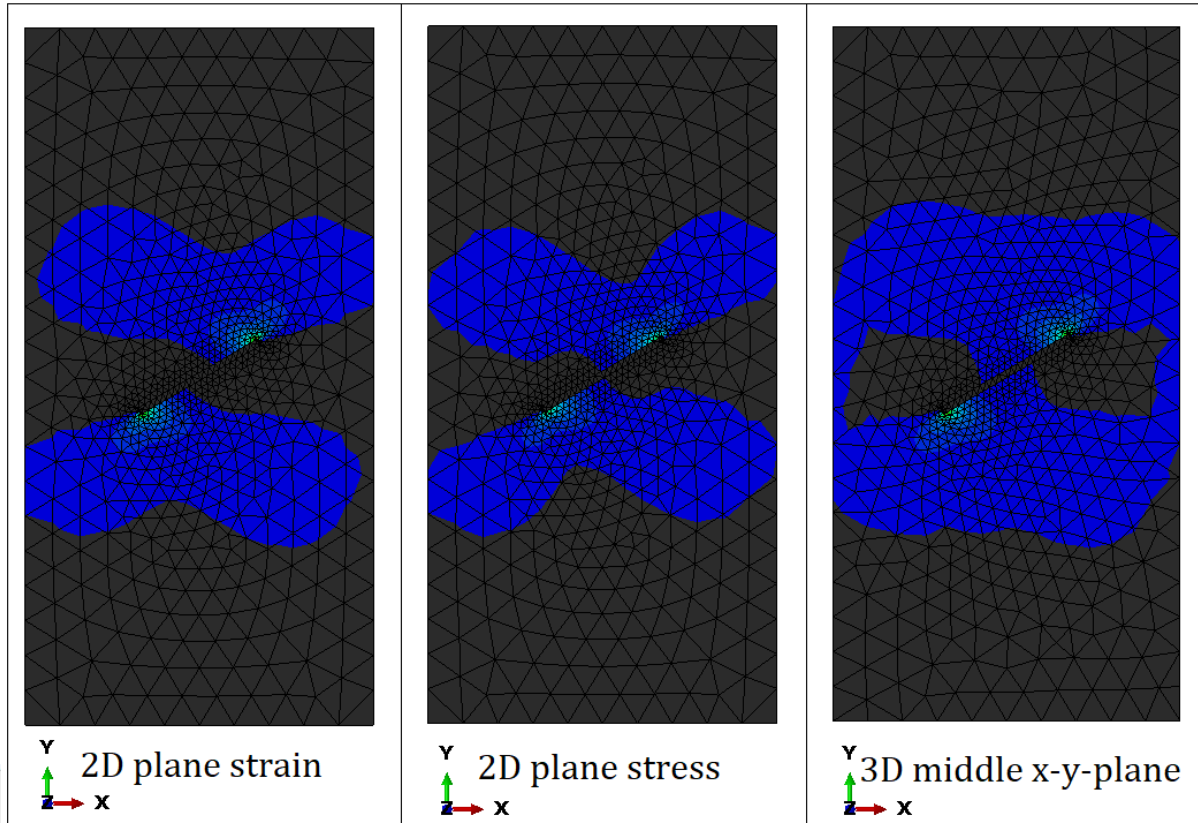


Figure 39: The σ_3 tensile stress contour plots for linear-elastic 2D plane strain, 2D plane stress and 3D models (mesh 2). The figures show undeformed meshes and contours. The legend is given in Figure 38.

5.3.4 2D/3D validation — nonzero σ_z buildups in the outer x-y-plane of 3D models

The 3D model contour plots showed some unexpected stress concentrations on the outer x-y-plane. An example is shown in Figure 41. σ_z concentrations of around 3 MPa were registered around the flaw. The far-field σ_z values were *ca.* 0 MPa. However, because the x-y-plane is not restrained or loaded in z-direction, the σ_z values are expected to be (approximately) 0 MPa over the entire outer x-y-plane. To examine these effects, the σ_z values from three locations A, B and C — see Figure 40 — were registered during the h-mesh-refinement test for the elastoplastic models. The values were obtained from both the outer x-y-plane and the x-y-plane that cuts through the middle of the specimen. Values were obtained from both the elastoplastic models (see Table 15) and linear-elastic models (see Table 16).

The h-refinement tests on the elastoplastic models that are presented in Table 15 set out to investigate whether the σ_z flaw concentrations on the outer x-y-plane were averaging-effects. However, as the mesh density increased, the σ_z values remained between -2 to -3 MPa. The tensile stress values on the locations decrease with 0.84 MPa (point A) to 3.2 MPa (point C) from the outer plane to the middle plane. Moreover, the σ_z values around the midflaw (point C) were approximately the same values as the σ_3 values at the midflaw. The mesh refinement test did not reduce the unwanted nonzero σ_z buildups.

Mesh 5 (3D) was additionally tested with quadratic shape functions (mesh 5q). This test was done with linear-elastic material assumptions due to convergence problems. Table 16 compares stress values at the points A, B and C from linear-elastic models discretized with first order elements (mesh 5) and second order elements (mesh 5q). The values on the middle x-y-plane are relatively stable as the element order

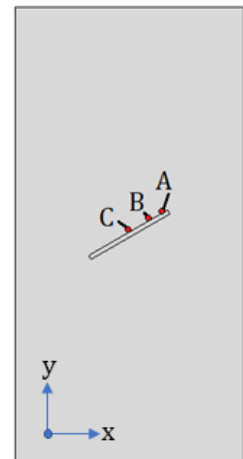


Figure 40: Locations A, B and C (x-y-plane).

increases. On the outer plane, the stress values in point B and C increased by about 2 MPa. However, the σ_z values in the outer plane were concentrated over a smaller area close to the material boundary (flaw) in the mesh 5q simulation. This can be seen in Figure 41. The σ_z buildups appear more concentrated around the flaw with the quadratic mesh 5q.

Material tests were carried out to investigate the σ_z effects around the material boundary of the 20 mm long grouted flaw with $\alpha = 30^\circ$. The test assumed elastoplastic material behaviour and compared the σ_z stress values around the flaw for different grouts. Models grouted with epoxy1 ($\nu = 0.45$, $E = 1.2$ GPa), epoxy2 ($\nu = 0.18$, $E = 1.2$ GPa) and epoxy3 ($\nu = 0.18$, $E = 10$ GPa) were compared. As the Poisson's ratio value decreased (epoxy2 simulation), the σ_z tensile values around the flaw in the outer x-y-plane decreased by almost 2 MPa. Conversely, the midplane values increased by 0.9 and 0.5 MPa at location B and C respectively. In the epoxy3 model, both ν and E were improved. These results showed σ_z concentrations < 1 MPa in the positions A, B and C. In the middle plane, the midflaw tensile stress values were low (around -0.1 MPa). Overall, these results suggest that higher contrasts in the stiffness and lateral expansion between the rock and the epoxy at the material boundary induce the local σ_z stress concentration effects close to the flaw boundary.

Table 15: σ_z values in three points along the flaw, obtained from the outer and middle x-y-planes of the *elasto-plastic* models. Figure 17 locates the points A, B and C.

			Outer x-y-plane Sigma ZZ (MPa)			Middle x-y-plane Sigma ZZ (MPa)		
	# of Elements	Material	A	B	C	A	B	C
Mesh 1 (3D)	12060	Epoxy1	-2.98	-2.58	-2.61	-1.88	-0.733	-0.398
Mesh 2 (3D)	14180	Epoxy1	-3.11	-2.70	-2.70	-2.11	-0.902	-0.404
Mesh 3 (3D)	17832	Epoxy1	-3.09	-3.04	-3.09	-2.11	-0.770	-0.406
Mesh 4 (3D)	31836	Epoxy1	-3.05	-3.55	-3.57	-1.82	-0.906	-0.417
Mesh 5 (3D)	47040	Epoxy1	-2.16	-3.34	-3.33	-1.32	-0.997	-0.402
Mesh 1 (3D)	12060	Epoxy2	-1.07	-1.22	-0.675	-1.57	-1.63	-0.917
Mesh 1 (3D)	12060	Epoxy3	-0.650	-0.340	-0.319	-0.555	-0.131	-0.0815

Table 16: σ_z values at locations A,B and C from the *linear-elastic* 3D simulations (see Figure 17) along the flaw for meshes using first order and second order elements. σ_1 and σ_3 maximum and minimum values are also included.

			Outer x-y-plane Sigma ZZ (MPa)			Middle x-y-plane Sigma ZZ (MPa)		
	# of elements	# of nodes	A	B	C	A	B	C
Mesh 5 (3D)	47040	25755	-6.35	-3.73	-3.58	-6.57	-1.73	-0.492
Mesh 5q (3D)	47040	125713	-6.19	-5.87	-5.70	-6.57	-1.73	-0.491

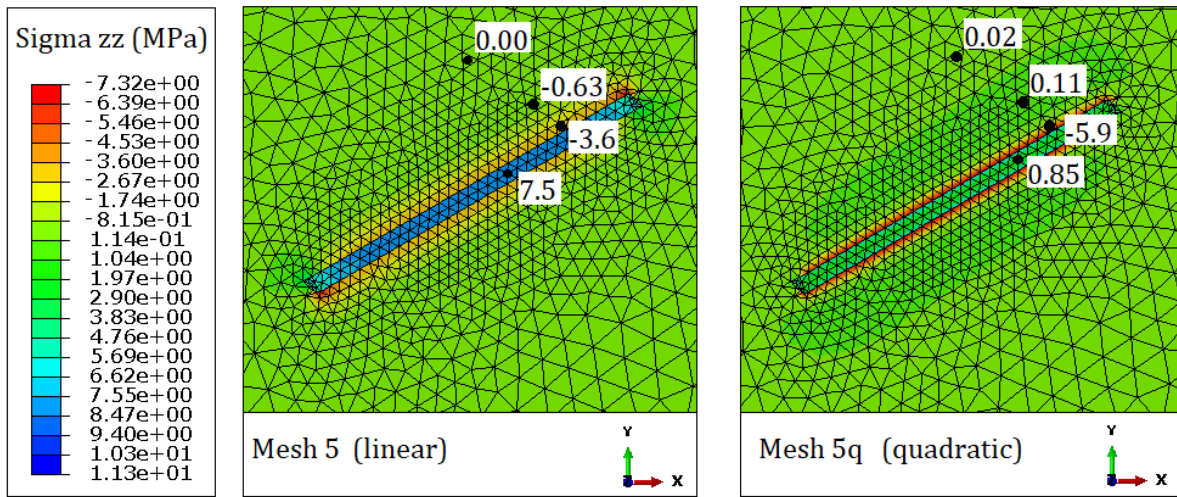


Figure 41: The σ_z contour plot for the outer x - y -plane of 3D models discretized with mesh 5. Left contour plot uses first order shape functions, right contour plot uses second order shape functions.

6 Comparison of Numerical Results and Experimental Results

The current study simulated uniaxial compression tests of rocks containing a single grouted or ungrouted flaw. The first objective of this study was to compare observed yielding patterns from the numerical modelling with the experimental results from Le et al. (2018). Simulations of Mohr-Coulomb materials were done with perfect brittle behaviour or perfect plastic behaviour. Both the perfect plastic and perfect brittle models agree on the locations of the yield initiation points, which were at the flaw tip or midflaw. However, the perfect brittle models returned yielded elements plots that resemble cracks most closely (long, thin yield patterns that grow more in length than width). Conversely, the perfect plastic yield contour plots appeared more as crushed zones around the flaw (the yield patterns tended to be shorter and thicker). It follows that the perfect brittle models are more realistic when modelling fracture failure of rock specimens. This chapter therefore compares the yield contour plot results from the brittle models (experimental design task) to the cracking behaviour observed in lab experiments by Le et al. (2018). Moreover, the chapter discusses the strengthening effects after grouting in terms of stress distribution and yielding patterns. Errors and limitations by the numerical models are addressed in Chapter 7.

6.1 UngROUTED rocks

Table 17 gives the crack types that were observed in the ungrouted lab tests by Le et al. (2018), and the crack types from the ungrouted numerical models. The following sections compare the cracking behaviour of the numerical and experimental models.

Table 17: Crack types observed in numerical simulations and the lab results (from Le et al. (2018)) for rocks containing ungrouted flaws of different length and dip angle combinations.

Flaw geometry		Observed crack types (ungrouted flaws)	
$2a$	α ($^{\circ}$)	Numerical results	Experimental lab results
10 mm	0	II, IV, midflaw tensile	II
	15	II, IV	II, III, (VI)
	30	II, IV	II, (VI)
	45	II, III, IV	III, (VI)
	60	I, II, IV	II, IV, (VI)
	75	II, shear at tip	II
	90	II, shear at tip	I, (VI, VII)
20 mm	0	II, IV, midflaw tensile	II, (VI)
	15	I, II, III, IV	II, III, (VI)
	30	I, II, IV	I, II, (V)
	45	I, II, III, IV	III, (V, VI)
	60	I, II, IV	I, III, IV, (VI)
	75	II, shear at tip	III, (VI)
	90	tensile at tip	I, (V, VII)
30 mm	0	II, IV, midflaw tensile	II, (VI)
	15	II, III, IV, midflaw tensile	II, (VI)
	30	I, II, III, IV	II
	45	I, II, IV	III, IV, (VI)
	60	I, II, III, IV, midflaw tensile	II, IV, (VI)
	75	II, shear at tip	II, IV, (V, VI)
	90	tensile at tip	II, (V, VII)

6.1.1 Far-field and spalling crack types not observed in numerical models

The crack types V, VI and VII occurred randomly in the lab experiments, meaning there was no clear relation between the crack geometry and these crack types. In the numerical results, crack types V-VII did not occur. Crack type V is a far-field tensile crack and initiates from microcracks and micropores in the rock material. However, the numerical model contains no microstructures that can act as stress

concentrators. Thus, cracks cannot initiate at far-field locations in the numerical models, and it follows that crack type V can't be expected in the numerical models. Furthermore, the crack types VI and VII are spalling cracks. Cracks VI and VII accompany tensile cracks or initiate at the specimen corners and edges. Spalling may result from friction in the contact between the loading plates and the specimen. The load was further applied directly as a displacement defined on the nodes on the upper specimen boundary. Moreover, the numerical models are designed with perfectly straight lines connected at accurate 90° corners. This loading method did not induce any stress concentrations (or yielding) on the corners or edges of the modelled specimens. This explains the absence of cracks V-VII in the numerical models. Thus, crack types V, VI and VII were not expected to develop in the grouted nor ungrouted numerical simulations that were carried out in this project. The crack types V-VII are therefore written in parentheses in the tables.

In every experimental case, spalling and far-field tensile cracks were observed. This implies that crack types V-VII were a part of the failure development and degenerated the strengths of the specimens. In reality, intact rocks containing no flaws fail by coalescence of microcracks, that eventually make up a persistent failure plane. In the numerical models containing no flaw, there are no stress concentrators. This was demonstrated by loading intact models (without flaws) beyond failure. The intact models returned an uniform stress field (every element showed equal stress values), and all elements therefore yielded at the same time. This means that the numerical model contains only one stress concentrator — the flaw. Conversely, the lab specimens contain several microscopic stress concentrators in addition to the flaw. Due to the lack of microscopic stress concentrators in the numerical models, it could be expected that more cracks originate from positions around the flaw in the numerical models compared to the lab specimens. This is further addressed in the following sections. Additional explanations for discrepancies between the numerical and experimental results are also offered.

6.1.2 Flaw tip tensile cracks

Crack type II was the primary crack in most of the lab test cases. The exceptions were for example specimens containing ungrouted flaws with dip angle of 45° . As seen in Table 17, type II occurred in almost every simulated model with ungrouted flaws. However, in the numerical ungrouted flaw results, type II was always accompanied by other tensile cracks (I or III) or shear crack (IV). This means that for matching flaw geometries, more crack types were observed in the numerical results than the experimental results, for the following possible explanation. In the numerical simulations, every brittle model was assigned an average load of 20 MPa on the top plate. This loading magnitude exceeds the experimental UCS of the 30 mm long flaws with dip angles 0, 15, 30 and 60° (see Figure A1 in Appendix A). Moreover, the discrepancies between crack types is most prominent for the long flaws — which have the lowest experimental UCS values. Conversely, the specimens with the highest experimental UCS (flaws with $\alpha = 90^\circ$) returned the least developed yielding pattern in the numerical results. This may be because the simulated load is relatively low (20 MPa) compared to their experimental strength (30-36 MPa). Therefore, the inconsistency between loading magnitudes in the experimental tests and numerical simulations might explain the discrepancies between the numerical and experimental crack types.

6.1.3 Shear failure indicated in numerical models

Table 17 informs that shear yielding occurred in almost every numerical simulation of ungrouted models. In every case with severe yielding (all lengths with dip angle up to 60°), shear yielding patterns initiated from the flaw tip. The shear yielding propagated $45-75^\circ$ from the horizontal plane, and is referred to as type IV. Further, less developed shear yielding was also found at the flaw tip for the cases with less prominent yielding. Conversely, shear cracks (type IV) only occurred in 5 cases in the lab experiments (for α between 45 and 75°). This might indicate that the shear strength that were used in the numerical models was lower than the actual material shear strength. Future numerical models might therefore be modelled with higher cohesion and internal friction angle.

6.1.4 Midflaw tensile cracks around ungrouted flaws

Another obvious difference between numerical and experimental results is the midflaw tensile crack that occurred in the numerical models containing ungrouted flaws of low dip angles. An example of this crack type was shown in Figure 31. Furthermore, the stress fields from linear-elastic models returned high tensile stress concentrations at the midflaw for flaws with $\alpha \leq 30^\circ$. This suggests that tensile cracks could originate from the midflaw position. However, midflaw tension cracks did not occur in the lab compression tests of ungrouted specimens.

For specimens containing horizontal and ungrouted flaws, the primary crack was type II in the lab experiments. Conversely, the first crack to initiate in the numerical simulations was the midflaw tensile crack. This was further demonstrated by reducing the load of the model and registering where the yielding first developed. It is difficult to explain these differences. However, the linear-elastic models returned high σ_1 concentrations at the tip of the ungrouted horizontal flaws. The linear-elastic stress field therefore points to both the midflaw and the flaw tips as areas where crack initiation is likely. Thus, it might be possible that primary cracks can initiate from the midflaw area in lab specimens. In fact, the photographed failure modes of the specimen containing a 20 mm long horizontal, ungrouted flaw showed cracking around the midflaw. However, Le et al. (2018) only registered the crack types type II and type VI (surface spalling) for this specimen. Figure 42 compares the failure mode from the lab results and the numerical results for the ungrouted 20 mm long horizontal flaw geometry. The numerical results show more severe cracking (yielding) and include more shear yielding than the experimental results. Apart from this, the results are similar, despite the fact that no midflaw tensile cracks or shear cracks were described for this flaw by Le et al. (2018). It can thus be suggested that despite discrepancies in observed crack types, the numerical and experimental results are consistent.

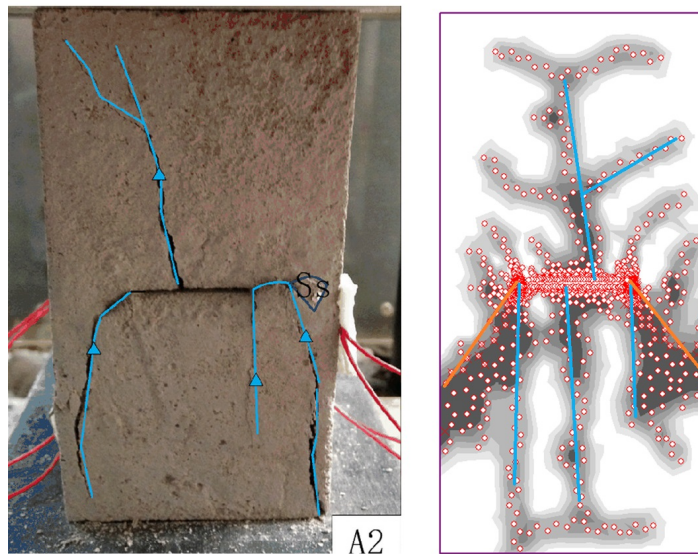


Figure 42: Left picture shows the failed specimen containing a 20 mm horizontal ungrouted flaw (obtained from Le et al. (2018)). The right contour plot gives the yielded elements for the numerical model with the same flaw geometry (see legend in Figure 28). Blue lines are tensile cracks. Orange lines are shear cracks.

In the numerical results, combinations of shear and tensile yielding characterize the failure modes. Some elements are yielding both in shear and tension. As mentioned in the introduction, cracks initiate at microscopic levels (Kranz, 1979, Eberhardt et al., 1999, Hoek and Martin, 2014). Moreover, interactions between microcracks and micropores are complicated, and the stress field experienced by microcracks differs from the applied stress field by both magnitude and direction (Kranz, 1979). This was also the case in the numerical simulations. As was seen in Figure 32, the stress field is rotated around the local yielded areas. Moreover, the yielded elements contour plots from the numerical models contained several elements that yielded both in shear and tension (Figure 43 b) is a good example). Literature (*e.g.* Kranz (1979)) and the numerical results therefore indicates that the tensile cracks that were described from the

experimental results, might actually experience combinations of shear and tensile stress modes in some situations. Some of the cracks from Le et al. (2018) may therefore be combinations of shear and tensile cracks, as opposed to being pure tensile or pure shear cracks, as Le et al. (2018) claimed. Consequently, the agreement between numerical and experimental results can be good, despite disagreement in crack modes (shear and/or tensile) or crack types (I-IX).

6.1.5 UngROUTED specimen strength based on flaw length and dip angle

In the numerical simulations, the percentage of the rock elements that yielded decreased when the dip angle of the ungrouted flaw increased (for all flaw lengths). A low yielded element percentage might indicate that the model has a higher strength (because the same load is applied to all numerical models). This might not be an accurate measure because models with different flaw geometries do not have identical meshes and the exact same total amounts of elements. However, the trend suggested by the elastoplastic numerical simulations is that the strength of the specimens increases when the dip angle increases from 0 to 90°.

The linear-elastic simulations returned $\sigma_{t,max}$ peaks on 45° or 60° (*i.e.* higher tensile stress concentrations around these flaws). Moreover, the $\sigma_{c,max}$ peaked on the $\alpha = 15^\circ$ for 30 mm long flaws and on $\alpha = 45^\circ$ for the 20 mm long flaws. This contradicts the tendencies from the yielded elements results (where the strength increased steadily with the dip angle — without any clear peaks). However, the maximal stress values from the linear-elastic simulations might be unrealistically high due to stress singularities (some values are close to 250 MPa, the top plate load is 20 MPa). The finite maximum concentration values that are given might therefore just be a function of the mesh resolution around the flaw (might approach infinity if finer meshes are used). This is discussed in Section 7.2. It follows that the elastoplastic results (yielded elements) are more realistic than the linear-elastic results. The linear-elastic results should therefore primarily be used to study tendencies in the stress field, and the returned maximal stress values should be interpreted with caution.

Le et al. (2018) similarly reported the highest UCS for specimens containing short flaws ($2a = 10$ mm) and flaws with high dip angles ($\alpha = 90^\circ$), as seen in Figure A1 in Appendix A. However, for the 20 and 30 mm long flaws, the experimental UCS increased for dip angles between 0 and 45°. This unexpected outcome was assumed to be due to the decreasing length of the failure path for these dip angles, and were explained as follows (Le et al., 2018): The flaws with the longer horizontal component of the flaw length (long flaw length and/or low dip angle) have a shorter distance from the flaw tip to the lateral side of the specimen. Moreover, this increases the likelihood that the cracks cut through the lateral side and cause failure of the specimen.

The results from Le et al. (2018) might have been more consistent if they used wider specimens. It would then be less likely that the primary cracks reached the lateral side of the specimen and potentially caused failure of the specimen before secondary cracks could develop — which was the case in Le et al. (2018) (manifested as surprisingly low UCS for 20 and 30 mm long flaws with $\alpha = [0, 15, 30]^\circ$). It would be interesting to see which secondary crack types that develop around long flaws with low dip angles ($2a = [20, 30]$ mm, $\alpha = [0, 15, 30]^\circ$) if wider lab specimens were used. It might be possible that the midflaw crack — which clearly occurred in the current numerical analyses of *e.g.* long horizontal flaws — can appear as secondary cracks in wider lab specimens. This is an interesting issue for further research. A study similar to the UCS-tests by Le et al. (2018) should therefore be repeated using wider specimens relative to the horizontal flaw length component. However, before this suggested study is undertaken, a dimensional analysis should be carried out to investigate the minimum specimen width that is necessary to prevent cracks from reaching the lateral side of the specimen for the longest flaw. A possible approach for this dimensional analysis is to take a specimen from Le et al. (2018) where cracks did not reach the lateral specimen side. Further, the ratio between the specimen width and the horizontal flaw component of this specimen can be calculated. Finally, the necessary new specimen width is found by multiplying this ratio by the horizontal component of the flaw that has the longest length and lowest dip angle (that is going to be studied in the new project).

6.2 Grouted rocks

In the experimental uniaxial compression tests of specimens containing a grouted flaw, the flaw types I-II and V-IX occurred. The numerical simulations of the uniaxial loading of grouted models returned four typical crack types (yielding patterns): Type I-III and shear yielding close to the flaw tip. See Table 18. As discussed in the previous section, the crack types V-VII are not expected in continuum FEM models (hence the parenthesis notation). The discussion of grouted specimen failure modes further focuses on the different crack types that originated from the tip or midflaw area of grouted flaws.

6.2.1 Far-field and flaw-tip tensile cracks in grouted rocks

In every numerical simulation of grouted models, tensile yielding originated from the flaw tip. Conversely, in 12/21 of the grouted flaw lab cases, no tensile cracks initiated from the flaw tip. This is a pronounced difference between the numerical results and the experimental results from Le et al. (2018). In for example the specimen containing a grouted 10 mm long flaw with $\alpha = 0^\circ$, crack type V — which initiates in a position far from the flaw — was the only observed crack type. In other specimens, the critical failure plane developed in the lateral side of the specimen, and not in the plane containing the grouted flaw. Moreover, the UCS-values of these specimens were close to the UCS of the intact rock (42 MPa). This might imply that for these specimens, the preexisting defects such as micropores and microcracks were more critical stress concentrators than the actual grouted flaw. In the continuum FEM models however, the flaw — regardless of length and orientation — is the only stress concentrator. This explains why the yielding initiated from a position around the flaw in every simulated UCS test.

The tensile yielding that occurred in the numerical simulations resemble the typical wing crack. As mentioned in the introduction, the wing crack initiates at the tips of inclined penny-shaped flaws and grows parallel to σ_1 (see Figure 1). Similarly, yielding initiated at the tips of the grouted (or ungrouted) flaws and propagated in the direction of the applied load in the numerical models. Examples of yield contour plots that are similar to the wing crack are seen in Figure 29 (right subfigure) and Figure 45 (bottom row and upper left subfigure). The wing crack pattern was a typical result for the grouted models, but it also occurred in a few ungrouted cases (for example when $\alpha = 75^\circ$).

Table 18: Crack types observed in numerical simulations and the lab results (from Le et al. (2018)) for rocks containing grouted flaws of different length and dip angle combinations.

Flaw geometry		Observed crack types (grouted flaws)	
$2a$	α ($^\circ$)	Numerical results	Experimental lab results
10 mm	0	II	(V)
	15	II	N/A
	30	II, shear at tip	(V, VII)
	45	I, II, shear at tip	(V, VI)
	60	II, shear at tip	II, (VI), IX
	75	II	(V), IX
	90	II	N/A
20 mm	0	II	I, (V, VI, VII), VIII
	15	II	II, (VI), VIII
	30	II, shear at tip	(V, VI, VII), VIII
	45	II, shear at tip	II, (V, VI),
	60	II, shear at tip	I, II, (VI), IX
	75	II, shear at tip	II, (VI), IX
	90	II	(V, VI, VII), VIII
30 mm	0	II close to tip	(V, VII)
	15	II, shear at tip	II, (V, VI, VII), VIII
	30	I, II, III, shear at tip	(V, VI, VII), VIII
	45	I, II, shear at tip	(V, VI), VIII
	60	II, shear at tip	II, IX
	75	II, shear at tip	I, (VI), IX
	90	tensile at tip	N/A

6.2.2 Midflaw tensile cracks in grouted rocks

Crack type VIII is a tensile crack that initiates from a point away from the grouted flaw tip, develops in the loading direction and cuts through the grouted flaw. This crack type occurred along with spalling in the lab tests of grouted specimens (Le et al., 2018). In the grouted perfect brittle numerical models, this crack type was not observed. However, crack VIII resembles the midflaw tensile crack that occurred in the simulations of ungrouted models. The ungrouted numerical models were loaded closer to their experimental UCS than the grouted models. (The simulated load was 20 MPa, the UCS of grouted models ranged from 35-43 MPa.)

In the perfect plastic models loaded with 28 MPa (code validation task), midflaw yielding developed around the horizontal flaw (see Figure 34). Consequently, an additional perfect brittle simulation of a specimen containing a 10 mm long horizontal grouted flaw, loaded with 28 MPa was done. The goal was to find if crack type VIII or midflaw yielding could develop as a secondary crack type in this model. The resulting contour plot returned a critical failure plane yielding in tension and shear, which can be seen in Figure 43. Moreover, shear and tension yielding occurred at the midflaw, and cut through the grouted flaw as marked in Figure 43. These results prove that midflaw yielding could occur in grouted simulations if the loading increased.

Figure 43 further compares the simulation of a 10 mm horizontal grouted flaw loaded with 20 MPa and 28 MPa, and the failure modes for this grouted flaw geometry from Le et al. (2018). It can be seen that the tensile yielding marked as crack type II in Figure 43 a) developed when the loading increased (Figure 43 b). This yielding pattern resembles the crack type V that was observed by Le et al. (2018) and is shown in Figure c). A pronounced difference is the plane that yields in shear and tension and cuts through the specimen in a direction about 45° from the applied load. However, the experimental and numerical results are similar. Moreover, the tensile crack in the experimental results (type V) initiated at an inhomogeneity in the rock, and the first numerical tensile crack initiated close to the flaw tip (type II). This implies that the failure modes occurring in the simulated uniaxial compression tests can be consistent with the lab results, even though the match in crack types is not perfect (which was also the case for the ungrouted numerical flaws, as discussed in 6.1.4).

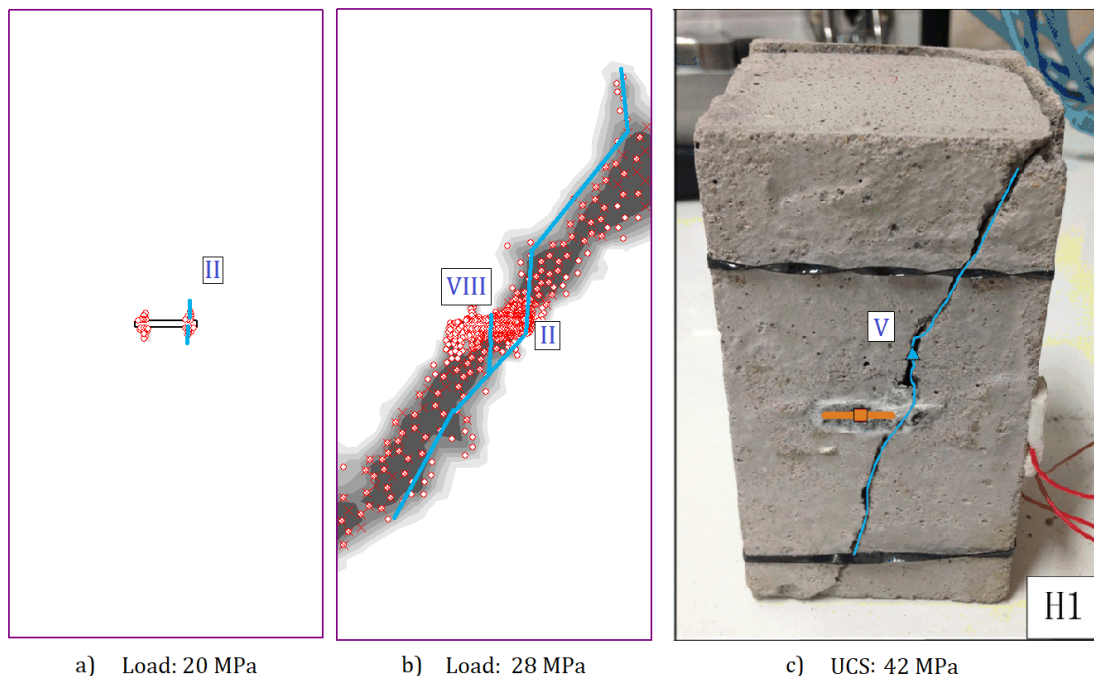


Figure 43: Specimens containing a 10 mm long grouted flaw ($\alpha = 0^\circ$). a) gives the yielded element contour plots with an average top plate load of 20 MPa. b) shows the yielded elements when the load is increased to 28 MPa. c) shows the experimental results (obtained from Le et al. (2018)). Blue lines mark tensile cracks, orange line outlines the grouted flaw. See legend in Figure 28.

6.2.3 Shear cracks in grouted rocks

Le et al. (2018) observed crack type IX in the failed grouted rocks with dip angle 60 and 75°. IX is a shear crack that initiates at the rock-epoxy interface and propagates in a direction parallel to the flaw inclination. The numerical models that were loaded with 20 MPa experienced shear yielding at the flaw tips. IX was however not observed in these results. Intuitively, this crack type is not expected in the simulated results because the material boundary is modelled with continuum elements and have infinite shear strength. In future investigations, this boundary can be modelled with interface elements. (This is further discussed in Chapter 7.) However, when the assigned load on the numerical models are increased, elements will eventually yield in shear around the flaw. An example of this was given in Figure 43 b).

Similarly to the ungrouted specimen results, shear yielding occurred in many of the grouted model simulations (12/21 cases). Only 6 shear crack cases developed in the 21 grouted lab tests. This might again indicate that the shear strength of the numerical models was too low.

6.2.4 Grouted specimen strength based on flaw length and dip angle

In the lab tests, Le et al. (2018) experienced that the UCS for the grouted specimens was lowest for flaws with $\alpha = 60^\circ$. The failure mode of these specimens had combinations of crack type II and IX. Le et al. (2018) thus concluded that this crack combination efficiently degenerates the specimen strength. Moreover, the UCS of the grouted lab specimens was highest for specimens containing flaws with dip angles of 0 and 90°. Consistent with the lab results, this research found that models containing grouted flaws with a low dip angle ($\alpha = 0^\circ$) and a high dip angle ($\alpha = 90^\circ$) returned the lowest amount of yielded rock elements (0.6-2.6%). However, the amount of yielding was highest for flaws with dip angles from 30 – 60°, and peaked for the 30 mm long flaw with $\alpha = 30^\circ$ (17.2% of the rock elements yielded). The numerical results are therefore not in complete agreement with the lab results.

A possible explanation for this disagreement might be that the numerical models assigns a grouted material to the flaw that is both perfectly homogeneous and that accurately fills the flaw void. In the practical tests, the grout (epoxy) might not adhere perfectly to the rock material at all flaw boundary locations. Moreover, the density of the flaw might not be continuous over the entire flaw volume for the following explanation. The specimens containing the grouted flaws were left to cure for 3 days after injection. During a 3 day curing time, it is possible that the epoxy sinks to the lowest areas of the flaw (due to gravity) before it hardens — if the specimens were not rotated regularly. It follows that the epoxy might be more concentrated in the bottom of the injected flaw in practical grouted flaws (see figure 44). This can result in features such as local areas of lower density and microscopic voids in the upper parts of the flaws in lab tests. Further, these inhomogeneities can act as stress concentrators that induce cracking and therefore potentially reduce the specimen strength. Moreover, this effect might be more clear for flaws with a high inclination angle (if the specimens are stored on their short sides during curing). This is another possible explanation for why specimens with grouted flaws with inclination angles $\alpha = [60, 75]^\circ$ had relatively low UCS (and different crack types) compared to specimens with α ranging from 0-45° in the lab tests.

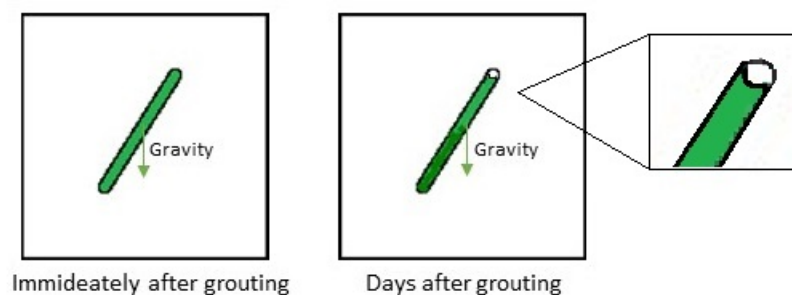


Figure 44: Schematic of possible grouting results in the time after injection (exaggerated).

Nevertheless, both experimental and numerical results suggest that the strength of grouted rocks is highest for grouted flaws with dip angles of 0 and 90°. Section 6.3.2 discusses the stress field around grouted (and ungrouted) flaws and possible explanations for why the strength varies with dip angles.

6.3 Grout reinforcement effect

This section addresses the strengthening effects from grouting. First, it outlines the strengthening effects in terms of yielded elements. It will then go on to discussing how grouting improves the strength of rocks and which mechanisms that are responsible for the grouting strengthening effect.

6.3.1 Yielding

The experimental design task found that under the same loading magnitude, the percentage of the rock elements that yielded was reduced by grouting in 20 of 21 cases (see Table 11). Because the same mesh was used for the rock material section in both the models containing ungrouted and grouted flaws of the same flaw geometry, mesh effects can be ruled out. The numerical results therefore indicated a pronounced grout reinforcement effect. This finding is consistent with the results from Le et al. (2018), where the UCS of the rock was higher for the grouted cases than the ungrouted cases with matching flaw geometries.

Le et al. (2018) observed that the strengthening factor was highest for the 30 mm long flaws with low dip angles ($\alpha = [0, 15]^\circ$) and lowest for all flaw lengths with dip angles of 90° (see Figure 5). The results from this study further support these observations. Numerical models containing the lowest dip angles ($\alpha = 0$ and 15°) indicated the most evident grout reinforcement effect. For the model containing a 30 mm long flaw, the amount of yielded rock elements decreased from 55% to 1% due to the grouting. Moreover, the models containing 20 mm long and 10 mm long horizontal flaws produced reductions of 54 and 40 percentage points respectively. Models containing vertical flaws moreover indicated the lowest strengthening effect. In these cases, the reduction in yielded element percentage ranged from 0.0-0.4%. These findings are in agreement with those of Le et al. (2018), who reported the highest strengthening factor on specimens with low flaw dip angles and vice versa. Moreover, vertical flaws are oriented parallel to the applied load, and clearly had the lowest stress concentrations on the flaw tips in both the grouted and ungrouted cases. A low strength reinforcement effect was therefore expected for the flaws with the highest dip angles.

In the literature (Le et al., 2018) and numerical results, the grout reinforcement effect was found to be most pronounced for long horizontal flaws. This was also the case for the numerical models. An example of how flaw length affects the grout improvement in numerical models can be seen in Figure 45. The figure compares the yielded elements for ungrouted and grouted flaws with dip angle 60° and varying flaw lengths. The geometry with $2a = 30$ mm shows a significant reduction of yielded elements from the ungrouted to the grouted model. Conversely, the yielding around the ungrouted and grouted 10 mm long flaws are more similar.

Le et al. (2018) observed that specimens containing flaws with dip angle of 60° had relatively large strength improvement compared to $\alpha = 45^\circ$ and $\alpha = 75^\circ$. Overall, the simulated yielded element improvement decreased when the dip angle increased for most flaw lengths, without any clear peaks. However, the yielded rock percentage peaked for the grouted flaws with dip angles from 30° to 60°. This indicated that the grout infilling itself could induce some stress concentrations that caused additional yielding for some flaw dip angles. This is discussed in the following section.

6.3.2 The stress field before and after grouting

The research by Le et al. (2018) concluded that stress reduction at the flaw tip is one of the mechanisms behind grout reinforcement (in addition to improved shear-strength along the flaw interface). Moreover, this thesis examined the stress distribution in numerical models of grouted and ungrouted rocks. The major result from the stress analysis, is that the stress concentrations were significantly lower in the grouted models than the ungrouted ones.

The σ_1 and σ_3 contour plots produced from the grouted and ungrouted simulations showed significant stress reduction from grouting. As seen in Figures 24 and 25, the ungrouted stress plots have relatively high tensile stress values around the midflaw (-16 MPa which was 50% of $\sigma_{t,max}$), where the grouted models returned low compressive stress (*ca.* 0 MPa). In the ungrouted models, the stress is rotated about the open flaw, which cannot carry stress (unless the loading closes the flaws and gives contact between the long flaw boundaries). This can further be seen in Figure 32. The stress rotation around the ungrouted flaws explain the tensile stress concentrations in this area. Moreover, when the flaw is grouted, it may hold a portion of the applied load. Thus, the entire load does not need to be redistributed around the flaw. However, the epoxy has a lower Young's modulus than the rock material (1.2 GPa compared to 19.6 GPa). According to a linear load-displacement curve, the epoxy holds less load than the rock when the two materials have the same displacement — which is the case for grouted non-persistent flaws, because the epoxy is captured inside a frame of rock. Thus, some stress still needs to be redistributed around the flaw in the grouted models. The ability of the grouted model to hold a portion of the applied load explains why the stress concentrations were lower in the grouted models. The stress reduction results are in agreement with the findings of Le et al. (2018).

The results also point to the fact that the grouted flaw induces some stress concentrations close to the flaw. These stress buildups were ascribed to contrasts in stiffness and lateral expansion in the rock and epoxy material. The epoxy has a higher ν than the rock (0.45 compared to 0.18), and therefore expands more in the direction orthogonal to the loading direction. However, the epoxy is restrained by the stiffer rock frame, and will thus not be able to expand. Instead, the epoxy will put additional stress on the area surrounding the flaw. The experimental design simulation of a model containing a 30 mm long grouted flaw with $\alpha = 30^\circ$ produced the highest degree of yielding around the flaw (amongst the grouted simulations). 17.2% of the rock elements yielded in this case. When ν was decreased from 0.45 to 0.20, the amount of yielded rock elements decreased to 7.3%. This may have implications for the choice of grout qualities in rock mass grouting. The Poisson's ratio of the grout should not be in great contrast to the Poisson's ratio of the rock material. However, the rock-epoxy material boundary was modelled with infinite shear strength, which might lead to local stress concentrations at the material boundary due to the stiffness contrasts in the material. This is discussed in Chapter 7.

6.4 Overall agreement between numerical models and literature

This section briefly outlines the most important similarities and differences between the numerical simulations, the lab work by Le et al. (2018) and other literature (*e.g.* Kranz (1979), Hoek and Martin (2014), Ashby and Sammis (1990)). For the ungrouted flaws, the agreement is good in terms of the initiation points of the tensile cracks. Tensile crack originating from the flaw tip (I, II or III) occurred in every case, in simulations and lab. However, the numerical models indicated more shear failure than the experimental results.

The biggest inconsistency between the numerical and the experimental results were the midflaw yielding/type VIII. Type VIII did not occur as primary cracks in the grouted numerical models. Moreover, the primary cracks always initiated at the flaw tips in the grouted numerical models. In the grouted lab tests, cracks did not always initiate at the flaw tips, and type VIII was a commonly occurring crack type. The shear crack IX that developed in grouted lab specimens, was not observed in the numerical models. This is because the rock/epoxy interface was modelled with infinite shear strength.

There was not a perfect match in observed crack types from simulations and lab experiments. Compared yielded elements contour plots and photographs of failed lab specimens however indicated that the failure modes are similar, despite inconsistencies in observed crack types. Moreover, the numerical results are consistent with other literature (*e.g.* Kranz (1979), Hoek and Martin (2014), Ashby and Sammis (1990)). The tensile cracks that initiated at the flaw tips always propagated in the direction of the applied load. In many cases, the contour plots produced a yield pattern that was similar to the typical wing crack described by Ashby and Sammis (1990).

In terms of strength improvement, the agreement between the experimental and numerical results was good. Both implied highest strength improvement for the lowest angles, and vice versa. Grouting was also found to reduce the stress concentrations at the flaw tip and around the flaw in the numerical models. Similarly, stress reduction was outlined as an important strengthening mechanism from grouting by Le

et al. (2018).

The next chapter provides a thorough discussion on the assumptions that were made in the numerical modelling. Moreover, the chapter provides possible explanations for some of the discrepancies between the experimental results and the numerical results in more detail.

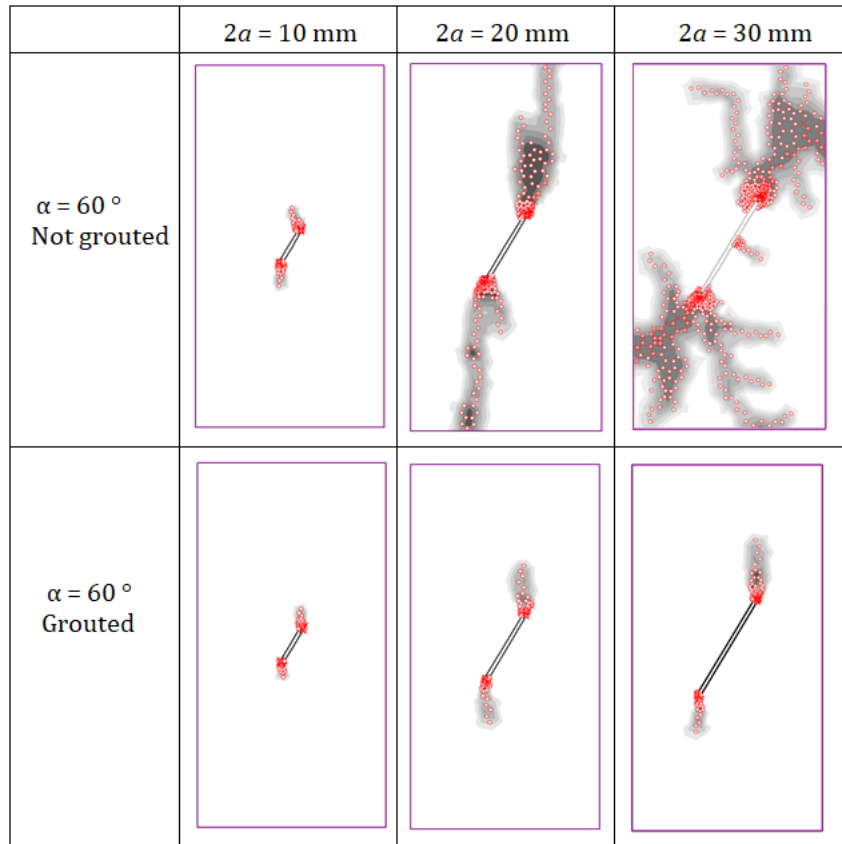


Figure 45: Yielded elements for ungrouted (top row) and grouted flaws (bottom row) with $\alpha = 60^\circ$ and varying flaws lengths. Circles indicate tensile yielding, crosses mark shear yielding (see legend in Figure 28). A significant reduction of yielding can be seen in the grouted cases. The applied load is 20 MPa in all models.

7 Discussion of the Numerical Models

The experimental design simulations of this study investigated the agreement between two-dimensional numerical models and the laboratory experiments performed by Le et al. (2018). In addition, three-dimensional numerical analyses of the uniaxial compression tests were carried out. Because RS2 is not developed for 3D analysis, ABQ (Abaqus/Standard) was used for this purpose. Before 3D models were made in ABQ, it was chosen to build and compare 2D models in both RS2 and ABQ. This gives a better understanding of the disagreements between the two-dimensional RS2 models and the three-dimensional ABQ models, and whether the deviations are attributed to program differences (such as iteration solvers) or are results of adding the third dimension. Additionally, repeating simulations with several codes might help validate the results from the two programs.

First, this chapter provides a comparison of the different numerical models. A discussion on general challenges that occurred in this project follows. Finally, the codes ABQ and RS2 are compared, and problems and other experience from working with these programs are discussed.

7.1 Agreement between the models

In this thesis, uniaxial compression tests of specimen were modelled with varying material behaviour and loading magnitudes. Simulations were carried out in the programs RS2 and ABQ. Moreover, both 2D and 3D simulations were run. This section compares the results and discusses the agreement between the different models.

7.1.1 Agreement between RS2 and ABQ results

Uniaxial compression tests of models containing 18 different flaw geometries and an intact model were simulated in RS2 and ABQ. All models were assigned a -0.14 mm displacement in the top plate (about 27-28 MPa in compression). The presented results were the maximal stress values (from linear-elastic simulations), stress contour plots and yielded elements contour plots (from elastoplastic simulations).

The agreement between the contour plots produced by the two programs was generally good. The σ_1 contour plots from the elastoplastic models showed differences between 1-2 MPa in most parts of the models containing grouted flaws (which makes up 1% of the maximal σ_1 magnitudes). Furthermore, the programs agree on the locations of the maximum stress concentrations (which were at the flaw tips), and the shapes of the stress contours and yielded elements contours. In the yielded element contour plots, the location, length and angle of the yielded zone were similar in both programs. At local points close to the flaw tip, RS2 and ABQ results disagreed on the maximum stress concentrations — both in the elastoplastic and linear-elastic results. This disagreement was most prominent for the linear-elastic models. In local points around the flaw tip, the deviation of stress magnitudes from the RS2 to the ABQ results was up to 50% (linear-elastic models). This may be due to stress singularities, which is discussed in Section 7.2.

Naturally, the flaw was an important feature in the current study. However, the flaw geometries complicated the models and the meshes. The most simple models — which were the intact models containing no flaws — showed excellent agreement in terms of the stress values. There was a 0% error between the σ_1 and σ_3 values produced by ABQ and RS2, despite different mesh resolutions being used. Moreover, the meshes that were used in ABQ were in most cases considerably finer than the RS2 meshes (up to 50% more elements in ABQ). The inconsistency between the mesh resolution in ABQ and RS2 — which is especially prominent around the flaw — is a likely cause for the stress differences between the two programs. Different stopping criteria and iteration methods are used in the two programs. This is another possible explanation for the deviation between the results from the elastoplastic (non-linear) models simulated in ABQ and RS2. This is further discussed in Section 7.2.3.

7.1.2 2D and 3D models

As mentioned in Chapter 4, the 2D/3D validation task compared results from two- and three-dimensional uniaxial compression test simulations. Moreover, two- and three-dimensional models containing one flaw geometry — a 20 mm long grouted flaw with a dip angle of 30° — were studied. The assigned top plate displacement was -0.10 mm (20 MPa in compression) in every simulation. Moreover, the simulations were repeated with different mesh resolutions (mesh 1-5) and stress assumptions (plane strain, plane stress, 3D stress).

Overall, the agreement between the elastoplastic 2D and 3D models was fair. The most important agreements and disagreements can be summarized as follows:

1. The maximum compression stress magnitudes were *ca.* 6% higher in the 2D model compared to the 3D model;
2. The maximum tensile stress magnitudes were up to 76% higher in the 2D model than the 3D model;
3. The deviation was lower within the grouted flaws (where both the 2D and 3D models showed 7-8 MPa) and in the far-field areas;
4. The maximum stress concentrations were consistently located at the flaw tip in the 2D models (both plane stress and plane strain) and in the 3D models;
5. The 3D models produced tensile stress around the midflaw area, where the 2D plane strain model produced compression stress (in the σ_3 contour plots);
6. In both the 2D and 3D models, the yielding initiated at the grouted flaw tip and grew in a direction 60-90° from the horizontal line.

Together, points 2 and 5 along with Figure 39 indicate that the 3D models produced lower maximum tensile stress magnitudes because the tensile stress was distributed over a larger area in the 3D models (compared to the 2D models). Particularly, the 3D model predicted tensile stress around the midpoint of the flaw, where the 2D models did not predict tensile stress. The midflaw area was also a topic of discussion in Chapter 6, where disagreements between the experimental (lab) results (Le et al., 2018) and the perfect brittle 2D models emerged. In the grouted lab cases, primary cracks (type VIII) often initiated close to the midflaw area. However, in the grouted numerical models, the primary cracks always initiated at the flaw tips. To sum up, the 3D models produced more tensile stress around the midflaw (than the 2D models), and the experimental study observed more tensile cracks originating from the midflaw (than the 2D models). It follows that the stress field produced by the 3D models might be more consistent with the lab results.

The perfect brittle 2D analysis assumed plane strain conditions (the strain in one direction is assumed to be zero). Additionally, a linear-elastic 2D analysis with plane stress elements was carried out (the stress working on the plane was assumed to be zero). The 2D plane stress linear-elastic analysis produced a σ_3 stress field that was more similar to the 3D model σ_3 stress field at the midflaw than the 2D plane strain σ_3 stress field (in terms of tensile stress). Because the 3D models appeared more consistent with the lab results (Le et al., 2018) than the 2D plane strain models, the plane strain assumptions might not be accurate enough for the current model geometry/problem. This suggests that more 3D models should be carried out. However, 3D models have a considerably higher computational cost. Moreover, the current project further experienced challenges with the 3D modelling, including more convergence problems and the some stress errors around the flaw. Moreover, the attempts of simulating 3D models with perfect brittle material behaviours were not successful. This implies that the 3D models used in the current study need to be developed further.

The remaining part of this chapter addresses the challenges experienced with the 3D models that were simulated in the current thesis work. Moreover, it provides suggestions and recommendations for the design of 3D models in future simulations of uniaxial compression tests of grouted rocks.

7.1.3 Unexpected nonzero σ_z buildups along material boundary in 3D models

In the current study, the three-dimensional models produced some unexpected nonzero σ_z concentrations close to the flaw boundary in the outer x-y-planes. One of the outer x-y-planes is marked as the blue plane in Figure 46, which also indicates the directions of the load (σ_y) that works on the 3D model. σ_z concentrations — which go perpendicular to the plane containing the flaw — occurred along the rock-epoxy boundary. As seen in Figure 46, this plane was not loaded in z-direction. Additionally, the plane was not restrained in z-direction. The σ_z values were therefore expected to be approximately 0 MPa on the entire plane. Mesh-refinement tests and material tests were carried out to investigate these unexpected σ_z concentrations. These tests also examined the stress values on the x-y-plane that cut through the middle of the specimen. An objective was to examine whether the unexpected σ_z buildups could help explain the tensile stress disagreement between the 2D (plane strain) and 3D models around the midflaw area.

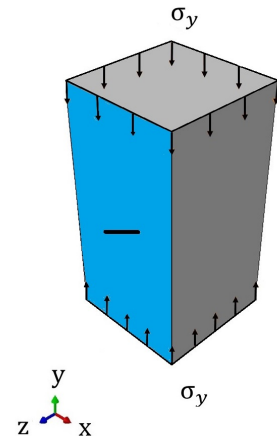


Figure 46: The applied load to the 3D models was applied in y-direction. The blue plane indicates one of the outer x-y-planes, where some unexpected σ_z concentrations occurred.

Implications of the mesh-refinement test and material test findings

Increasing the 3D mesh density from mesh 1 with 12060 elements and mesh 5 with 47040 elements had no considerable effects on the σ_z concentrations around the flaw — in neither of the examined planes (outer and middle x-y-planes). However, when the element order was increased from first order (25755 nodes) to second order (125713 nodes), the stress concentrations in points close to the midflaw actually increased in the outer plane. This is because the nonzero σ_z values were more concentrated in a smaller zone surrounding the material boundary — both on the inside and outside of the flaw. These results indicated that the material boundary itself — *i.e.* the shared lines between the rock material elements and epoxy material elements — causes the unexpected σ_z concentrations.

The material boundary σ_z buildups might be explained by the chosen element types and the contrast in the stiffness (E) and expansion in the z-direction (ν) between the materials. The epoxy has lower E and higher ν values, and expands more in z-direction than the rock. Moreover, the rock elements and epoxy elements are connected at shared lines with an infinite shear strength and can therefore not slip. The inside (epoxy side) of the material boundary is under compression σ_z , which is stress that works towards the specimen core. Further, the outside (rock side) of the boundary is under tensile σ_z — indicating that stresses attempt to push the rock outwards, away from the specimen core. The infinite shear strength is what prevents the relative movements and captures the σ_z stress. This hypothesis was further explored by increasing the E (from 1.2 to 10 GPa) and decreasing ν (from 0.45 to 0.18) in the epoxy to approach the properties of the rock ($E = 19.6$ GPa and $\nu = 0.18$). When the contrast in the material behaviour decreased, the σ_z concentration along the flaw boundary was reduced significantly in the outer x-y-plane (from -2.6 MPa to 0.3 MPa at the midflaw). These findings support the idea that the unexpected σ_z concentrations were caused by the infinite shear strength material boundary combined with the contrast in material stiffness.

The mesh-refinement tests and material parameter studies provide explanations for the unexpected σ_z concentrations in the outer x-y-planes. During the two- and three-dimensional mesh and material simulations, it was further explored whether the σ_z buildups are related to the disagreement in stress values between the 2D and the 3D models at the midflaw (which was discussed in Section 7.1.2). For this purpose, σ_z values were obtained from the midflaw (location C in Figure 40) in both the middle x-y-plane and the outer x-y-plane of the model. The unexpected σ_z effects appeared to be most significant in the outer x-y-plane, and were reduced when moving inwards in the model. Moreover, the σ_z values obtained from point C in the middle x-y-plane remained relatively stable in the mesh refinement tests. In the elastoplastic h-mesh-refinement tests, the middle plane $|\sigma_z|$ values increased by 5% when the number of elements increased. The σ_z values lay close to the registered σ_3 stresses in the midflaw area (*ca.* -0.4 MPa),

and no yielding occurred in this area. In the linear-elastic p-refinement test, the stress values at point C in the middle x-y-plane increased by 0% when the element order increased from linear to quadratic. Conversely, in the outer x-y-plane (where the unexpected σ_z concentrations occurred), the values in point C were more unstable as the mesh refinement increased. From the elastoplastic h-refinement tests, the $|\sigma_z|$ results in the outer x-y-plane increased by 38% at point C. In the linear-elastic p-refinement test, the outer plane $|\sigma_z|$ values increased by 59% at the same location. Taken together, these results indicate that middle x-y-plane σ_z values are more stable than the outer plane σ_z values under mesh refinement. Therefore, these findings suggest no clear connection between the midflaw tensile stress in the 3D model (which did not occur in the 2D models) and the unexpected σ_z effects in the outer x-y-plane. Moreover, the tensile stress at the midflaw in the 3D models — which was in disagreement with the 2D models — cannot be claimed to be a modelling error and ruled out.

Suggestions for further research on 3D models

The unexpected σ_z concentrations and the 2D and 3D disagreement about tensile stress at the midflaw are issues for further work. Moreover, the mesh-test and material-test results suggest that the use of regular continuum elements — rather than cohesive elements — may cause errors in the model. Research that explores 3D flaw geometries modelled with cohesive elements along the rock-grout interface should therefore be undertaken. In such studies, it would be interesting to compare stress values close to the flaw boundary when the shear strength of the rock-grout interface is reduced. However, convergence problems were a noteworthy challenge in the work in Abaqus/Standard. Simulating a 3D compression test of a rock specimen containing a non-persistent flaw modelled with cohesive elements may thus be relatively time-consuming or challenging in Abaqus/Standard.

7.2 Challenges with the design

Finite element analysis takes a continuous geometrical model and assigns it material properties, boundary conditions/loading, and a mesh. The basis for the current analyses was specimen geometries, material properties and loading procedures from the laboratory experiments by Le et al. (2018). The numerical simulations aimed to match the lab experiments, and therefore use the given geometry and material information from the lab tests. However, in order to build FEM models that converged, adjustments were necessary. This section outlines and discusses challenges in this project, and how they were met.

7.2.1 Challenges with the geometrical model

The flaw is relatively thin compared to the length, and has sharp corners. Therefore, the flaw geometry is relatively challenging to model. The sharp corners — even with fillets — cause high stress concentrations. In linear-elastic analysis, these local points may act as stress singularities, which are points where the stress values do not converge. However, due to the discretization, the method returns finite stress values in these points. In any case — stress singularities or not — FEM simulations come with a solution error. This is because a continuous structure is discretized with a finite amount of elements. This error decreases when the the element size decreases (the number of elements increases). If an infinite amount of elements were used, the solution error would be zero (Kurowski, 2004).

Stress singularities could be investigated further with mesh refinement tests. Mesh refinement tests are carried out by increasing the mesh density gradually and checking if the maximal stress values converge to finite value as the density increased. Mesh-refinement tests were actually performed in this study. In these tests, the amount of elements (h-convergence test) and the order of the elements (p-convergence test) were increased. The main purpose of these tests were however to examine effects at the midflaw area, which is discussed in Section 7.1.3. The h-convergence test was performed with elastoplastic material properties (the primary area of interest for this test — the midflaw — remained elastic). It follows that the h-tests did not investigate the sharp corner stress singularities, as the elements around these points yielded. Moreover, only one step of the p-convergence test was performed. This step returned high convergence errors (27% for $\sigma_{1,max}$ and 50% for $\sigma_{3,min}$). Only first and second order elements are available in the ABQ continuum element library. Consequently, performing more p-convergence steps was

not possible in ABQ. If the convergence error for the next steps (increase in element order), remained high, it would indicate that the stress values diverge in the point of interest.

Nevertheless, when the structure is modelled with elastoplastic material behaviour, the areas with stress singularities yield when a certain stress threshold is reached. Yielded elements hold relatively low stress concentrations. Elastoplastic models can consequently solve stress singularity challenges, and such models were used in this thesis work.

7.2.2 Challenges with the material properties

Elastoplastic material models were attempted in each simulation set. In RS2, the elastoplastic simulations were relatively successful, because the models converged with the desired material properties (perfect brittle). In this case, convergence means that force equilibrium in the iteration process was accepted within the defined tolerance limits.

As opposed to the success in RS2, perfect brittle models did not converge in ABQ. Possible explanations for why models converge in RS2 and not ABQ are discussed in Section 7.2.3. It however appeared that models with severe yielding (which was the case for the brittle models), and especially tension yielding, do not converge in ABQ. The models were therefore designed with perfect plastic material behaviour, and with improved tensile strength ($\sigma_t = 6.0$ MPa compared to $\sigma_t = 4.1$ MPa). When these material parameters were applied to the various flaw geometries, the grouted models converged. Conversely, the ungrouted models did not converge until the tensile cutoff was increased to 11 MPa. This was assumed to be a high overestimation of the practical tensile strength, and it was therefore chosen to call off the ungrouted model simulations in ABQ.

In addition to changing the material behaviour and improving the tensile strength, reducing the load was attempted. This strategy was not successful — the simulations did not converge until the load was so low that the entire model remained elastic (*i.e.* no yielding occurred). It appears that models where tensile yielding occurs are unstable in ABQ. This may be due to the implementation of the MC-criterion and tensile cutoff in ABQ, or a general challenge in this program. In future ABQ simulations of similar structural problems, it could be attempted to model the material tensile strength with different failure criteria.

However, this was not done in this thesis. The RS2 simulations had returned useful results from perfect brittle models. Moreover, the linear-elastic stress results are still useful for understanding of the stress field around the flaw, even if the stress values may diverge or be unrealistically high in certain locations.

7.2.3 Experience with Abaqus/Standard and RS2

In the current study, the FEM codes Abaqus/Standard and RS2 were used. Both RS2 and ABQ include modules for the basic FEA steps. This includes modules for designing the geometric model, defining material properties, applying loading/boundary conditions, meshing, computation and result visualization. ABQ is a general-purpose product, and RS2 is developed specifically for rock/soil analysis. Advantages, disadvantages and challenges that occurred in RS2 and ABQ are outlined in this section. The section focuses on the major challenges that arose during this thesis work. Moreover, recommendations for use of these programs in future research are given.

RS2 advantages and disadvantages

RS2 was generally a code that worked well in this project. There were however a few disadvantages related to the geometry design module. 3D analysis was an important part of this study, and is also recommended for further work (as discussed above). The most important limitation with RS2 is that it does not include 3D modelling (except for axisymmetric models). Moreover, the CAD-module is developed specifically for *e.g.* underground excavation and slopes. The program does not include advanced design tools for easy or fast drawing of all kinds of geometries, including the rotated flaws. Consequently, the 21 flaw geometry pairs were not designed directly in RS2 (this would have been too time-consuming). The flaw vertex

coordinates were instead calculated according to trigonometric principles in a spreadsheet and imported to RS2 before the corner fillets were added in RS2. This method allowed quick and accurate geometry design, and did not require advanced coding skills. The simple RS2 CAD-module was therefore not a problem in this project.

RS2 included several advantages for this project. Because RS2 is designed for rock problems, the material module allows easy implementation of the MC-criterion. Mohr-Coulomb materials, behaving from perfectly brittle to perfectly plastic could easily be assigned to the rock specimens. Further, all models converged in RS2, which is, of course, an essential advantage. RS2 uses the accelerated initial stiffness method, which was found to be robust in severe yielding cases in a previous study (Dang et al., 2014). This coincides with the experience from this work — there were no convergence issues and generally low computational costs (models were computed in under 5 minutes). The comprehensive stopping criteria — which stops the iteration process when an equilibrium of energy, force and displacement is met within a specified tolerance limit — may also improve the numerical stability of the model. However, stopping criteria and high tolerance limits may lead to false convergence and less accurate results. Conversely, use of lower tolerance limits improves the accuracy, but gives higher computational cost. In this study, many simulations were repeated, and low computational cost was desirable. The main purpose of the research was to compare numerical yielding patterns to experimental crack types, and general tendencies were more interesting to study rather than *e.g.* obtaining accurate stress values. The default tolerance value suggestion was therefore used for every simulation.

Moreover, the visualization module of RS2 returns whether the elements yield in shear and/or tension (unlike ABQ). This was useful when comparing numerical failure patterns to the crack types that were described in the literature, and therefore provided a better understanding of the numerical results.

Abaqus/Standard advantages and disadvantages

The ABQ geometry design module is versatile and provides tools for designing a variety of 2D and 3D geometries. Flaw geometries could be designed efficiently and accurately directly in ABQ, in both 2D and 3D. However, ABQ was not fit for simulations that involved low material tensile strength, perfect brittle behaviour or a high degree of yielding. In these cases, the iteration process did not converge (even with a high number of maximal iterations). In order to stabilize the ABQ models, elasto-perfect-plastic material behaviour with a high dilation angle ($\psi = \phi \cdot 60\%$) had to be assigned to the rock. Other attempts of dealing with the convergence problems were adding strain hardening before failure (in brittle models), testing alternative boundary conditions (for 3D models) and increasing the mesh density around the flaw. These attempts did not successfully enhance the numerical stability of the elastoplastic problems. The numerical stability however appeared to depend on the mesh density of the models. This is discussed in the next paragraph.

ABQ uses the Newton-Raphson method to solve non-linear numerical problems, such as loading of elasto-plastic media. This may help explain why some models converged in RS2 and not ABQ (as RS2 implements other versions of Newton's method). Another possible explanation for the convergence problems in ABQ might be related to the mesh. During the simulations, it was observed that the models became more unstable as the mesh density around the flaw increased. A model that converged when a coarse mesh was applied did not always converge when a fine mesh was applied. Moreover, the implemented stopping criteria in ABQ were used, but this had no noteworthy effect on the model stability — even if the tolerance limits were increased. This points to the fact that the convergence problems are related to the Newton-Raphson method, and possibly how the Newton-Raphson method deals with fine meshes or meshes where there is high contrast between the element sizes (for example smaller elements close to the flaw and larger elements far-field). No relevant research on mesh-refinement tests using the Newton-Raphson method was found in literature search. This could therefore be investigated further by performing systematic mesh-refinement tests in ABQ, where both meshes with equally sized elements and meshes with high contrast in element size are compared.

7.2.4 Program recommendations for further work

In this project, the programs RS2 and ABQ complimented each others to a certain degree. RS2 produced numerically stable results for two-dimensional numerical analyses with desired material properties. Further, ABQ simulated 2D and 3D models using adjusted material properties.

A shortcoming with working with both RS2 and ABQ programs in one project, is that they use different stress conventions. In ABQ, positive stress values are defined as tensile stress. In RS2, positive stress values are conversely defined as compression stress (and vice versa). This resulted in extra work when writing this report. To avoid confusion for the reader (and the author), the sign of the all the stress values from ABQ were changed, and the legends from ABQ were therefore edited in a photo editing software. Additionally, comparing the yielded elements results from ABQ and RS2 were challenging for the simulations where first order elements were used. ABQ marks the elements as either actively yielding (1) or not yielding (0). The RS2 yielded elements contour plot returns the percentage of yielded elements connected to a node. Further, RS2 takes the nodal yield percentages and returns continuous yield contour lines within the elements. It was therefore slightly difficult to compare these contour plots. However, when 3D elements are used, ABQ gives a continuous AC yield plot.

To sum up, RS2 was a good tool for two-dimensional simulation of uniaxial compression tests. Other supplementing tools (for production of importable lists of geometry coordinates) were however necessary for convenient model design. As discussed in the above sections, 2D and 3D modelling where special joint elements (cohesive elements/interface elements) are assigned to the rock/grout boundary is recommended in future work. This can be done relatively conveniently in RS2 by converting the flaw material boundary to a joint boundary and experimenting with the joint strength parameters. In ABQ, this is more complicated: a rock part with an excavated flaw (with continuum elements), a thin boundary part (with cohesive elements) and a flaw filling material part (with continuum elements) need to be designed and then joined together in the ABQ assembly module. Additionally, the ABQ models might not converge with desired material properties. Therefore, this project recommends using RS2 instead of ABQ for further 2D joint element analyses. For further 3D analyses (with or without joint/interface/cohesive elements), a program that uses the accelerated stiffness method might be a better option than ABQ.

8 Conclusions and Suggestions for Future Research

This chapter rounds off the current thesis with conclusions and suggestions for further research.

8.1 Conclusions

This thesis set out to examine the strengthening effects from grouting of rock specimens, and how grouting affects the stress distribution in the specimen. For this purpose, numerical uniaxial compression tests of rocks containing a single grouted or non-grouted flaw of varying length and dip angle were simulated. The basis for the numerical model design was the methodology behind experimental uniaxial compression tests of grouted rocks performed by Le et al. (2018). Another aim of the current study was to verify the numerical results by comparing the numerical failure modes to the experimental crack types that occurred in the tests by Le et al. (2018). The numerical simulations were carried out with the FEM codes RS2 and Abaqus/Standard in two and three dimensions. The following conclusions and significant findings can be drawn from this thesis:

1. Grouting of flaws resulted in significant reduction of yielding in the numerical rock models. This suggests that grouting improves the strength of rocks with open flaws. (Consistent with findings from Le et al. (2018).)
2. The strengthening effect from grouting is more pronounced for rock specimens containing longer flaws rather than shorter flaws. Moreover, the strength reinforcement is most efficient when the flaws are orientated at high angles (75-90°) from the applied uniaxial load. (Consistent with findings from Le et al. (2018).)
3. The computed σ_1 and σ_3 contour plots showed an efficient reduction of stress concentrations around the tips and middle-sections of the flaw when the flaws were grouted, compared to the cases where the flaws were not grouted. This finding supports the idea of Le et al. (2018), who suggested that one of the important mechanisms behind grout reinforcement is stress reduction around the flaw tips.
4. The numerical yielded elements contour plots and experimental failure modes showed similarities in crack initiation points and propagation path. Specifically, the numerical simulations produced tensile yielding patterns at the flaw tip that resembled the tensile cracks I, II and III from Le et al. (2018) and the wing crack described by Ashby and Sammis (1990).
5. For specimens containing a grouted flaw, lab tests indicated more tensile cracks originating from the midflaw area than the numerical 2D models. Moreover, the grouted numerical 3D models produced more tensile stress at the midflaw area than the numerical 2D models.
6. For specimens containing an ungrouted flaw of low dip angles (0,15 and 30°), the numerical 2D models produced tensile cracks that initiated from the midflaw area. However, Le et al. (2018) claimed that no midflaw crack occurred in their ungrouted specimens. Conversely, their photograph of a specimen containing a 20 mm long horizontal ungrouted flaw actually showed a crack growing from the midflaw. Moreover, the numerical stress contour plots produced high tensile stress concentrations at the midflaw in ungrouted models. These findings point to the midflaw as possible area for tensile crack initiation in specimens containing ungrouted flaws rotated 0 – 70° from the loading axis.
7. Shear crack type IX from Le et al. (2018) did not occur in the numerical models. This is because the flaw material boundary was modelled with infinite shear strength.
8. The 3D simulations of a grouted flaw produced unexpected non-zero stress buildups in the direction normal to both the compression axis and the plane containing the flaw. This effect is likely due to the fact that the flaw boundary was modelled with continuum elements. Moreover, this observation suggests that future numerical modelling of grouted flaws assigns interface elements to the rock/grout boundary.

-
9. A 2D simulation where the Poisson's ratio (ν) of the epoxy/grout was decreased from 0.45 to 0.20, and a 3D simulation where ν of epoxy/grout was decreased from 0.45 to 0.18 were carried out for models containing grouted flaws with dip angles of 30° (where the rock was modelled with $\nu = 0.18$). Due to the reduction of ν , less yielding and lower stress concentrations occurred around the flaw. This finding suggests using a grout with a Poisson's ratio close to the Poisson's ratio of the rock in practical grouting.

Based on remarks 1-4, it can be said that the agreement between the numerical results from the current study, the experimental results by Le et al. (2018) and other literature (*e.g.* Ashby and Sammis (1990)) is good. However, due to the inconsistencies described in point 5-7, along with the recommendation in point 8, this thesis suggests that further three-dimensional numerical analyses — where the rock-grout material boundary is modelled with interface elements — are carried out. Such analyses might establish a better understanding of the stress field close to the midflaw area of grouted flaws.

8.2 Suggestions for further research

This section summarizes and elaborates some of the most significant suggestions for further research that were proposed in Chapter 6 and Chapter 7. Once numerical models are validated against experimental results, modelling of large-scale problems can be attempted. Large-scale problems can involve *e.g.* deformation and failure around a tunnel constructed in a grouted rock mass. This study began the process of validation of small-scale problems. However, due to some inconsistencies between numerical and experimental models, the following suggestions can be applied before attempting large-scale modelling.

Further studies of grout/epoxy interface shear strength

As mentioned in the introduction, literature (*e.g.* Liu et al. (2017), Wang et al. (2019), Le et al. (2018)) suggests that grouting can increase the shear strength (cohesion and internal friction angle) of the grout/rock interface flaws. Moreover, Le et al. (2018) outlined this effect as one of the mechanisms behind grout reinforcement of rocks. Another suggested grout reinforcement mechanism was stress reduction around the flaw. The numerical models that were analysed in this study used continuum elements to model the epoxy (grout) and rock boundary, and therefore assigned infinite shear strength to this boundary. This is of course an overestimation of the practical shear strength of grout/rock interfaces. Future numerical analyses should include parameter studies of the shear strength (c and ϕ) of the material boundary, by using interface elements. It would be interesting to compare the stress concentrations and yielding around the flaw for cases with varying c and ϕ parameters on the material boundaries. Such analyses could be carried out with 2D models, but should be supplemented or verified with 3D models.

As mentioned in Chapter 7, using infinite shear strength along the material boundary might additionally cause errors in the model (manifested as unexpected non-zero stress buildups around the flaw boundary in the unloaded and non-restrained z-direction). This is another reason why this thesis suggested interface elements in future 3D modelling of grouted rock specimens.

This study experienced convergence problems when using the Newton-Raphson method (which is implemented in Abaqus/Standard) for computation of the non-linear rock models containing flaws. Conversely, no convergence issues occurred with the accelerated initial stiffness method (which is implemented in RS2). Therefore, this thesis recommends using codes that uses the accelerated initial stiffness iteration method for future modelling.

Further studies of grout material properties

In some 2D and 3D simulations, the ν (Poisson's ratio) of the epoxy was reduced to match the ν of the rock. The results indicated that when the contrast between ν of the rock and grout/epoxy was reduced, the stress concentrations and yielding in the rock surrounding the flaw were reduced. A further study could investigate the stress magnitudes and yielded elements around flaws filled with grouts of varying

values of ν and E (Young's modulus). The suggested study should test several flaw dip angles. This could have implications for the choice of grout material quality in practical rock mass grouting.

Investigation of rough-walled fractures or partially grouted flaws

In this study, grout material was assigned to the entire void of the open flaw. It can therefore be said that a perfect grouting outcome was assumed. Voids, fractures and discontinuities that occur naturally in rock masses have rough, uneven surface conditions. Depending on local stress conditions, fractures can be closed or open at local points. Moreover, fractures can be filled with crushed/weathered rock material. Therefore, the grouting outcome cannot be assumed to be perfect at all points of the fractures in real grouting projects.

Further studies that explore rocks or rock masses with uneven or rough-walled fractures that are grouted unevenly would be interesting. However, such models involve sharp geometries and small voids — which can produce stress singularities — and might be challenging to model with FEM.

Bibliography

- Ashby, M. and Sammis, C. (1990), ‘The damage mechanics of brittle solids in compression’, *Pure and applied geophysics* **133**(3), 489–521.
- Barton, N., Bandis, S. and Bakhtar, K. (1985), Strength, deformation and conductivity coupling of rock joints, in ‘International journal of rock mechanics and mining sciences & geomechanics abstracts’, Vol. 22, Elsevier, pp. 121–140.
- Barton, N. and de Quadros, E. F. (1997), ‘Joint aperture and roughness in the prediction of flow and groutability of rock masses’, *International Journal of Rock Mechanics and Mining Sciences* **34**(3-4), 252–e1.
- Bohlooli, B., Skjølsvold, O., Justnes, H., Olsson, R., Grøv, E. and Aarset, A. (2019), ‘Cements for tunnel grouting—rheology and flow properties tested at different temperatures’, *Tunnelling and Underground Space Technology* **91**, 103011.
- Brown, S. R. (1987), ‘Fluid flow through rock joints: the effect of surface roughness’, *Journal of Geophysical Research: Solid Earth* **92**(B2), 1337–1347.
- Dang, H. K., Yacoub, T., Curran, J., Visser, M. and Wai, D. (2014), ‘Evaluate the performance of an accelerated initial stiffness method in three dimensional finite element analysis’, *Computers and Geotechnics* **62**, 293–303.
- Dassault Systèmes (2014), ‘Getting started with Abaqus: Interactive Edition’. Version 6.14.
- Dassault Systèmes (2017), ‘Abaqus/CAE 2017’, <https://www.3ds.com/products-services/simulia/products/abaqus/abaquscae/>.
- Eberhardt, E., Stead, D. and Stimpson, B. (1999), ‘Quantifying progressive pre-peak brittle fracture damage in rock during uniaxial compression’, *International Journal of Rock Mechanics and Mining Sciences* **36**(3), 361–380.
- Griffiths, D. and Lane, P. (1999), ‘Slope stability analysis by finite elements’, *Geotechnique* **49**(3), 387–403.
- Hoek, E. and Martin, C. (2014), ‘Fracture initiation and propagation in intact rock—a review’, *Journal of Rock Mechanics and Geotechnical Engineering* **6**(4), 287–300.
- Kranz, R. L. (1979), Crack-crack and crack-pore interactions in stressed granite, in ‘International Journal of Rock Mechanics and Mining Sciences & Geomechanics Abstracts’, Vol. 16, Elsevier, pp. 37–47.
- Kurowski, P. M. (2004), ‘Finite element analysis for design engineers’.
- Labuz, J. F. and Zang, A. (2012), Mohr–coulomb failure criterion, in ‘The ISRM Suggested Methods for Rock Characterization, Testing and Monitoring: 2007-2014’, Springer, pp. 227–231.
- Le, H., Sun, S., Kulatilake, P. H. and Wei, J. (2018), ‘Effect of grout on mechanical properties and cracking behavior of rock-like specimens containing a single flaw under uniaxial compression’, *International Journal of Geomechanics* **18**(10), 04018129.
- Liu, Q., Lei, G., Peng, X., Lu, C. and Wei, L. (2017), ‘Rheological characteristics of cement grout and its effect on mechanical properties of a rock fracture’, *Rock Mechanics and Rock Engineering* **51**(2), 613–625.
- Mo, S. and Skjetne, P. (2016), ‘Numerical simulations of grout flow in simplified geometries’, *8th Nordic Grouting Symposium, Oslo, Norway, 26.-27. September. 2016* .
- Ottosen, N. S. and Petersson, H. (1992), *Introduction to the Finite Element Method*, Pearson Education.
- Rocscience Inc. (2021a), ‘Axisymmetric Analysis’. (accessed: 12.04.2021).
URL: https://www.rocscience.com/help/rs2/tutorials/rs2_axisymmetric_analysis.htm
- Rocscience Inc. (2021b), ‘RS2 - 2D Geotechnical Finite Element Analysis’, www.rocscience.com. Version 11.

Rocscience Inc. (2021c), ‘Stress Analysis Settings in RS2’. (accessed: 12.04.2021).

URL: https://www.rocscience.com/help/rs2/phase2_model/stress_analysis.htm

Saeidi, O., Stille, H. and Torabi, S. R. (2013), ‘Numerical and analytical analyses of the effects of different joint and grout properties on the rock mass groutability’, *Tunnelling and underground space technology* **38**, 11–25.

Sun, C. and Jin, Z.-H. (2012a), Chapter 1 - introduction, in C. Sun and Z.-H. Jin, eds, ‘Fracture Mechanics’, Academic Press, Boston, pp. 1–10.

URL: <https://www.sciencedirect.com/science/article/pii/B9780123850010000018>

Sun, C. and Jin, Z.-H. (2012b), Chapter 2 - griffith theory of fracture, in C. Sun and Z.-H. Jin, eds, ‘Fracture Mechanics’, Academic Press, Boston, pp. 11–24.

URL: <https://www.sciencedirect.com/science/article/pii/B978012385001000002X>

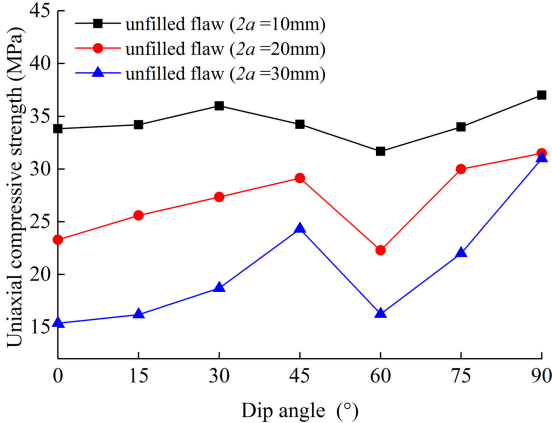
Wang, C., Li, X., Xiong, Z., Wang, C., Su, C. and Zhang, Y. (2019), ‘Experimental study on the effect of grouting reinforcement on the shear strength of a fractured rock mass’, *PloS one* **14**(8), e0220643.

Zolfaghari, A., Bidar, A. S., Javan, M. M., Haftani, M. and Mehinrad, A. (2015), ‘Evaluation of rock mass improvement due to cement grouting by q-system at bakhtiary dam site’, *International Journal of Rock Mechanics and Mining Sciences* **74**, 38–44.

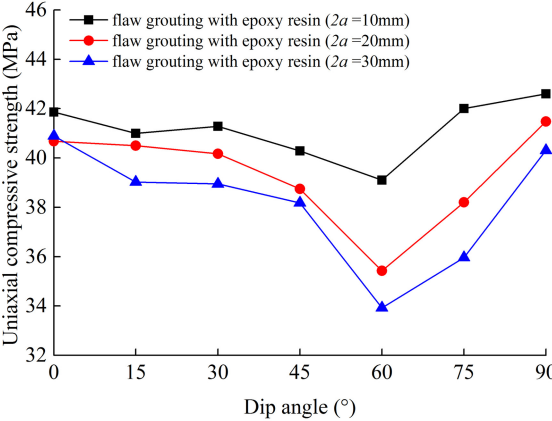
Appendix

- Appendix A** Observed crack types and UCS-values from uniaxial compression tests by Le et al. (2018)
- Appendix B** Maximal stress magnitudes and yielded element percentages from the experimental design task
- Appendix C** Yielded elements contour plots from the experimental design task (legend is given in Figure 28).

A Crack Types and UCS-Values from Uniaxial Compression Tests by Le et al. (2018)



(a)



(b)

Figure A1: UCS for specimens containing ungrouted flaws (a) and grouted flaws(b), from Le et al. (2018). Results for different length and inclination angle are plotted.

Table A1: Overview of the crack types that occurred in the specimens containing ungrouted flaws of different combinations of length ($2a$) and inclination angle (α). (Snippet from Le et al. (2018).)

Series	α (°)	Crack types						
		Type I tensile	Type II tensile	Type III antitensile	Type IV shear	Type V far field	Type VI surface spalling	Type VII corner spalling
Unfilled flaw ($2a = 10$ mm)	0		X					
	15		X	X			X	
	30		X				X	
	45			X			X	
	60		X		X		X	
	75		X					
	90	X					X	X
Unfilled flaw ($2a = 20$ mm)	0		X				X	
	15		X	X			X	
	30	X	X			X		
	45			X		X	X	
	60	X		X	X		X	
	75			X			X	
	90	X				X		X
Unfilled flaw ($2a = 30$ mm)	0		X				X	
	15		X				X	
	30		X					
	45			X	X		X	
	60		X		X		X	
	75		X		X	X	X	
	90		X			X		X

Table A2: Overview of the crack types that occurred in the specimens containing grouted flaws of different combinations of length ($2a$) and inclination angle (α). "N/A" indicates that the cracking occurred in the lateral sides of the specimens (not in the sides containing the grouted flaws). (Snippet from Le et al. (2018).)

Series	α (°)	Crack types								
		Type I tensile	Type II tensile	Type III antitensile	Type IV shear	Type V Far field	Type VI surface spalling	Type VII corner spalling	Type VIII tensile	Type IX shear
Grout-infilled flaw ($2a = 10$ mm)	0					X				
	15	N/A								
	30					X		X		
	45					X	X			
	60		X				X			X
	75					X				X
90	N/A									
Grout-infilled flaw ($2a = 20$ mm)	0	X				X	X	X	X	
	15		X				X		X	
	30					X	X	X	X	
	45		X			X	X			
	60	X	X				X			X
	75		X				X			X
90					X	X	X	X		
Grout-infilled flaw ($2a = 30$ mm)	0					X		X		
	15		X			X	X	X	X	
	30					X	X	X	X	
	45					X	X		X	
	60		X							X
	75	X					X			X
90	N/A									

B Numerical Results

Results Experimental Design linear-elastic models

Table B1: The maximum σ_1 and minimum σ_3 values and their location, from the linear-elastic models containing ungrouted flaws (experimental design).

Simulation	$\alpha(^{\circ})$	$\sigma_{1,max}$ (MPa)	Location	$\sigma_{3,min}$ (MPa)	Location
Ungouted flaw 2a=10 mm	0	138,54	Flawtip (FT)	-17,09	Midflaw (MF)
	15	130,15	FT	-21,21	Close to FT/MF
	30	110,66	FT	-26,72	FT
	45	110,6	FT	-32,56	FT
	60	122,85	FT	-25,54	FT
	75	75,23	FT	-16,83	FT
	90	29,07	MF	-8,82	FT
Ungouted flaw 2a = 20 mm	0	160,74	FT	-18,25	MF
	15	167,45	FT	-23,27	MF
	30	159,87	FT	-31,05	Close to FT/MF
	45	191,56	FT	-65,13	FT
	60	167,21	FT	-40,25	FT
	75	83,15	FT	-34,74	FT
	90	28,22	FT	-7,9	FT
Ungouted flaw 2a = 30 mm	0	177,54	FT	-18,28	MF
	15	242,52	FT	-24,59	MF
	30	228,84	FT	-33,07	MF
	45	180,52	FT	-46,78	FT
	60	148,68	FT	-59,5	FT
	75	127,03	FT	-38,18	FT
	90	28,75	FT	-7,07	FT

Table B2: The maximum σ_1 and minimum σ_3 values and their location, from the linear-elastic models containing grouted flaws (experimental design).

Simulation	$\alpha(^{\circ})$	$\sigma_{1,max}$ (MPa)	Location	$\sigma_{3,min}$ (MPa)	Location
Grouted flaw 2a=10 mm	0	46,79	FT	-5,82	close to FT
	15	56,02	FT	-18,57	FT
	30	58,57	FT	-39,21	FT
	45	66,32	FT	-35,03	FT
	60	78,1	FT	-26,32	FT
	75	53,93	FT	-17,84	FT
	90	26,33	MF	-9,17	FT
Grouted flaw 2a = 20 mm	0	41,68	FT	-5,46	close to FT
	15	57,23	FT	-23	FT
	30	68,62	FT	-49,38	FT
	45	95,93	FT	-61,42	FT
	60	86,37	FT	-34,36	FT
	75	54,07	FT	-24,87	FT
	90	26,49	FT	-7,63	FT
Grouted flaw 2a = 30 mm	0	41,37	FT	-5,2	close to FT
	15	70,5	FT	-28,52	FT
	30	83,94	FT	-43,11	FT
	45	79,29	FT	-47,88	FT
	60	71,13	FT	-46,38	FT
	75	64,61	FT	-25,8	FT
	90	27,04	FT	-6,12	FT

Results Experimental Design elastoplastic models

The following tables, Table B3, Table B4 and Table B5 use the following terminology:

\mathcal{E}_{total}	—	The total number of elements assigned to the structure (model)
\mathcal{E}_{rock}	—	The total number of elements assigned to the rock material section
\mathcal{E}_{flaw}	—	The total number of elements assigned to the grout material section
$\mathcal{E}_{rock,Y}$	—	The total number of yielded elements in the rock material section
$\mathcal{E}_{flaw,Y}$	—	The total number of yielded elements in the grout material section

Table B3: The number of yielded elements in the rock material section, and the percentage of the elements in the rock section that yielded in the elastoplastic **ungROUTED** series of the experimental design. The table also comments the observed crack types, as described in table 3.

Simulation	$\alpha(^{\circ})$	\mathcal{E}_{total}	\mathcal{E}_{rock}	$\mathcal{E}_{rock,Y}$	$\mathcal{E}_{rock,Y}/\mathcal{E}_{rock}$ (%)	Crack type
UngROUTED flaw 2a = 10 mm	0	1574	1574	675	42,9	II, IV, midflaw tensile
	15	1422	1422	282	19,8	II, IV
	30	1501	1501	321	21,4	II, IV
	45	1710	1710	459	26,8	II, III, IV
	60	1498	1498	114	7,61	I, II, IV
	75	1422	1422	92	6,47	II, shear at tip
	90	1574	1574	25	1,59	II, shear at tip
UngROUTED flaw 2a = 20 mm	0	1806	1806	1007	55,8	II, IV, midflaw tensile
	15	1826	1826	858	47,0	I, II, III, IV
	30	1686	1686	471	27,9	I, II, IV
	45	1894	1894	471	24,9	I, II, III, IV
	60	1686	1686	266	15,8	I, II, IV
	75	1804	1804	136	7,54	II, shear at tip
	90	1806	1806	13	0,72	tensile at tip
UngROUTED flaw 2a = 30 mm	0	1874	1874	1022	54,5	II, IV, midflaw tensile
	15	1970	1970	996	50,6	II, III, IV, midflaw tensile
	30	1955	1955	798	40,8	I, II, III, IV, midflaw tensile
	45	2162	2162	538	24,9	I, II, IV
	60	1950	1950	635	32,6	I, II, III,IV, midflaw tensile
	75	1975	1975	256	13,0	II, shear at tip
	90	1874	1874	15	0,80	tensile at tip

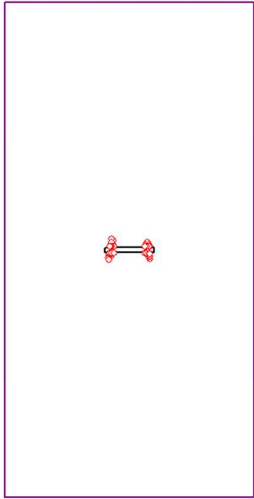
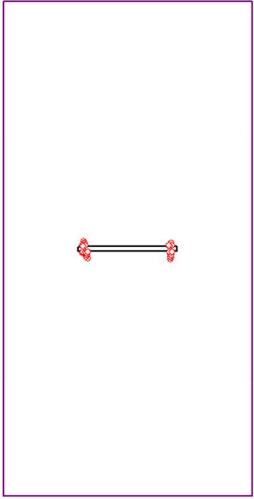
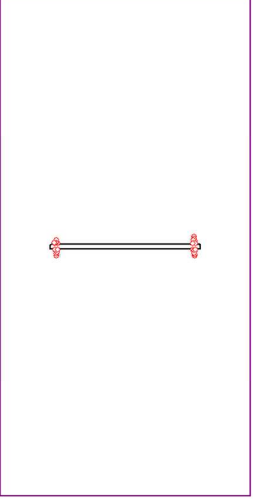
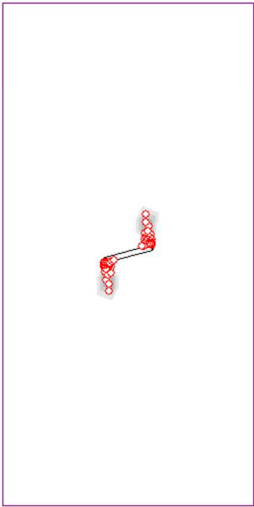
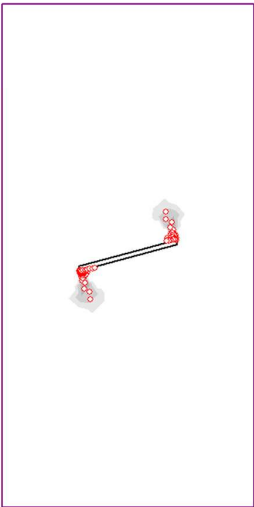
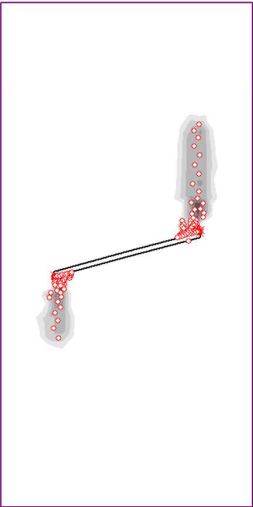

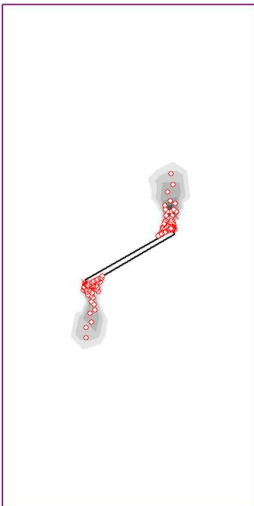
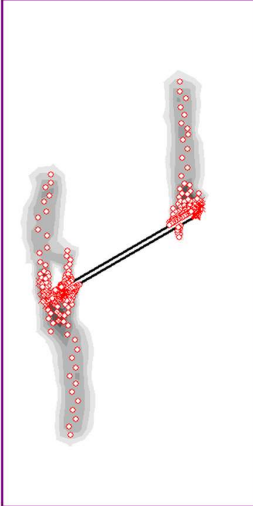
Table B4: The number of yielded elements in the rock material section and epoxy material section and the percentage of the elements in the rock section that were yielded in the elastoplastic **grouted** series of the experimental design. The table also comments the observed crack types, as described in Table 3.

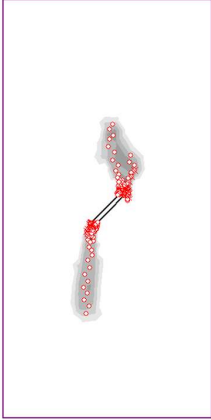
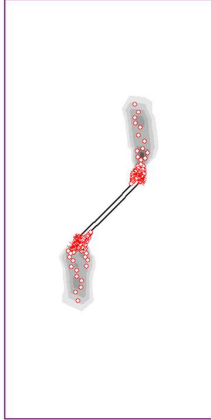
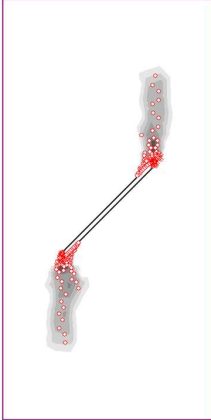
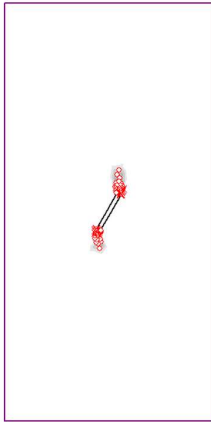
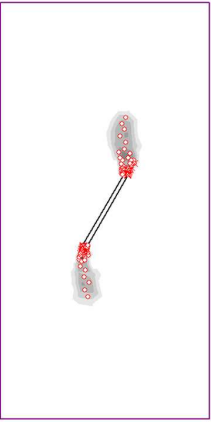
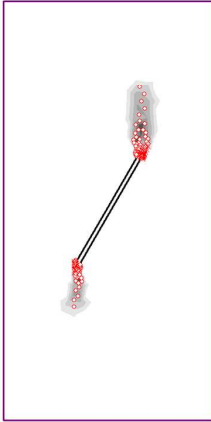
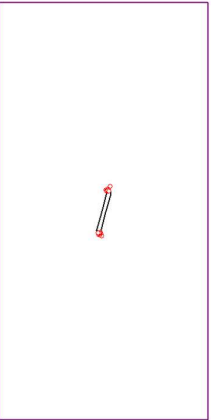
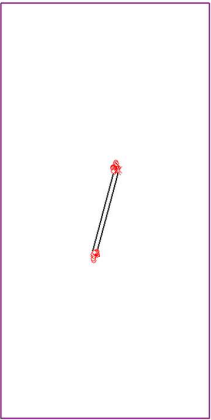

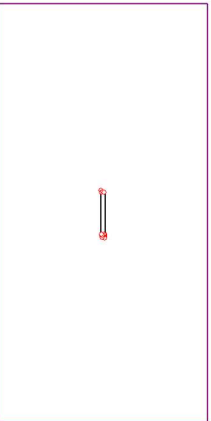
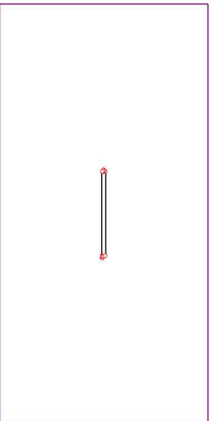
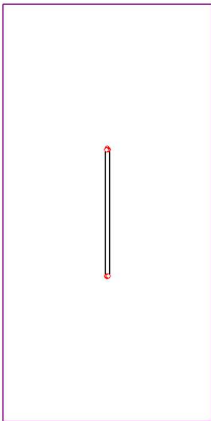
Simulation	$\alpha(^{\circ})$	\mathcal{E}_{total}	\mathcal{E}_{rock}	\mathcal{E}_{flaw}	$\mathcal{E}_{rock,Y}$	$\mathcal{E}_{flaw,Y}$	$\mathcal{E}_{rock,Y}/\mathcal{E}_{rock}$ (%)	Crack type
Grouted flaw 2a = 10 mm	0	1804	1574	230	41	0	2,60	II
	15	1552	1422	130	60	0	4,22	II
	30	1638	1501	137	93	0	6,20	II, shear at tip
	45	1832	1710	122	227	0	13,3	I, II, shear at tip
	60	1628	1498	130	85	0	5,67	II, shear at tip
	75	1552	1422	130	23	0	1,62	II
	90	1702	1574	128	19	0	1,21	II
Grouted flaw 2a = 20 mm	0	1994	1806	188	32	0	1,77	II
	15	2046	1826	220	91	0	4,98	II
	30	1880	1686	194	151	0	8,96	II, shear at tip
	45	2036	1894	142	200	0	10,6	II, shear at tip
	60	1888	1686	202	112	0	6,64	II, shear at tip
	75	2016	1804	212	52	0	2,88	II, shear at tip
	90	1994	1806	188	13	0	0,72	II
Grouted flaw 2a = 30 mm	0	2152	1874	278	27	0	1,44	II close to tip
	15	2260	1970	290	162	0	8,22	II, shear at tip
	30	2244	1955	289	337	0	17,2	I, II, III, shear at tip
	45	2368	2162	206	249	0	11,5	I, II, shear at tip
	60	2236	1950	286	163	0	8,36	II, shear at tip
	75	2270	1975	295	96	0	4,86	II, shear at tip
	90	2150	1874	276	11	0	0,59	tensile at tip

Table B5: The number of yielded elements in the rock material section and epoxy material section, and the percentage of the elements in the rock and epoxy sections that yielded in the elastoplastic **grouted** model, grouted with epoxy B (Plastic).

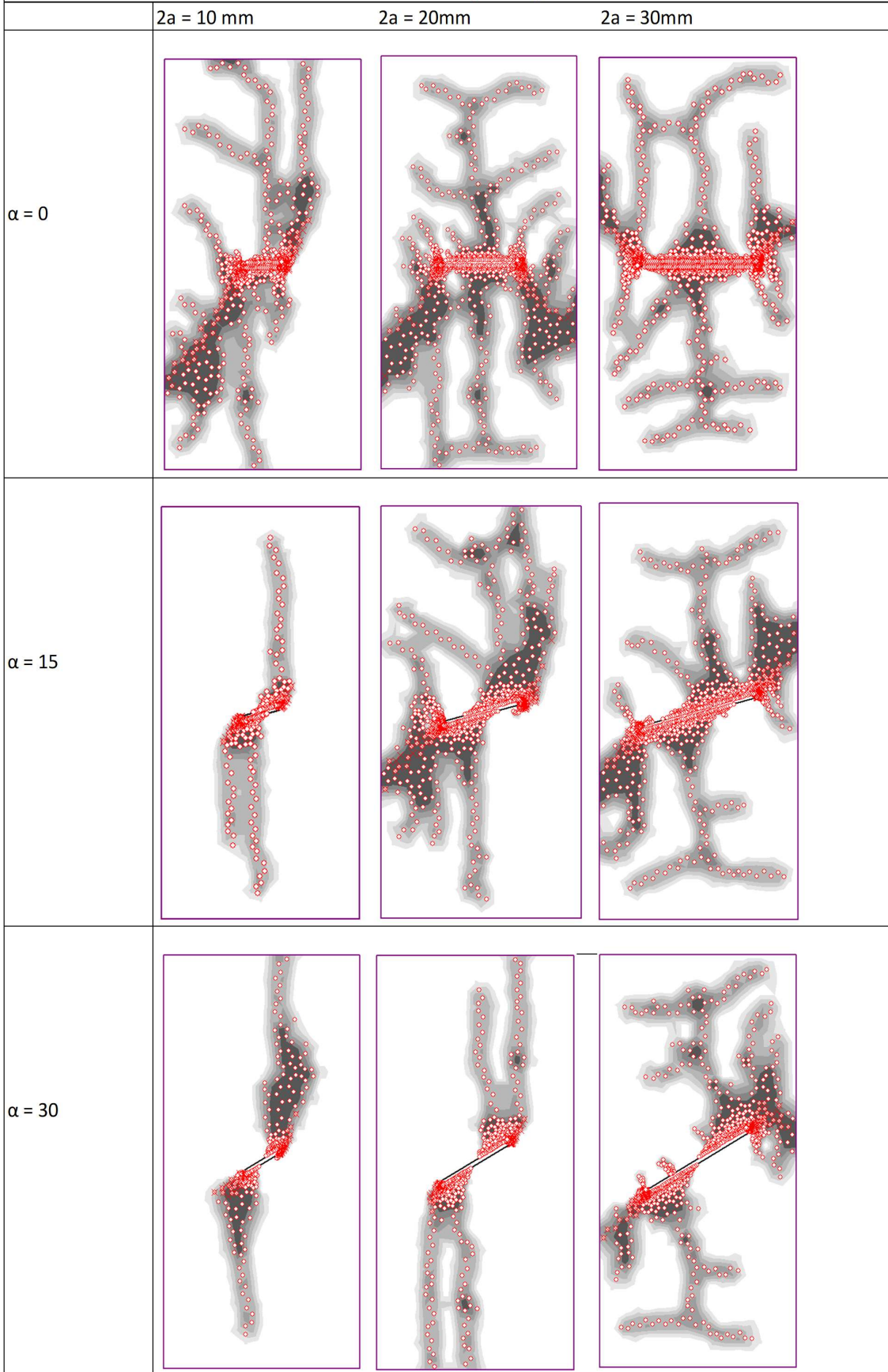
Simulation	2a (mm)	$\alpha(^{\circ})$	\mathcal{E}_{total}	\mathcal{E}_{rock}	\mathcal{E}_{flaw}	$\mathcal{E}_{rock,Y}$	$\mathcal{E}_{flaw,Y}$	$\mathcal{E}_{rock,Y}/\mathcal{E}_{rock}$ (%)
Grouted flaw	30	30	2244	1955	289	137	0	7

C Yielded Elements Contour Plots (Experimental Design)

Yielded elements in models containing a grouted flaw loaded with 20 MPa			
	2a = 10 mm	2a = 20 mm	2a = 30 mm
$\alpha = 0$			
$\alpha = 15$			
$\alpha = 30$			

Yielded elements in models containing a grouted flaw loaded with 20 MPa			
	2a = 10 mm	2a = 20 mm	20a = 30 mm
$\alpha = 45$			
$\alpha = 60$			
$\alpha = 75$			
$\alpha = 90$			

Yielded elements in models containing an ungrouted flaw loaded with 20 MPa



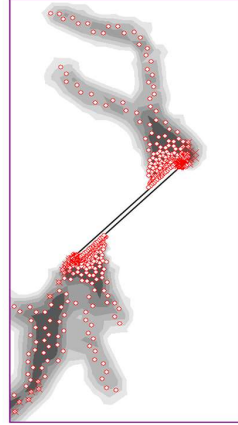
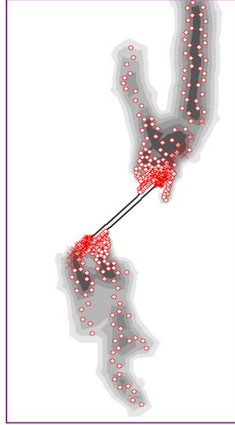
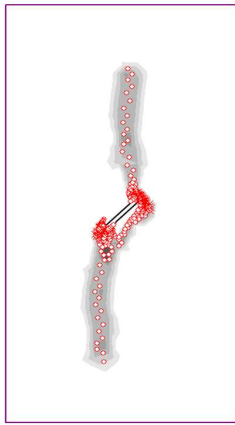
Yielded elements in models containing an ungrouted flaw loaded with 20 MPa

2a = 10 mm

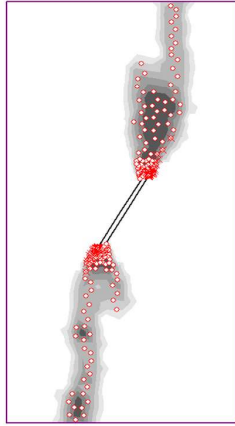
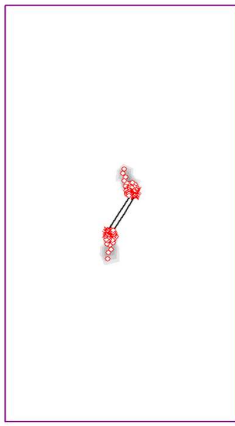
2a = 20 mm

20a = 30 mm

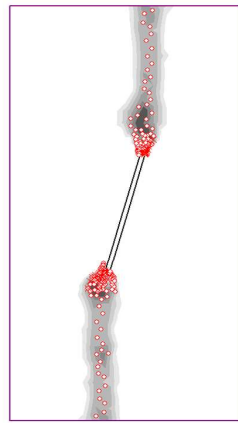
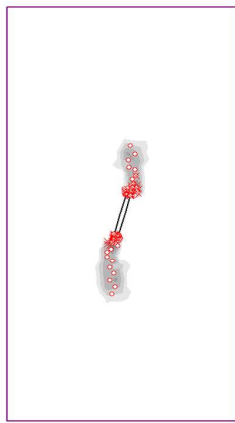
$\alpha = 45$



$\alpha = 60$



$\alpha = 75$



$\alpha = 90$

